AN ABSTRACT OF THE THESIS OF

George A. Pubanz for the degree of Doctor of Philosophy in Chemistry presented on July 22, 1986

Title: Nonlinear Raman Spectroscopy in Supersonic Jets

Abstract approved: Professor Joseph W. Nibler

The techniques of coherent anti-Stokes Raman spectroscopy (CARS) and inverse Raman spectroscopy (IRS) are used to examine carbon dioxide aggregation in a supersonic jet expansion. To promote the formation of small clusters, a BMW injector valve is modified to permit its use as a pulsed nozzle at very cold temperatures. This results in a substantial enhancement in the concentration of small aggregates and permits an analysis of relative spectral intensities as a function of initial temperature, pressure and composition. CARS probing of CO_2 in jets reveals several new peaks in the region of the Fermi doublet, ν_1 and $2\nu_2$, which appear only in the cold, highly condensing conditions of the expansion. This study focuses upon several peaks which are red shifted from the 1285.5 cm^{-1}, ν_1 monomer peak. The dependence of the relative peak intensities upon initial temperature and CO_2 concentration along with the relative shift from the monomer has enabled assignment of peaks at 1281.3 cm^{-1}, 1278.7 cm^{-1} and 1275.3 cm^{-1} to the dimer, trimer and higher polymers respectively.

The dimer structure has been the subject of much controversy and the present results are enlightening in this regard. The CARS dimer peak is shifted -4.1 cm^{-1} from the monomer resonance and comparison with a published infrared spectrum, showing a dimer band with a -0.7 cm^{-1} shift, shows that the dimer adheres to the rule of mutual exclusion and must therefore, have a structure with a center of symmetry. Earlier experimental and theoretical studies gave conflicting evidence for one of two structures, a T-shaped configuration with C_{2v} symmetry and an offset parallel structure with C_{2h} symmetry. Since only the C_{2h} form has a center of symmetry, it is concluded that the most stable arrangement for the dimer of CO_2 is the nonpolar, offset parallel structure.

The Fermi doublet of CO_2 is also used to characterize the performance of a new high resolution IRS spectrometer assembled as part of this thesis work. A pulse amplified, actively stabilized ring dye laser provides the Stokes beam for IRS studies while the probe beam is a chopped single-mode Ar ion laser. Almost completely resolved static and jet spectra of the ν_1 Q branch of CO_2 are reported and an instrumental resolution of 0.0033 cm^{-1} is determined.

Nonlinear Raman Spectroscopy in Supersonic Jets

by

George A. Pubanz

A THESIS

submitted to

Oregon State University

in partial fulfillment of
the requirements for the
degree of

Doctor of Philosophy

Completed July 22, 1986

Commencement June 1987

APPROVED:

Redacted for privacy

Professor of Chemistry in charge of major

Redacted for privacy

Head of department of Chemistry

Redacted for privacy

Dean of Graduate School

Date thesis is presented July 22, 1986

Typed by researcher for George A. Pubanz

ACKNOWLEDGEMENTS

I have completed this thesis and the research which led to it with the help of many people. I would like to acknowledge the contributions of these individuals.

Steve Bares, for his enthusiasm and thought provoking discussions.

Tom Lundeen, for his introduction to the laboratory and for numerous useful computer programs.

Brian Bozlee, for the many discussions of experiment and theory.

Glen Hopkins, for building the interfaces and writing the software for scanning the CARS apparatus and for the initial work on the BMW pulsed nozzle.

Mark Maroncelli, for providing ideas, programs, and the stimulation to keep on going when the CO_2 dimer problem looked hopeless.

Jeng Yang, for taking the data used for the pressure series depicted in Figure 4.8.

John Archibald and Bob Boyer, for providing the machine shop support essential for this research.

Jerry Allison and Doyle Woodrow, for their consultations and their ability to get equipment running after the inevitable catastrophy.

Professor Joseph Nibler, my mentor and friend, for innumerable good ideas, boundless enthusiasm, and seemingly infinite patience. Without Professor Nibler's moral and financial support as well as his ideas for the original research, none of this work would have been accomplished.

I credit my father, George A. Pubanz, Sr., with nurturing and encouraging my interest in science.

The one person to whom the greatest credit is due is my wife, Mary Ellen Collentine. She encouraged me at every turn and continued to have faith when my own was faltering. Without her support I would never have begun this odyssey.

TABLE OF CONTENTS

LIST OF FIGURES

FIGURES (cont.)

LIST OF TABLES

NONLINEAR RAMAN SPECTROSCOPY IN SUPERSONIC JETS

CHAPTER 1 -- INTRODUCTION

Nonlinear Raman spectroscopic techniques have been developed to study the weak intermolecular forces in dimers and small clusters of gas molecules. The present work details the study of carbon dioxide, its dimer and higher polymers formed in cooled supersonic jet expansions using the nonlinear Raman techniques of coherent anti-Stokes Raman scattering and high resolution inverse Raman spectroscopy.

This chapter provides an overview of coherent Raman techniques and supersonic jet expansions and forms a basis for the more detailed description of the studies documented in chapters 3 and 4. In chapter 2 consideration is given to the theory of nonlinear Raman spectroscopy with particular attention to the CARS and IRS phenomena. Chapter 3 presents a study of clusters of carbon dioxide formed in supersonic jets and probed with the CARS technique. The investigation centers upon the structure of the dimer. Chapter 4 concludes this thesis with the details of the design and construction of a high resolution inverse Raman spectrometer, the characterization of this instrument with a linewidth study of the ν_1 Q branch of CO_2 and observations in the jet of the monomer and dimer regions of CO_2.

HISTORICAL PERSPECTIVE

Raman scattering, discovered in 1928 by the Indian physicist Sir Chandrasekhara V. Raman, has become a primary tool of the molecular

spectroscopist.[1] A monochromatic source of light passing through a transparent sample is scattered slightly, even if the sample is dust free and very pure. Most of the scattered radiation is of the same frequency as the source, however, a small fraction exhibits a change in frequency. The difference in frequency between the incident and the scattered radiation has been found to equal the difference between energy levels of the molecules of the sample.

Although limited by the weakness of the effect and the low intensity of the available monochromatic sources, Raman scattering quickly became a popular spectroscopic technique. Scattering of the incident radiation with no change in frequency is termed Rayleigh scattering and is typically 10^{-3} less intense than the incident radiation. The intensity of a strong Raman line is about 10^{-3} less than the Rayleigh scattering.[2] The discovery of the laser in 1960 and the subsequent development of the continuous gas laser heightened interest and multiplied the applications of this spectroscopic tool. Continued development of the laser as a research tool has fostered noteworthy advances in all branches of spectroscopy and in particular in Raman spectroscopy.

Discovery of stimulated Raman scattering by Woodbury and Ng in 1962,[3] followed closely by the observation of four wave mixing (4WM) in coherent anti-Stokes Raman scattering (CARS) in 1963 by Terhune[4] and by Maker and Terhune[5] in 1965, marked the beginning of the field of nonlinear Raman spectroscopy. These techniques and their variants, initially constrained by the available lines of fixed wavelength lasers, have undergone rapid development since the availability of tunable dye laser sources.

NONLINEAR RAMAN SPECTROSCOPY

Figure 1.1 compares the energy level schematic for spontaneous Raman spectroscopy with that for the CARS technique and for the complementary stimulated Raman spectroscopic (SRS) techniques of Raman gain spectroscopy (RGS) and inverse Raman spectroscopy (IRS). Spontaneous Raman spectroscopy is a "two photon" technique which involves the coupling of an incident photon with a scattered photon in an inelastic collision with a molecule. If the resulting change in energy of the scattered photon results from an absorption of energy by the molecule it is termed a Stokes band. Scattering by a molecule which undergoes a transition from an excited state to a lower energy state results in a scattered photon higher in energy than the incident photon and yields the anti-Stokes band. The Raman spectrum thus appears as symmetric sets of lines equally displaced at higher and lower frequencies with respect to the central Rayleigh line.

In contrast, nonlinear Raman spectroscopy is a "four photon" process which couples two or three incident laser beams to produce the observed signal. CARS spectroscopy as depicted in Figure 1.1b involves the mixing of two degenerate photons from the pump beam or beams with a third photon from a Stokes beam to produce a fourth, anti-Stokes, photon at higher energy. In contrast to the spontaneous Raman process, the CARS process is an elastic scattering event in which there is no net change in the energy of the sample molecule. As will be discussed further in chapter 2, the CARS signal is not due to an isolated scattering event, rather the signal emerges as a coherent beam into a well defined solid angle, the result of an oscillating polarization

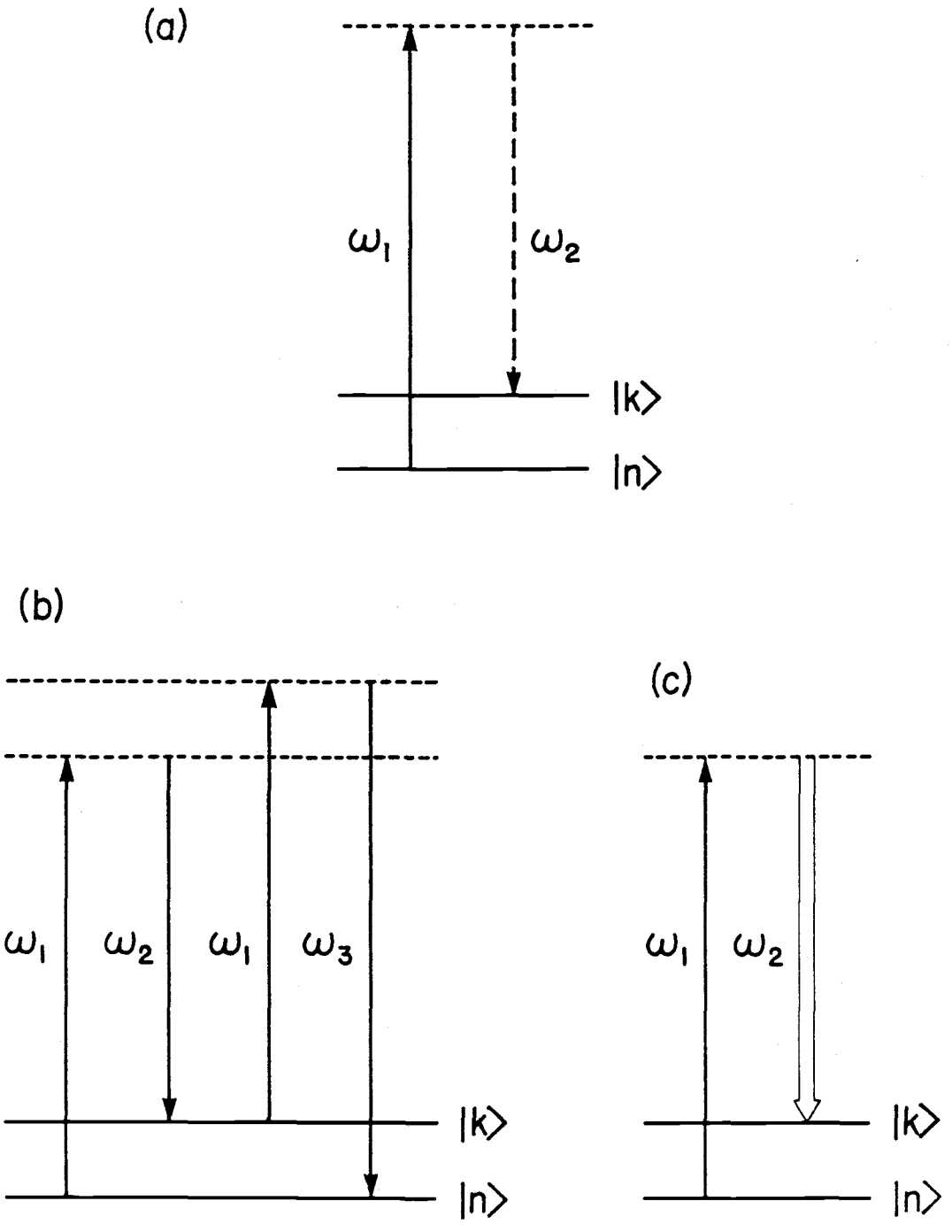

Figure 1.1 Energy level diagrams for linear and nonlinear Raman spectroscopy. (a) spontaneous Raman scattering, (b) CARS, and (c) IRS.

of the bulk sample. For the most common case where two of the input beams are degenerate, the beams have the frequency relationship $\omega_1 - \omega_2 = \omega_{kn}$ and $2\omega_1 - \omega_2 = \omega_3$. ω_1 is the pump beam, ω_2 the Stokes beam, ω_{kn} the frequency of a Raman active transition and ω_3 is the CARS beam.

The inverse Raman process depicted in Figure 1.1c is, like the spontaneous counterpart, an inelastic process which involves the absorption of energy by the sample. However, unlike spontaneous Raman, two laser beams simultaneously impinge upon the sample and a molecular resonance results in the decrease in intensity of the higher frequency beam and the corresponding increase in the intensity of the lower frequency beam. As before, the beams have the frequency relationship $\omega_1 - \omega_2 = \omega_{kn}$.

Several features make the nonlinear Raman methods attractive for the investigations in this work. The inherent advantages of using focussed beams coupled with the use of crossed beam geometry allows the sampling point to be determined very precisely. Depending upon the focal length of the lenses used and the angle of beam crossing, the volume of sample which contributes to the signal can be as small as a cylinder 10 μm in diameter and 100 μm long. With the optics used in these experiments the sample volume is somewhat larger but still small and precisely defined. The advantages of this spatial resolution become apparent when we consider probing the free expansion zone of a supersonic jet where nonequilibrium conditions make the population distribution a strong function of position.

Nonlinear Raman techniques offer substantial improvements in spectral resolution as well. Resolution is determined by the

linewidths of the source lasers which are inherently narrow and not by multipass monochromators. In addition, as will be discussed in detail in chapter 4, the use of actively stabilized lasers and pulse amplifiers permits very high resolution to be achieved.

Another important feature of nonlinear Raman spectroscopy is the laser-like properties of the signal beam. The CARS beam can only propagate in a direction which satisfies the phase matching conditions described in chapters 2 and 3. This effectively limits the solid angle to be similar to that of the input beams. As a consequence, all of the signal photons can be collected utilizing simple optics. When the input beams are colinear and the sample is nondispersive, various filters and polarization techniques must be used to discriminate against the input beams and allow the signal to be detected. On the other hand a three dimensional phase matching geometry described in chapter 3, produces a CARS beam spatially separate from the input beams; reducing the need for absorptive filters but also yielding less absolute signal due to a smaller interaction zone.

EXPERIMENTAL REQUIREMENTS

Nonlinear Raman spectroscopy derives its name from the fact that at high field intensities the induced polarization of the sample departs significantly from the linear response which characterizes the polarization at low fields. This nonlinear response will be described in more detail in chapter 2. For the present, it is sufficient to say that high fields are required to observe the nonlinear Raman effects.

The experimental apparatus required for both the CARS and IRS techniques is similar. Both experiments have been done using

continuous wave (cw) lasers but the modest field intensities which can be achieved limit the applications of the cw experiment to high density samples. Pulsed lasers have been used very successfully to generate very high fields and hence cause strong nonlinear response. In our experiments the laser pulse is created by using flashlamps to pump a rod shaped crystal of neodymium doped, yttrium aluminum garnet (Nd:YAG). An electrically activated polarization rotator (Q switch) allows the output of the "YAG" laser to be discharged in a very short pulse (10 - 20 ns) with a wavelength in the infrared band at 1.06 μm. For the spectroscopic studies discussed in this thesis the output is frequency doubled using second harmonic generation (SHG) in KD^*P to a wavelength of 532 nm. Though the average power output of a doubled YAG is typically between 100 mW and 2 W with a pulse repetition rate of 10 Hz, the "duty cycle" is very low and the power per pulse is enormous (10^6 W for a 10 ns pulse with 100 mW average power).

These pulsed beams are normally focussed to achieve the maximum nonlinear response. With focussing the magnitude of the electrical fields in the sample volume can easily surpass the ionization threshold and cause electrical breakdown of the sample. Breakdown thus poses a very real limitation to the amount of power which can be focussed within a sample. There are other, less dramatic effects such as saturation[6] and optical Stark splitting[7] which cause spectral distortion at high field intensities.

Part of the output of the YAG is used to pump a pulsed dye laser or pulsed dye amplifier to provide a tunable pulsed laser source. This tunable output is then combined with the fixed output of the YAG to provide the two frequencies for the CARS experiment. In the IRS

experiment one beam is provided by an actively stabilized ring dye laser which is pulse amplified by the YAG and the other beam is the chopped output of a cw argon ion laser.

SUPERSONIC JETS

The supersonic free jet expansion is the most recent of a series of techniques used to cool samples for spectroscopic purposes. Refrigeration of static samples has been used for many years to investigate hot band assignments and to probe for clusters. In addition, solid phase studies of both neat samples and dilute samples frozen into a host matrix have yielded important spectroscopic results. Gas phase studies are particularly desirable because the lines narrow to an extent that individual transitions can be observed. In molecules of more than a few atoms, gas phase spectra at room temperature often consist of a bewildering array of overlapping vibration-rotation bands. The simplification of spectra which can be achieved by cooling often aids in the process of assignment of these spectra.

The dynamics of the supersonic jet have been studied in great detail and there are many publications on the subject, illustrating the value of this technique to the scientific community. Our interest in the supersonic jet is in the very cold, condensing environment found in the early stages of the expansion. It is under these conditions that clusters of carbon dioxide can be formed in sufficient concentration to permit probing by the CARS technique (Chap 3). What follows here is a simple description of the properties of supersonic jets with an emphasis on those aspects related to the formation of clusters.

Physically, a supersonic jet forms when gas molecules at high pressure expand into a low pressure chamber through a small orifice. The size of the orifice or nozzle must be large enough to permit collisions to occur during the expansion thus enabling the redistribution of velocities which characterize a supersonic jet. Nozzle diameters are typically between 50 μm and 2 mm. The expansion chamber is connected to a vacuum system with a high pumping speed to maintain the low pressure condition. Figure 1.2 illustrates a jet apparatus and the temperature and density dependence on distance from the nozzle.

The cooling experienced by the sample during expansion is due to a redistribution of the thermal energy of the equilibrium sample prior to expansion into the energy of mass flow of the jet. Levy[8] has described the phenomenon related to conservation of enthalpy. If one assumes constant enthalpy per unit mass and h_0 is the enthalpy per unit mass in the reservoir, then

$$h_0 = h + u^2/2 \tag{1.1}$$

where u is the flow velocity and h is the enthalpy per unit mass at some point downstream of the nozzle. Eq. (1.1) gives a physically reasonable picture where the energy necessary to accelerate molecules into a molecular beam comes from the internal energy of the gas. Several parameters are necessary to conveniently express the condition of the sample at some point x downstream of the nozzle. Ratios of pressure, density and temperature are all related to the Mach number M,

$$M \equiv u/a \tag{1.2}$$

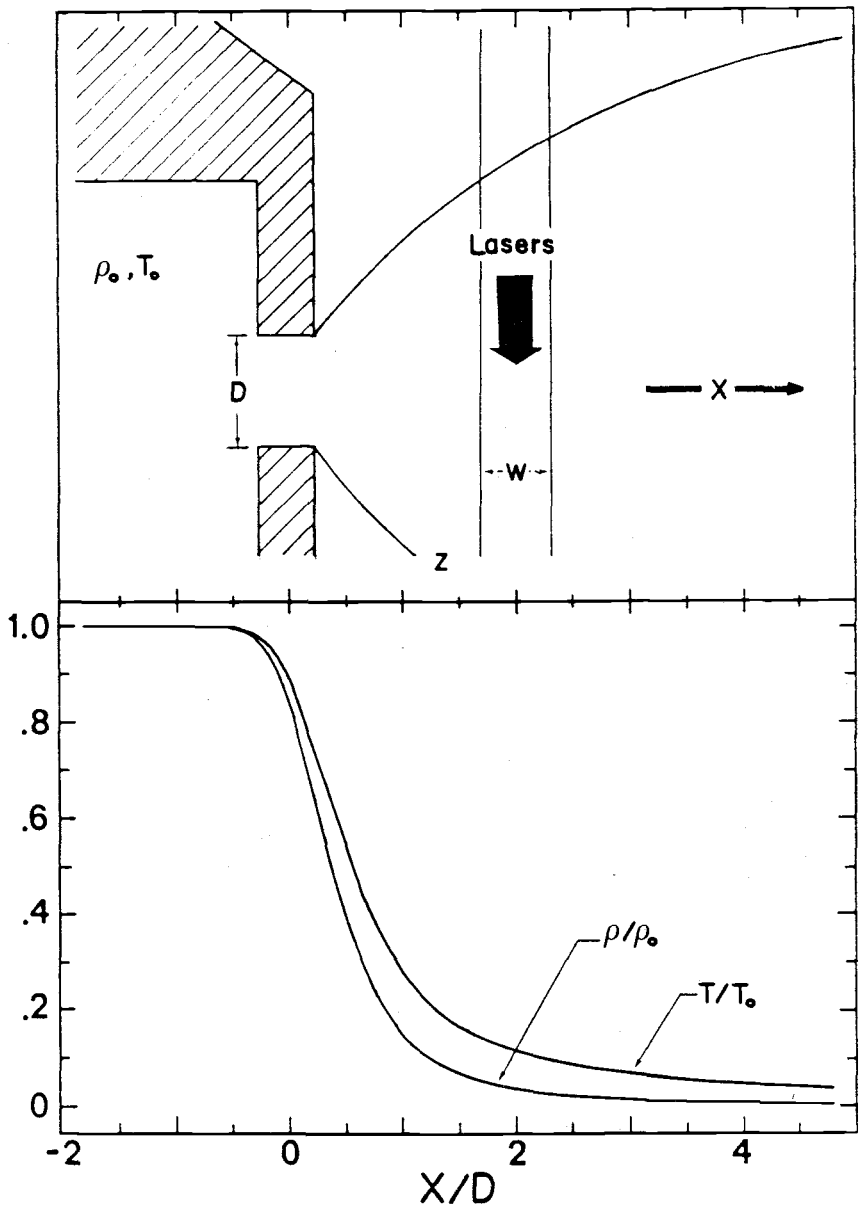

Figure 1.2 The supersonic jet expansion. The upper trace is a schematic of the supersonic expansion where ρ_0 and T_0 are the density and temperature respectively in the reservoir, D is the nozzle diameter, and X is the direction of bulk flow. Lasers are depicted as a cylinder rather than a focussed beam. The lower trace shows the change of density and temperature as one proceeds out from the nozzle.

where u is the flow velocity and a is the local speed of sound.

For an ideal gas

$$a = (\gamma r T)^{\frac{1}{2}} \tag{1.3}$$

where $\gamma = C_p/C_v$ is the ratio of the heat capacities for a gas, T is the temperature and r is the gas constant per unit mass. We note that the local speed of sound decreases as the tembilize and the expansion assumes the properties of a molecular beam.

Figure 1.3 gives another way to visualize the temperature changes in a supersonic expansion. Temperature in a gas is described by the width of a Maxwell-Boltzmann velocity distribution and the relatively wide peak centered at v = 0 is characteristic of a room temperature distribution. The second peak represents the velocity distribution along the axis of the expansion at some point downstream of the nozzle. The velocity distribution bilize and the expansion assumes the properties of a molecular beam.

Figure 1.3 gives another way to visualize the temperature changes in a supersonic expansion. Temperature in a gas is described by the width of a Maxwell-Boltzmann velocity distribution and the relatively wide peak centered at v = 0 is characteristic of a room temperature distribution. The second peak represents the velocity distribution along the axis of the expansion at some point downstream of the nozzle. The velocity distribution is now much narrower and is representative of a temperature far below room temperature. In addition $\langle v \rangle \neq 0$ indicating a mass flow.

From experimental data Ashkenas and Sherman[9] show that the Mach number can be described by the empirical relation

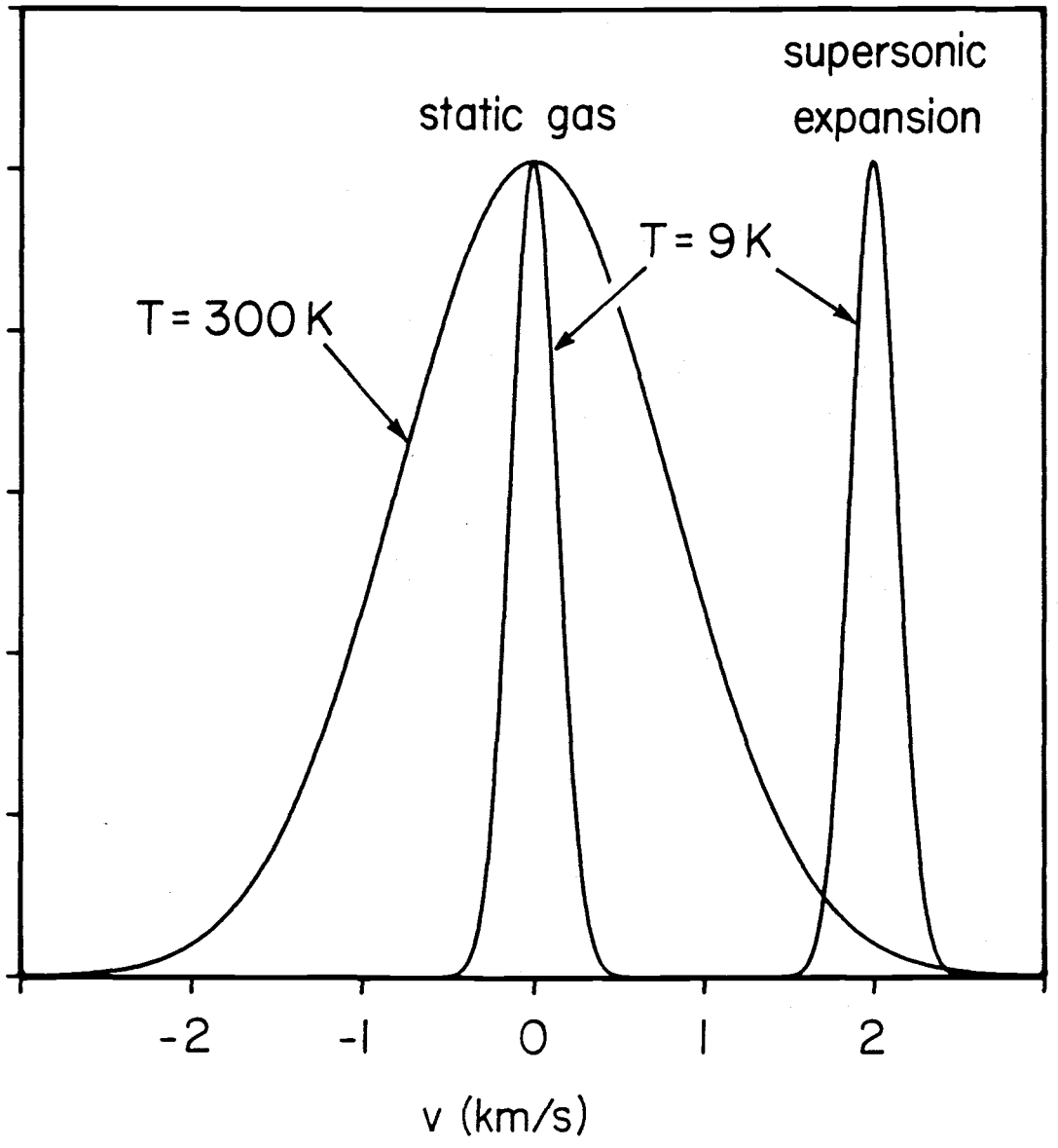

Figure 1.3 Distribution of velocities in equilibrium samples and supersonic expansion. One dimensional velocity distribution of static gas at 300 K and at 9 K and in supersonic expansion showing bulk flow.

$$M = A\left(\frac{X - X_0}{D}\right)^{\gamma-1} - \frac{1}{2}\left(\frac{\gamma + 1}{\gamma - 1}\right)\Big/A\left(\frac{X - X_0}{D}\right)^{\gamma-1} \qquad (1.4)$$

where A and X_0 are constants which depends upon γ and A is equal to 3.26 for a monatomic gas. X_0 is determined iteratively by a method detailed by Ashkenas and Sherman and is very close to the nozzle. X is the distance from the nozzle and D is the diameter of the nozzle. An estimation of the Mach number allows the temperature and density to be calculated using the formulae[8]

$$\frac{T}{T_0} = \left[1 + \left(\frac{\gamma-1}{2}\right)M^2\right]^{-1} \text{ and} \qquad (1.5)$$

$$\frac{\rho}{\rho_0} = \left[1 + \left(\frac{\gamma-1}{2}\right)M^2\right]^{1/(1-\gamma)} . \qquad (1.6)$$

Using Eq. (1.4 - 1.6) the temperature and density of an expansion of a monatomic gas can be calculated as a function of X/D. In a helium expansion seeded with a small percentage of CO_2, as discussed in chapter 3, the jet characteristics are determined by the helium and contributions due to the CO_2 can be ignored. Figure 1.2 shows a calculation of temperature and density as a function of X/D. This calculation was done using the equations presented above for the supersonic region ($X/D \geq \sim 1$) along with fitting formulae developed from a numerical solution using the method of characteristics[10] which model more closely the transonic regime ($-3 \leq X/D \leq \sim 1$). The calculation was done in a Symphony worksheet which was developed by Dr. Mark Maroncelli. It is clear that even relatively close to the jet, conditions are favorable for condensation of a species like carbon dioxide.

CLUSTERING IN JETS

Although using coherent Raman methods to study the clusters formed in supersonic jet expansions is relatively recent,[11,12,13] jets have been utilized to produce clusters for study by other methods since 1956.[14] Dorfeld and Hudson[15,16] conducted a study of condensation of CO_2 in free jet expansions using far field detection by mass spectrometry. Even more germane to this discussion are two publications by Hagena[17,18] which detail the size distribution of clusters of CO_2 with respect to source pressure, temperature and seeded inert carrier gas. Once again these studies were carried out in the far field in the region of molecular flow. Nonetheless, there is a clear indication in these works that conditions of high source pressure, low source temperature and seeding in an inert gas carrier all contribute to the formation of clusters. The study of carbon dioxide clusters in chapter 3 presents experimental data which support the conclusion that in the near field, close to the nozzle, similar conditions yield high concentrations of small clusters.

CHAPTER 2 -- THEORY

INTRODUCTION

The coherent Raman techniques share a basic theoretical development which has been covered thoroughly in a number of reviews and papers.[19-38] The purpose of this chapter is to establish a consistent theoretical framework upon which to base the subsequent discussions of the two coherent Raman methods which form the heart of this experimental work.

The starting point for a discussion of the interaction of light with matter is the classical description of electromagnetic waves by Maxwell's equations. These equations for bulk samples with no free charges and no magnetization in Gaussian units are:

$$\vec{\nabla} \times \vec{E} = - \frac{1}{c} \frac{\partial \vec{H}}{\partial t} \tag{2.1}$$

$$\vec{\nabla} \times \vec{H} = \frac{1}{c} \frac{\partial \vec{D}}{\partial t} \tag{2.2}$$

$$\vec{\nabla} \cdot \vec{D} = 0 \tag{2.3}$$

$$\vec{\nabla} \cdot \vec{H} = 0 \ . \tag{2.4}$$

The electric displacement $\vec{D}$ is related to the electric field vector by

$$\vec{D} = \vec{E} + 4\pi\vec{P} \tag{2.5}$$

where $\vec{P}$ is the electric polarization in the medium. Substituting Eq. (2.5) into Eq. (2.2) and substituting the result into the curl of Eq. (2.1) yields

$$\vec{\nabla} \times (\vec{\nabla} \times \vec{E}) + \frac{1}{c^2} \frac{\partial^2 \vec{E}}{\partial t^2} = - \frac{4\pi}{c^2} \frac{\partial^2 \vec{P}}{\partial t^2} \ . \tag{2.6}$$

We assume that the electric field and polarization will be the sums of functions with frequencies of the applied fields, of the sample resonances and of the various sum and difference frequencies:

$$E = \frac{1}{2} \sum_{j=1} \{E_j \exp[i(k_j z - \omega_j t)] + c.c.\} \tag{2.7}$$

$$P = \frac{1}{2} \sum_{j=1} \{P_j \exp[i(k_j z - \omega_j t)] + c.c.\} \tag{2.8}$$

where the waves are propagating in the z direction and E_j and P_j are the jth frequency components and c.c. is the complex conjugate. For a given frequency component ω_j the wave equation

$$\vec{\nabla} \times (\vec{\nabla} \times \vec{E}_j) - (\omega_j/c)^2 \vec{E}_j = 4\pi(\omega_j/c)^2 \vec{P}_j \tag{2.9}$$

gives the electric field response to an oscillating polarization. $\vec{P}$ responds to the driving electric field through the susceptibility $\vec{P} = \chi\vec{E}$ which is linear at low field intensity. In the presence of high field intensities the polarization no longer responds in a linear fashion and is represented by a series which explicitly shows the linear and the higher order terms. The expansion of the polarization is typically done in terms of the susceptibility

$$\vec{P} = \chi^{(1)} : \vec{E} + \chi^{(2)} : \vec{E}\vec{E} + \chi^{(3)} : \vec{E}\vec{E}\vec{E} + \ldots \tag{2.10}$$

where $\chi^{(n)}$ is the susceptibility tensor of rank n + 1.

In a transparent medium the linear susceptibility is related to the dielectric constant,

$$\varepsilon = 1 + 4\pi\chi^{(1)} \ . \tag{2.10}$$

The second order susceptibility, $\chi^{(2)}$ and all higher order even terms of the susceptibility vanish in isotropic media such as gases and liquids and in centrosymmetric crystals. However, $\chi^{(2)}$ is of great importance to spectroscopists in producing efficient second harmonic generation (SHG) in noncentrosymmetric crystals such as potassium dideuterium phospate, KD^*P, commonly used to produce 532 nm radiation from the 1.06 μm output of a Nd:YAG laser.

The third order susceptibility term, $\chi^{(3)}$, is the first nonlinear term which is nonzero for all media and which is responsible for the coherent Raman effects discussed in this thesis.

THIRD ORDER SUSCEPTIBILITY

The third order susceptibility or "chi-three" is a fourth order tensor containing the elements of the molecular resonance which can be probed by coherent Raman methods. Of the 81 elements of chi-three only 21 are nonzero in isotropic media.[34] Of these only three are independent, these are:

$$\chi^{(3)}_{1111}\ ,\quad \chi^{(3)}_{1122}\ ,\quad \chi^{(3)}_{1212}\ ,\quad \text{and}\quad \chi^{(3)}_{1221} \tag{2.11}$$

with

$$\chi^{(3)}_{1111} = \chi^{(3)}_{1122} + \chi^{(3)}_{1212} + \chi^{(3)}_{1221}\ . \tag{2.12}$$

Levenson[35] has tabulated the specific susceptibility element probed using various orientations of polarization for the CARS technique and for the stimulated Raman techniques. For the CARS and inverse Raman experiments where the polarizations of the input beams are all oriented parallel to one another only $\chi^{(3)}_{1111}$ contributes to the observed signal.

This was the polarization orientation used in all of the experiments discussed in this thesis. Nibler and Knighten have shown that, in particular,

$$\chi^{(3)}_{CARS} = 3\chi_{1111}(\omega_1, \omega_1, -\omega_2) \quad \text{and} \tag{2.13}$$

$$\chi^{(3)}_{RAM} = 6\chi_{1111}(\omega_2, \omega_1, -\omega_1) \quad ; \tag{2.14}$$

hence $\chi^{(3)}_{1111}$ is the susceptibility of greatest immediate interest.

At the molecular level Nibler and Knighten have shown that the relationship between the CARS and the Raman susceptibilities at resonance with a Raman allowed transition is

$$\chi^{(3,mol)}_{\alpha\beta\gamma\delta}(\omega_1,\omega_1,-\omega_2)peak = -2\chi^{(3,mol)}_{\alpha\beta\gamma\delta}(\omega_2,\omega_1,-\omega_1)peak \tag{2.15}$$

In addition they have shown that, after orientational averaging to link the molecular with the laboratory frame of reference, the relationship expressed in Eq. (2.15) holds for $\chi^{(3)}(\omega_1,\omega_1,-\omega_2)$ and $\chi^{(3)}(\omega_2,\omega_1,-\omega_1)$ of the bulk sample in the laboratory frame. The differential Raman cross section per molecule is given by[34]

$$\frac{d^2\sigma}{d\Omega d\omega_2} = \frac{-4\hbar n_2 \omega_2^4}{n_1 \pi c^4 (N_n - N_k)} \, Im\chi_{RAM} \tag{2.16}$$

where $Im\chi_{RAM}$ is the imaginary part of the Raman susceptibility. Eq. (2.15) details the peak susceptibility and it is related to the integrated susceptibility as follows

$$\int_{-\infty}^{\infty} Im\chi^{(3,mol)} d(\delta\omega) = \pi\Gamma_{kn} Im\chi^{(3,mol)}(peak) \tag{2.17}$$

where Γ_{kn} is the half width of the normal Raman transition $|k\rangle \leftarrow |n\rangle$. Eq. (2.16) can be used along with Eq. (2.15) and Eq. (2.17) to

establish the relationship between the differential Raman cross section and the CARS and Raman susceptibilities. The differential Raman cross section expressed in terms of $\chi^{(3)}_{CARS}$ is

$$\frac{d\sigma}{d\Omega} = \int_{-\infty}^{\infty} \left(\frac{d^2\sigma}{d\Omega d\omega}\right) d\omega = \frac{2\hbar n_2 \omega_2^4 \Gamma_{kn}}{n_1 c^4 (N_n - N_k)} \chi^{(3)}_{CARS}(\text{peak}) \ . \tag{2.18}$$

We solve Eq. (2.18) for $\chi^{(3)}_{CARS}$ and include the frequency response term $\omega_{kn}+\omega_1-\omega_2$ and obtain

$$\chi^{(3)}_{CARS} = \frac{n_1 c^4 (N_n - N_k)}{2\hbar n_2 \omega_2^4} \left(\frac{d\sigma}{d\Omega}\right) \frac{1}{\omega_{kn}-\omega_1+\omega_2+i\Gamma_{kn}} + \chi_{NR} \ . \tag{2.19}$$

This is the fundamental susceptibility equation for the CARS process. $N_n - N_k$ is the difference in the number density between the lower and the upper states of the Raman transition and $(d\sigma/d\Omega)$ is the ordinary differential Raman cross section. The Raman susceptibilty follows a similar development starting from Eq. (2.16)

$$\frac{d\sigma}{d\Omega} = \int_{-\infty}^{\infty} \left(\frac{d^2\sigma}{d\Omega d\omega}\right) d\omega = \frac{-4\hbar n_2 \omega_2^4 \Gamma_{kn}}{n_1 c^4 (N_n - N_k)} \chi^{(3)}_{RAM}(\text{peak}) \ . \tag{2.20}$$

Once again we solve for the susceptibility term and find

$$\chi^{(3)}_{RAM} = \frac{n_1 c^4 (N_n - N_k)}{-4\hbar n_2 \omega_2^4} \left(\frac{d\sigma}{d\Omega}\right) \frac{1}{\omega_{kn}-\omega_1+\omega_2+\Gamma_{kn}} \ . \tag{2.21}$$

One important difference between the CARS and the inverse Raman susceptibilites is that in the case of CARS both the real and the imaginary parts of the susceptibility contribute to the observed signal. In contrast, only the imaginary part of the susceptibility is observed in the inverse Raman technique. For this reason it is useful to separate Eq. (2.21) into its real and imaginary components.

$$\text{Re}\chi^{(3)} = \frac{n_1 c^4 (N_n - N_k)}{-4\hbar n_2 \omega_2^4} \frac{(\omega_{kn}-\omega_1+\omega_2)}{(\omega_{kn}-\omega_1+\omega_2)^2 + \Gamma_{kn}^2} + \chi_{NR} \tag{2.22}$$

$$\mathrm{Im}\chi^{(3)} = \frac{n_1 c^4 (N_n - N_k)}{-4\hbar n_2 \omega_2^4} \frac{i\Gamma_{kn}}{(\omega_{kn} - \omega_1 + \omega_2)^2 + \Gamma_{kn}^2} \tag{2.23}$$

The real part of the susceptibility, Eq. (2.22), is responsible for the change of index of refraction as a function of intensity and explains the self-focussing behavior which is observed in high intensity laser beams.[27] Eq. (2.23) details the susceptibility term which is used to calculate the inverse Raman signal. In addition to the resonant parts of the susceptibility, a real, nonresonant susceptibility, χ_{NR} in Eqs. (2.19) and (2.22), exists for all samples. χ_{NR} is a slowly varying function with respect to frequency and is normally orders of magnitude smaller than the resonant susceptibility. All molecules in a sample contribute to the nonresonant susceptibility which is essentially the electronic polarizability of the sample.

It is important to note that χ_{NR} only contributes to the CARS susceptibility and that the inverse Raman technique is free of this interference. In some cases where the species of interest is in low concentration, χ_{NR} can alter the appearance of the CARS spectrum. This is particularly true for studies of combustion gases and is of concern in this work for some of the low concentration studies described in Chapter 3.

GAIN EQUATION FOR STIMULATED RAMAN SCATTERING

Inverse Raman spectroscopy (IRS) and Raman gain spectroscopy (RGS) are complementary techniques which both fall under the designation stimulated Raman scattering. As described in Chapter 1 there is a one to one correspondence between the increase in the intensity of the

Stokes beam and the decrease in the intensity of the pump beam. The equations for the gain in the Raman gain experiment apply equally well to the inverse Raman experiment with only a change in sign.

The linear polarization term $\vec{P}^{(1)}$ can be written utilizing Eq. (2.11)

$$\vec{P}^{(1)} = \chi^{(1)}\vec{E}_j = ([\varepsilon_j - 1]/4\pi)\vec{E}_j \ . \tag{2.24}$$

Expanding Eq. (2.24) and adding the third order nonlinear term yields

$$\vec{P} = \varepsilon_j\vec{E}_j/4\pi - \vec{E}_j/4\pi + \vec{P}^{(3)} + \ldots \ . \tag{2.25}$$

Substituting Eq. (2.25) into Eq. (2.9) and using the vector identity $\vec{\nabla}\times(\vec{\nabla}\times\vec{E}) = \vec{\nabla}(\vec{\nabla}\cdot\vec{E}) - \vec{\nabla}^2\vec{E}$ one obtains

$$\frac{\partial^2\vec{E}}{\partial z^2} + \left(\frac{\omega}{c}\right)^2 \varepsilon_j\vec{E}_j = -4\pi\left(\frac{\omega}{c}\right)^2\vec{P}^{(3)} \tag{2.26}$$

for a wave propagating in the z direction. If we use the definitions of index of refraction, $\varepsilon = n^2$, and the magnitude of the wave vector, $k_j = n_j\omega_j/c$, Eq. (2.26) can be evaluated for the jth component of the field expressed in Eq. (2.7).

$$-k_1^2 + \left(\frac{\omega_1 n_1}{c}\right)^2 = -2\pi\left(\frac{\omega_1}{c}\right)^2\chi^{(3)}_{RAM}|E_2|^2 \tag{2.27}$$

The indices are consistent with those for the CARS expression. The Stokes beam, ω_2, is the modulated or pulsed laser while the pump beam, ω_1, which is normally a cw or quasi-cw beam, is monitored as the probe in the inverse Raman experiment.

Eq. (2.27) is solved for k_1 in terms of the intensity using the relation $I = (nc/8\pi)|E|^2$.

$$k_1 = k_1^0[1 + (16\pi^2/n_1^2 n_2 c)\chi^{(3)} I_2]^{\frac{1}{2}} \tag{2.28}$$

where $k_1^0 = \omega_1 n_1/c$. Eq. (2.28) can be approximated using the series expansion $(1 + x)^{\frac{1}{2}} = 1 + \frac{1}{2}x + \ldots$ and truncating after the second term.

$$k_1 = k_1^0[1 + (8\pi^2/n_1^2 n_2 c)\chi^{(3)} I_2] \tag{2.29}$$

Eq. (2.29) can be separated into real and imaginary parts, $k_1 = \mathrm{Re}k_1 + i\mathrm{Im}k_1$ with the appropriate parts of the susceptibility $\chi^{(3)}_{RAM}$,

$$k_1 = k_1^0[1 + (8\pi^2/cn_1^2 n_2)(\mathrm{Re}\chi + \chi_{NR})I_2] + ik_1^0[(8\pi^2/cn_1^2 n_2)(\mathrm{Im}\chi)I_2] \quad . \tag{2.30}$$

Eq. (2.30) can be substituted into the jth field component of Eq. (2.7) which yields a product of two terms

$$E_1(z) = \tfrac{1}{2}\{[\tilde{E}_1(z)\exp[i(k_1^0 z - \omega_1 t)] \times [\text{Real Term}] + \text{c.c.}\} \tag{2.31}$$

where

$$\tilde{E}_1(z) = E_1^0 \exp[-k_1^0(8\pi^2/cn_1^2 n_2)(\mathrm{Im}\chi)I_2 z] \tag{2.32}$$

is the amplitude of the probe beam as a function of z. Converting Eq. (2.32) to intensity gives the gain equation

$$I_1(z) = I_1^0 \exp[-k_1^0(16\pi^2/cn_1^2 n_2)(\mathrm{Im}\chi)I_2 z] = I_1^0 e^{gz} \tag{2.33}$$

where the coefficient of gain is

$$g = -(16\pi^2 k_1^0/cn_1^2 n_2)(\mathrm{Im}\chi)I_2 \quad . \tag{2.34}$$

Under normal circumstances $gz \ll 1$ and the approximation

$$I_1(z) \simeq I_1^0(1 + gz) \tag{2.35}$$

is valid, yielding our desired expression for the change in probe beam intensity,

$$\delta I_1 = gzI_1^0 = (-16\pi^2\omega_1/cn_1^2n_2)(Im\chi)I_2I_1z \ . \tag{2.36}$$

Eq. (2.36) provides useful information about the inverse Raman experiment. One can easily see the linear dependence of the signal upon the probe intensity, I_1, the pump intensity, I_2 and the susceptibility. In addition, since the signal is the product of the two input beams, it is clear that significant enhancement of the signal is possible by focussing the input beams. An approximation of a focussed Gaussian beam enables Eq. (2.36) to be cast in terms of the powers of the beams. For a focussed Gaussian beam the minimum beam diameter is $w_0 = 4\lambda f/\pi w$ where f is the focal length of the focussing lens and w is the diameter of the beam at the lens. The interaction length z is set equal to the confocal parameter $b = \pi w_0^2/2\lambda$ and the intensities are converted to powers by $I_i = p_i[1/\pi(w_0/2)^2]$. The resulting equation

$$\delta p_1 = (-16\pi^2\omega_1/cn_1^2n_2)(Im\chi)p_2p_1(2/\lambda) \tag{2.37}$$

indicates among other things that the signal is independent of the focal length of the focussing lens. It is found experimentally that this is a good approximation although the conditions of the experiment vary considerably from those assumed. The most significant deviation is the assumption of colinearity of the probe and Stokes beams. Most

experimental arrangements utilize a crossed beam geometry which allows the probe beam to be spatially isolated. The resulting signal is found to be a very sensitive function of the crossing angle.

We note that Eq. (2.30 - 2.36) can be applied equally well to the Raman gain experiment or to the inverse Raman experiment by using the appropriate form for the susceptibility. Jones[40] has indicated that the imaginary part of the susceptibility changes sign on the interchange of frequencies ω_1 and ω_2. The sign of the susceptibility and hence signal gain or loss therefore depends upon which beam is being observed.

THE CARS SIGNAL

The amplitude of the CARS signal can be derived starting with Eq. (2.26) and substituting in the CARS susceptibility.

$$\frac{\partial^2 E}{\partial z^2} + \left(\frac{\omega}{c}\right)^2 \varepsilon E = -4\pi\left(\frac{\omega}{c}\right)^2 \chi^{(3)}_{CARS} |\vec{E}_1|^2 \vec{E}_2$$

$$= -4\pi\left(\frac{\omega}{c}\right)^2 \chi^{(3)}_{CARS} E_1^2 E_2 \exp[i(2k_1 - k_2)z] \qquad (2.38)$$

If we assume a solution

$$\vec{E} = \hat{e}_{CARS} E_3^0 \exp[ik_3 z] \qquad (2.39)$$

where $\hat{e}_{CARS}$ is the unit polarization vector in the direction of the CARS field then Eq. (2.38) becomes

$$\frac{\partial^2 E_3}{\partial z^2} + 2ik_3 \frac{\partial E_3}{\partial z} - E_3^0 k_3^2 = -4\pi\left(\frac{\omega_3}{c}\right)^2 \chi_{CARS} E_1^2 E_2 \exp(i\Delta k z) \qquad (2.40)$$

where $\Delta k = 2k_1 - k_2 - k_3$. We assume that Δk is small and that E_3^0 is a slowly varying function of z so that the second derivative can be

neglected. Integrating Eq. (2.40) and assuming that $E_3^0 = 0$ at $z = 0$ yields

$$E_3^0 = \frac{2\pi\omega_3}{n_3 c} \chi^{(3)}_{CARS} E_1^2 E_2 (\exp[i\Delta kz]-1)/\Delta k \ . \tag{2.41}$$

Converting the electric field to intensity

$$I_3 = \frac{256\pi^4\omega_3^2}{n_1^2 n_2 n_3 c^4} |\chi^{(3)}_{CARS}|^2 I_1^2 I_2 L^2 \left(\frac{\sin(\Delta kL/2)}{\Delta kL/2}\right)^2 \tag{2.42}$$

Eq. (2.42) shows the quadratic dependency of the CARS signal upon the susceptibility and the pump intensity. Due to the $I_1^2 I_2$ dependence, large I_3 signals can be achieved by focussing the pump and Stokes beams. The phase matching condition mentioned in the first chapter goes to 1 in the limit $\Delta k \to 0$.

In a manner similar to that for the inverse Raman development Eq. (2.42) can be converted to show the power relationships. Once again the Gaussian limits for a focussed beam are utilized,

$$P_3 \simeq \left(\frac{2}{\lambda}\right)^2 \frac{256\pi^4\omega_3^2}{n_1^2 n_2 n_3 c^4} |\chi^{(3)}_{CARS}|^2 P_1^2 P_2 \ . \tag{2.43}$$

Eqs. (2.37) and (2.43) clearly illustrate the differences between the CARS technique and the inverse Raman experiment. The essential differences can be summarized as follows: The CARS signal has a quadratic dependence upon the number density difference and upon the pump power, ω_1. In addition, since signal is derived from the square of the real and imaginary susceptibility, any significant nonresonant real contribution will cause a distortion of the lineshapes. The real part also causes distortion of the lineshape when two peaks are adjacent to one another.[41] Detection techniques for CARS are inherently more sensitive because the signal is essentially an emission

which can be detected with a photomultiplier.

The inverse Raman signal is linear in number density difference and power in the two beams and responds to only the imaginary part of chi-three. Thus IRS has an advantage at low sample concentrations and it produces lineshapes and peak frequencies identical to those of spontaneous Raman spectroscopy. Offsetting this advantage is the fact that the inverse Raman signal is essentially slight absorption of an intense coherent beam. Detection of this absorption is inherently less sensitive than the methods used for CARS. Additional advantages of IRS include less problem with spectral distortion caused by the high power required for the CARS experiment. These include saturation effects ($N_n - N_k \rightarrow 0$), and the optical Stark effect.[60] It is also more straightforward to construct a high resolution IRS system using stable, narrow linewidth ion lasers and ring dye lasers. A description of the experimental CARS setup used to probe the carbon dioxide dimer in the supersonic jet is included in chapter 3. Chapter 4 gives a detailed description of the IRS spectrometer which was designed to enable very high resolution spectroscopy in supersonic jets.

CHAPTER 3 -- CARS STUDY OF CO_2 DIMER

INTRODUCTION

The study of intermolecular forces has been the focus of considerable theoretical and experimental work over the years. The elucidation of intermolecular forces allows many properties of the bulk material to be calculated from statistical mechanics. Of equally fundamental interest is the calculation of gas transport coefficients and rotational relaxation times.[42] These weak forces include electrostatic (dipole-dipole) interactions, induced dipole interactions and dispersion forces which, as a whole, are referred to as van der Waals forces. They are, in general, about two orders of magnitude weaker than normal covalent forces.[43]

As with chemical bonds, van der Waals forces form a potential energy well with a smaller but still significant energy minimum. These weak but long range forces will only favor the formation of complexes at low temperatures where thermal dissociation is minimized. Polyatomic molecules exhibit a significant anisotropy to what is now called the potential surface so that a molecular shape has meaning for such complexes. The anisotropic part of the potential also bears upon collisional rotational relaxation as well as upon orientational aspects of crystal structure.[44]

The spectroscopic study of van der Waals dimers can yield binding energy, structural information and vibrational predissociation lifetimes which are, in turn, of considerable use in mapping out the potential surface. When dimers are studied in the gas phase as in a supersonic jet expansion, the pair potential energy surface that is

determined is unperturbed by surrounding atoms or molecules and can provide more useful data for comparison with theory.

In addition, dimers and small clusters are important in the complex chemistry and dynamics of the low pressure, low temperature region of the upper atmosphere. The stability of the ozone layer and the chemistry of atmospheric pollution, for example, are influenced by the weak but long range van der Waals interactions.[45]

This chapter presents a CARS study of the dimer and small clusters of carbon dioxide produced in a supersonic jet expansion. While the monomer of carbon dioxide has been the object of many studies, there has been little work on the dimer until recently. In 1971 Mannik et al.[46] achieved the first spectroscopic observation of the dimer with an infrared study of CO_2 using a multipass one meter gas cell at -80 °C. This study centered on the infrared inactive ν_1 band of CO_2, made infrared allowed, albeit weak, by the change of symmetry associated with the formation of the dimer. Based upon the band maxima of a PQR structure near the ν_1 line they proposed a T-shaped structure for the dimer with a C···C separation of 4.1 Å.

In 1973, Novick and coworkers[47] observed 1% refocusing of $(CO_2)_2$ in a molecular beam electric deflection experiment; an observation consistent with a polar, T-shaped structure. An infrared study of the CO_2 dimer in an argon matrix by Fredin et al.[48] (1974) showed features consistent with a T-shaped structure lacking a center of symmetry. Also in 1974, Hashimoto and Isobe[49] concluded that the T-shaped structure represented the minimum energy structure in a CNDO/2 calculation where the intermolecular distance was fixed at 4.1 Å.

However, also in 1974, an empirical calculation in 1974 by Koide

and Kihara,[50] in which the intermolecular distance was allowed to vary, yielded two potential wells. One, the T-shaped structure, had a minimum at a distance of 4.5 Å while the other, an offset parallel structure, had a minimum at 3.8 Å. In addition, the minimum in the potential well of the offset parallel structure was 50% deeper than that for the T-shaped structure. This was the first evidence that the most stable structure for $(CO_2)_2$ might be an offset parallel configuration with C_{2h} symmetry. In 1977 Brigot et al.[51] considered two empirical potentials, CNDO/2, and ab initio calculations to further refine the structural predictions for $(CO_2)_2$. Their calculations support the conclusions of Koide and Kihara that the offset parallel form represents the most stable form of the dimer and that both forms may be present in the gas at low temperatures. Figure 3.1 illustrates these two favored structures.

Guasti, Schettino and Brigot[52] (1978) extended the matrix isolation infrared work of Fredin and coworkers by studying CO_2 trapped in Kr and Xe matrices as well as Ar. Their observations confirm the spectra previously observed in the Ar matrix but indicate that Kr and Xe matrices yield simpler spectra consistent with a dimer species with a center of symmetry. They suggest that only the nonpolar dimer is present in all three matrices but that in the argon matrix the dimer can be trapped in two different sites thus explaining the additional peaks.

In 1979 Barton and coworkers[53] reinvestigated $(CO_2)_2$ using the molecular beam electric deflection technique. This experiment differed from the previous neat CO_2 study in that a 5% CO_2 in Ar mixture was expanded through the nozzle to facilitate cooling. They

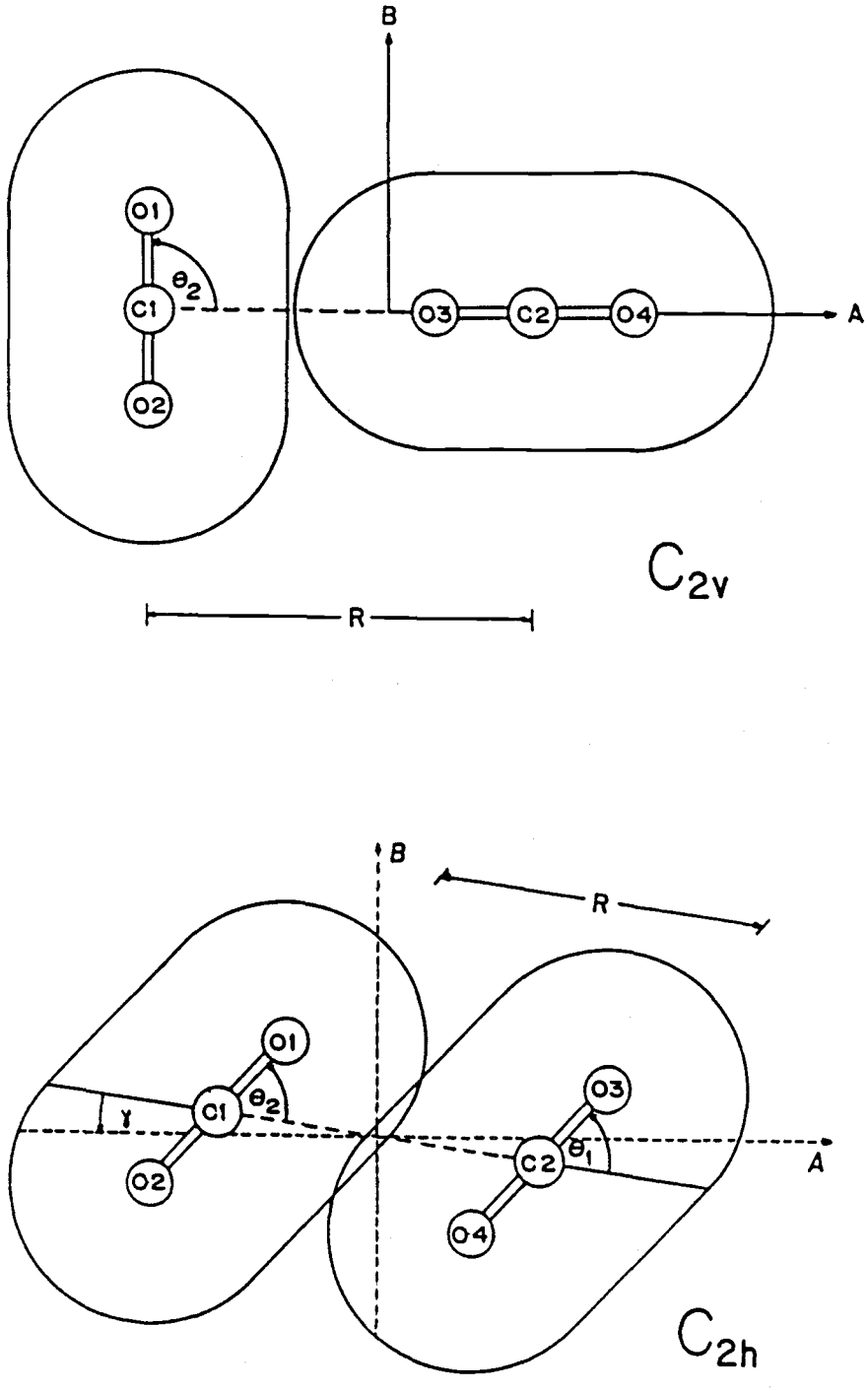

Figure 3.1 Two proposed structures of the CO_2 dimer. (adapted from Ref. 54). In (a) R = 4.1 Å and in (b) R = 3.7 Å.

noted that at very low temperatures, when polymers containing argon were produced, that there was a slight indication of refocusing of the dimer. They ascribed this observation to fragmentation of higher order polymers in the mass spectrometer and concluded that, since there was no refocusing of the dimer, it must have the nonpolar, offset parallel structure with a center of symmetry.

In 1981 Kopec[54] took another look at the long-path, cold spectrum of $(CO_2)_2$ using FTIR with a resolution better than 0.4 cm^{-1}. In this study he was able to resolve and subtract the individual R-branch lines of naturally occurring $^{12}C^{16}O^{18}O$ monomer (0.4%) overlying the unresolved PQR envelope of the CO_2 dimer. Kopec concluded, as had Guasti, that the displacement of the P and R branches from the Q branch did not yield an unequivocal assignment of structure deduced by Mannick et al. As a consequence Kopec concluded that the IR data were not inconsistent with the growing body of evidence favoring the nonpolar structure.

Gough, Miller and Scoles[55] (1981) published the results of a molecular beam infrared vibrational predissociation study of $(CO_2)_2$ which identified dimer peaks in the $\nu_1+\nu_3$ and the $2\nu_2+\nu_3$ combination band region. This peak of a 10% CO_2 in He was fairly broad with a half width of of about 1.7 cm^{-1}. It also appeared that there was underlying structure as evidenced by the uneven band contour. An additional observation was made that the peak showed a smooth red shift as conditions were created which favored higher clusters. Miller and Watts[56] extended this work in 1984 with the publication of a small region of the $\nu_1+\nu_3$ dimer band at very high resolution. Their spectra of dilute CO_2 expansions gave evidence for

highly resolved rotational fine structure in high pressure expansions of 2% CO_2 in He. A maximum scan width of 0.05 cm^{-1}, however, limited their ability make rotational assignments and hence to reach structural conclusions.

In 1984, Lobue, Rice and Novick[57] did a third molecular beam electric deflection experiment and attributed the apparent lack of refocusing of $(CO_2)_2$ in the study of Barton et al. to swamping of the refocusing signal by the nonpolar $(CO_2)_3$ and higher polymers. They were led to this conclusion by observing that the refocusing signal increased as the stagnation pressure behind the nozzle was decreased. This increase also followed the observed decrease in the intensity of mass peaks corresponding to $(CO_2)_3^+$ and higher order clusters relative to the dimer. This result supports the assertion that a significant proportion of the dimer has the T-shaped, polar structure. We note that this conclusion is not inconsistent with the calculations of Koide and Kihara and Brigot et al. which predict that there is a low potential barrier between the T-shaped and the more stable offset parallel form so that some thermal production of the former could occur even in the low temperature jet.

No Raman data existed for the dimer although Kopec attempted a Raman investigation of the ν_3 asymmetric stretch region of CO_2. This mode is Raman forbidden in the monomer but it was hoped that, in the dimer, the perturbed ν_3 band would become visible and offer further insight regarding the structure of the dimer. Unfortunately, no band was observed due to the low dimer concentration and the inherent insensitivity of spontaneous Raman spectroscopy.

Jet expansions and coherent Raman techniques offer hope in this

respect and stimulated this study. In this chapter we report the resultant spectra of the dimer band in the ν_1 symmetric stretch region which, along with the previous FTIR spectra, enable an unequivocal assignment of the structure of the CO_2 dimer.

EXPERIMENTAL

The experiment utilizes the technique of pulsed Coherent Anti-Stokes Raman Scattering (CARS) to probe molecular species in a cooled, pulsed supersonic jet expansion. The CARS spectrometer, depicted in Figure 3.2, consists of pulsed, unstable resonator Nd:YAG laser (Quanta-Ray DCR-1A) the 1.06 μm output of which is doubled by means of second harmonic generation in a KD^*P (Type II) crystal. The resulting 532 nm beam is split to pump a pulsed dye laser (Quanta-Ray PDL-1) and provide the two ω_1 pump beams. The output of the dye laser (ω_2) is mixed in the sample with the two ω_1 beams at their common focus using the three dimensional phase matching arrangement (folded BOXCARS) Figure 3.3a. The momentum vectors for the three input beams and the CARS beam must sum to zero for proper phase matching as depicted in Figure 3.3b. The dye laser is tuned by rotating a grating which functions as the rear high reflector of the oscillator cavity. The grating is controlled with a stepper motor and uses either the fourth or fifth order reflection with a tuning rate of 0.03 or 0.024 Å per step respectively. Most of the spectra were recorded with an overall resolution of 0.3 cm^{-1} using the grating in the fifth order.

The high resolution CARS spectra reported in this chapter utilize an optional intracavity air spaced étalon which, along with the dye laser grating, is housed in a sealed pressure chamber. In this mode

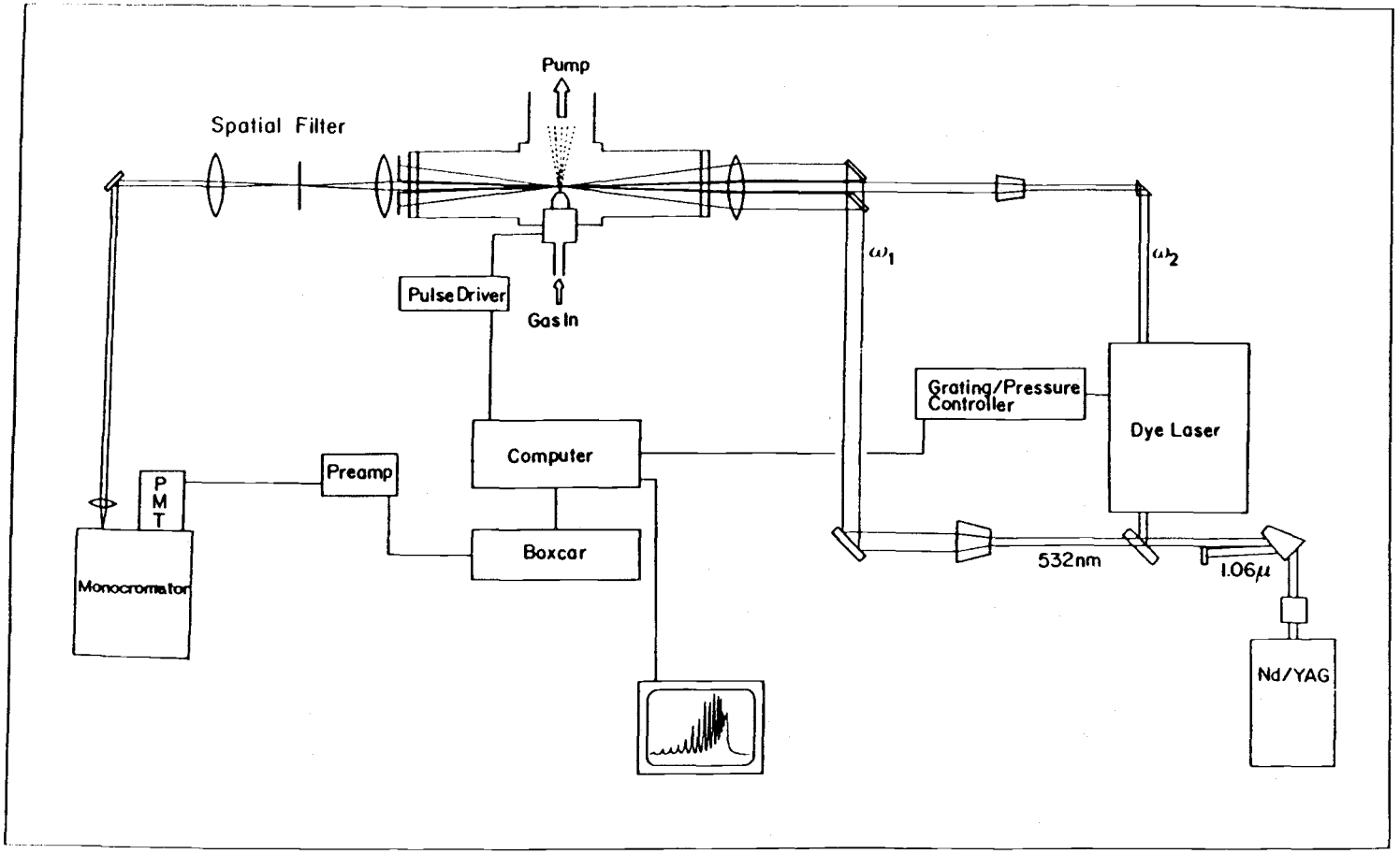

Figure 3.2 Schematic of the CARS apparatus.

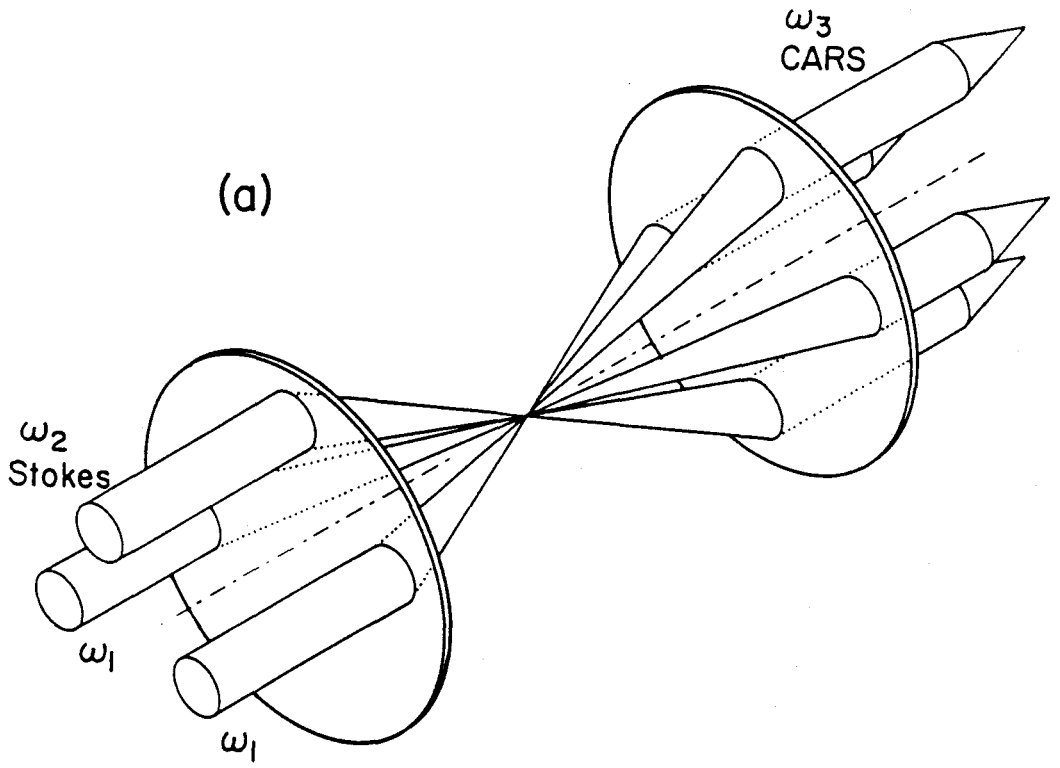

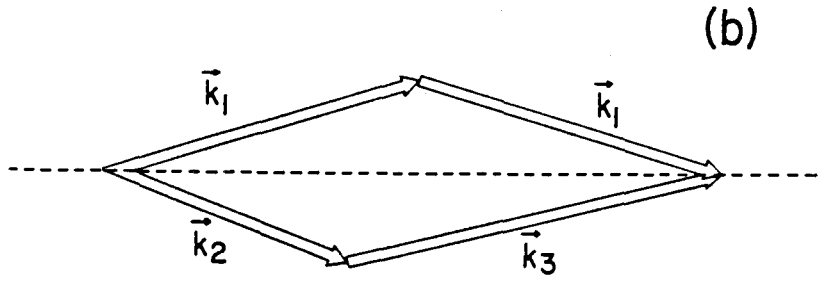

$$|k_i| = n_i \omega_1 / c$$

Figure 3.3 Three dimensional phase matching in the CARS experiment. (a) gives physical orientation of input and CARS beams, (b) is the vector condition necessary to achieve $\Delta k = 0$.

the dye laser has a linewidth of 0.05 cm^{-1} and can be tuned by adjusting the pressure within the chamber. The advantage of this method is that since the grating and the étalon see the same refractive index, these two elements "track" together as the pressure inside the chamber is adjusted and the laser will tune smoothly with no étalon mode hops. Using N_2 the laser can be tuned 10 cm^{-1} by varying the pressure from 0 to 2 atm. There is an insertion loss of 30 to 50% of the dye laser power with the addition of the air spaced étalon.

The pump source used for the high resolution CARS experiments was a doubled Nd:YAG (Molectron MY34-10) with a single-mode option (MY-SAM). This laser has a pulse width of 20 ns and achieves single-mode operation on most shots. The longer pulse width of this laser results in a lower peak power and consequently the efficiency in pumping a dye laser and the field intensities at the focus are lower. Thus there were significant sacrifices in signal intensity when operating in the high resolution mode.

The CARS signal in the three dimensional phase matching geometry is spatially separate from the co-propagating input beams and can, in large part, be isolated with a simple aperture. Remaining stray light is removed by spatial filtering through a pinhole and dispersion with a 0.3 m monochromator (McPherson 218). The signal is detected with a RCA 31032A photomultiplier operating at 1750 V, amplified with either one or, in the case of very low signal levels, two fast 10× video amplifiers (Cominear Corp. CLC 100). This 10 ns signal was captured with a gated integrator (Stanford Research Systems SR 250) and averaged with a minicomputer (DEC Micro-11).

The cooled, pulsed nozzle required for these experiments is based

upon a commercially available BMW fuel injector valve (Bosch Type 0 280 150 152) which has been extensively modified. Figure 3.4a is a cut away illustration of the unmodified Bosch valve. Several versions of this valve were used during the course of this investigation as repeated attempts were made to overcome the low temperature/high pressure limitations of the stock valve. Initially the valves were modified by soldering a 0.25 mm stainless-steel shim onto the injector head and grinding away the excess material to form a conical tip which was then drilled with the desired hole size (0.1 to 0.5 mm). The valve body was threaded to allow mounting in the sample chamber. Figure 4.4b shows the initial "room temperature" modifications to the valve.

During the CO_2 investigation it became apparent that in order to achieve adequate condensation in the jet it was necessary to cool the gas mixture prior to expansion. A dewar assembly was constructed which permitted the valve body to be submerged in a cold slush bath. The valve as modified above would function properly down to a temperature of 245 K but at lower temperatures the sealing O-rings within the body would lose elasticity and the valve would experience severe leaks. The highest pressure at which this modified valve would function was 12.2 atm; at higher pressures the valve would stop pulsing.

The valve was further modified to allow colder temperature operation. The back of the valve body was cut open on a lathe and the back of the valve was faced flat, removing the gas feed tube and the external electrical connectors. A brass housing was constructed which completely surrounded the modified valve body and a seal was effected with indium wire fitted into a groove formed between the cylindrical part of the valve body, the modified back of the valve and the back of

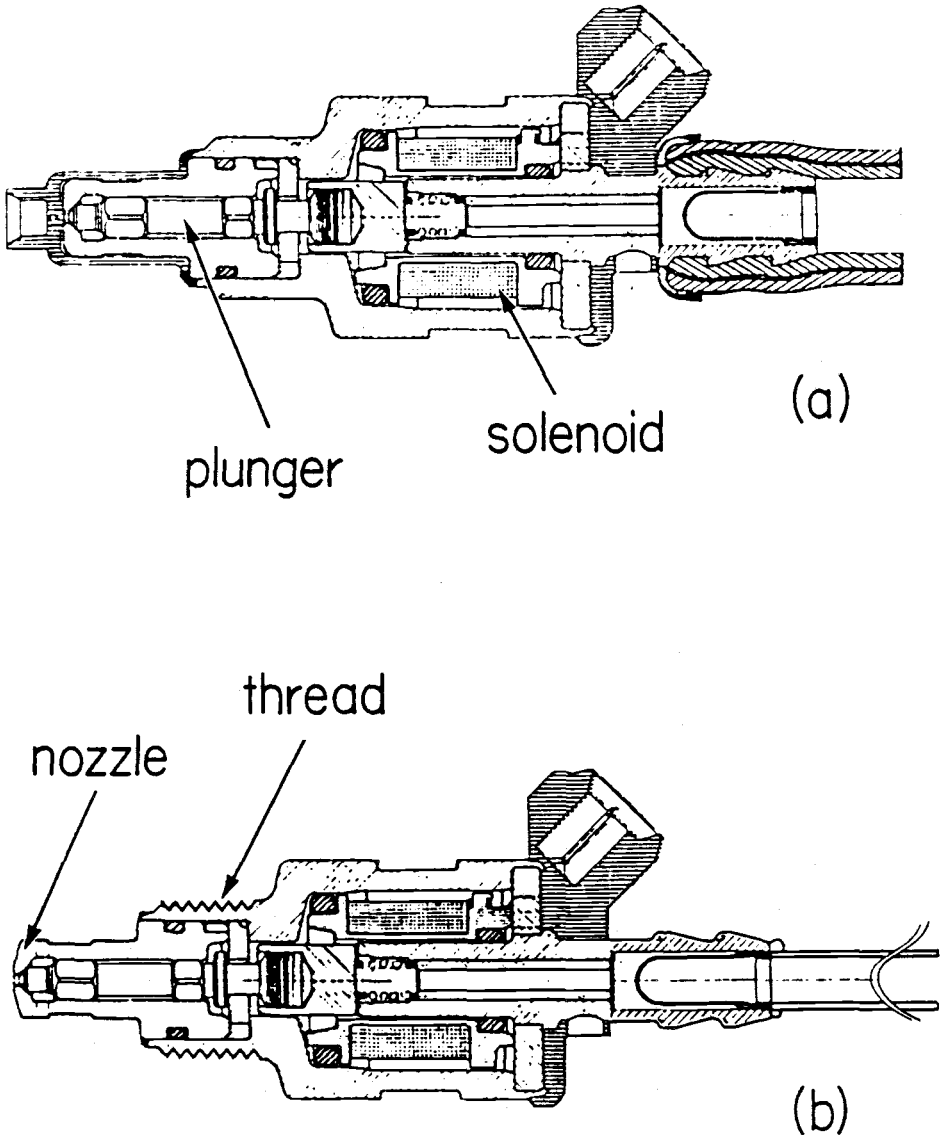

Figure 3.4 Modification of BMW injector valve for use as a pulsed supersonic jet. A cutaway drawing of the unmodified valve is shown in (a) and the initial room temperature modifications are shown in (b). (from Bosch)

the brass housing. (see Figure 3.5) The lower portion of the valve was sealed by soldering the body to the brass housing. With this setup the valve has been operated down to a temperature of 77 K and has also pulsed reliably up to 110 atm. Figure 3.6 depicts the placement of the modified valve in the dewar assembly mounted to the cell.

The sample cell was constructed with a 83x83x93 mm block of aluminum machined with ports to allow mounting of the pulsed valve/dewar assembly, a bellows connection to a cold trap with a 300 liter/minute rotary pump, 143 mm long cylindrical cell window extensions, and an observation window. The entire assembly was mounted upon a XYZ stage to allow precise alignment of the jet relative to the laser beams.

Electrical timing of the experiment is depicted in the schematic in Figure 3.7. Figure 3.7a shows the timing for the experiment using the Quanta-Ray system. The internal 10 Hz oscillator in the Quanta-Ray produces an electrical pulse approximately 3 ms prior to the firing of the Q-switch and the laser pulse. This signal is used to trigger a pulse generator (Hewlett-Packard model 222A) which provides a variable width output pulse after an adjustable delay. This output pulse triggers a specially constructed driver which opens the pulsed nozzle. The nominal width of the gas pulse was 1 ms. The delay of the HP pulse generator was adjusted such that the laser pulse arrived shortly after the pulsed valve reached its full open condition. This was done to avoid the possibility of taking spectra under conditions where the free jet zone was collapsing through the sampling region as the background pressure rose. In all probability this was an unnecessary precaution since the region of the jet sampled was out at most a few nozzle

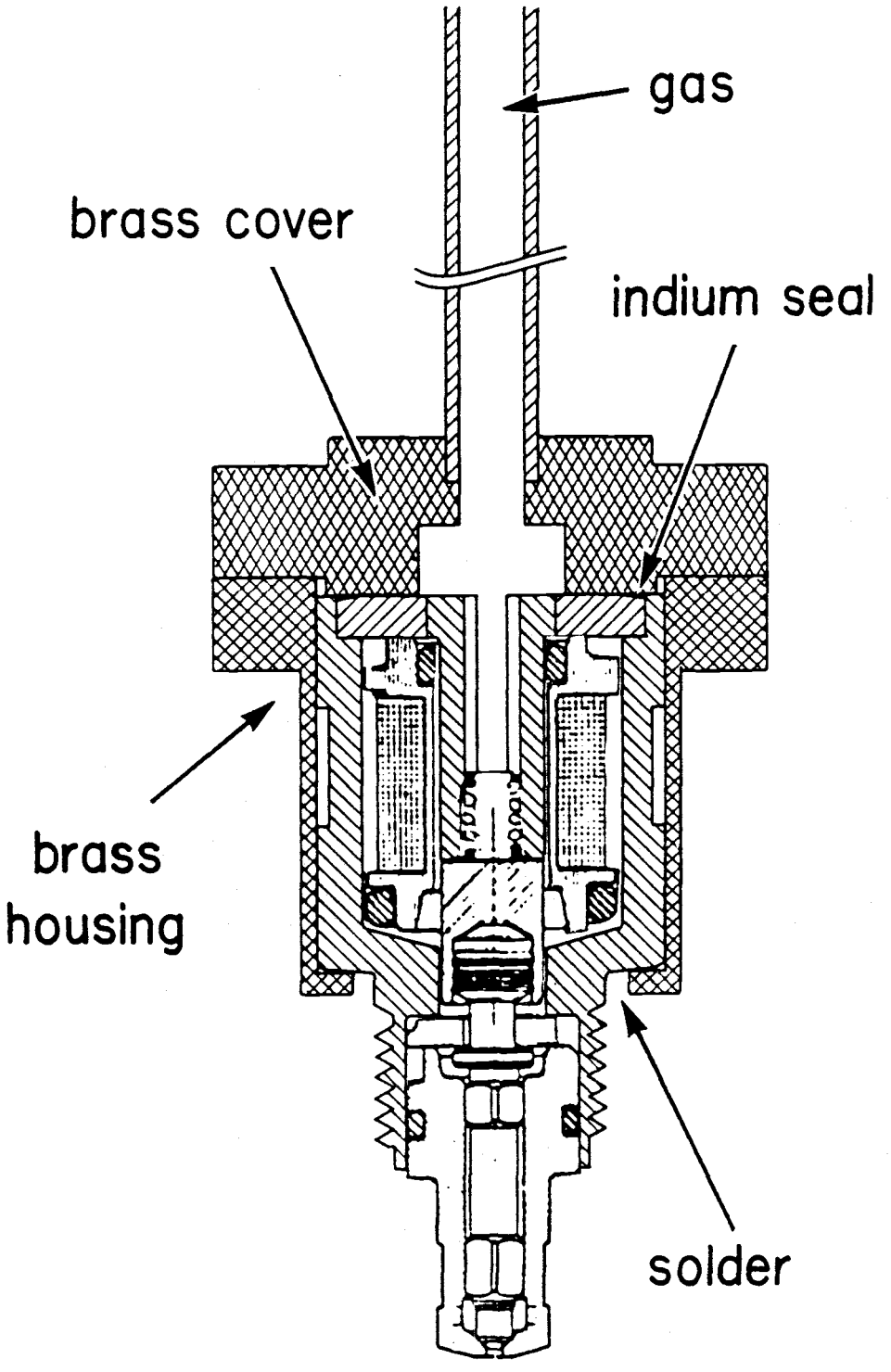

Figure 3.5 Pulsed valve modified for cooled, high pressure operation. Final modification to the pulsed valve showing the brass housing and the indium and solder seals. Not shown are the electrical connections to the solenoid which lead through the gas feed tube.

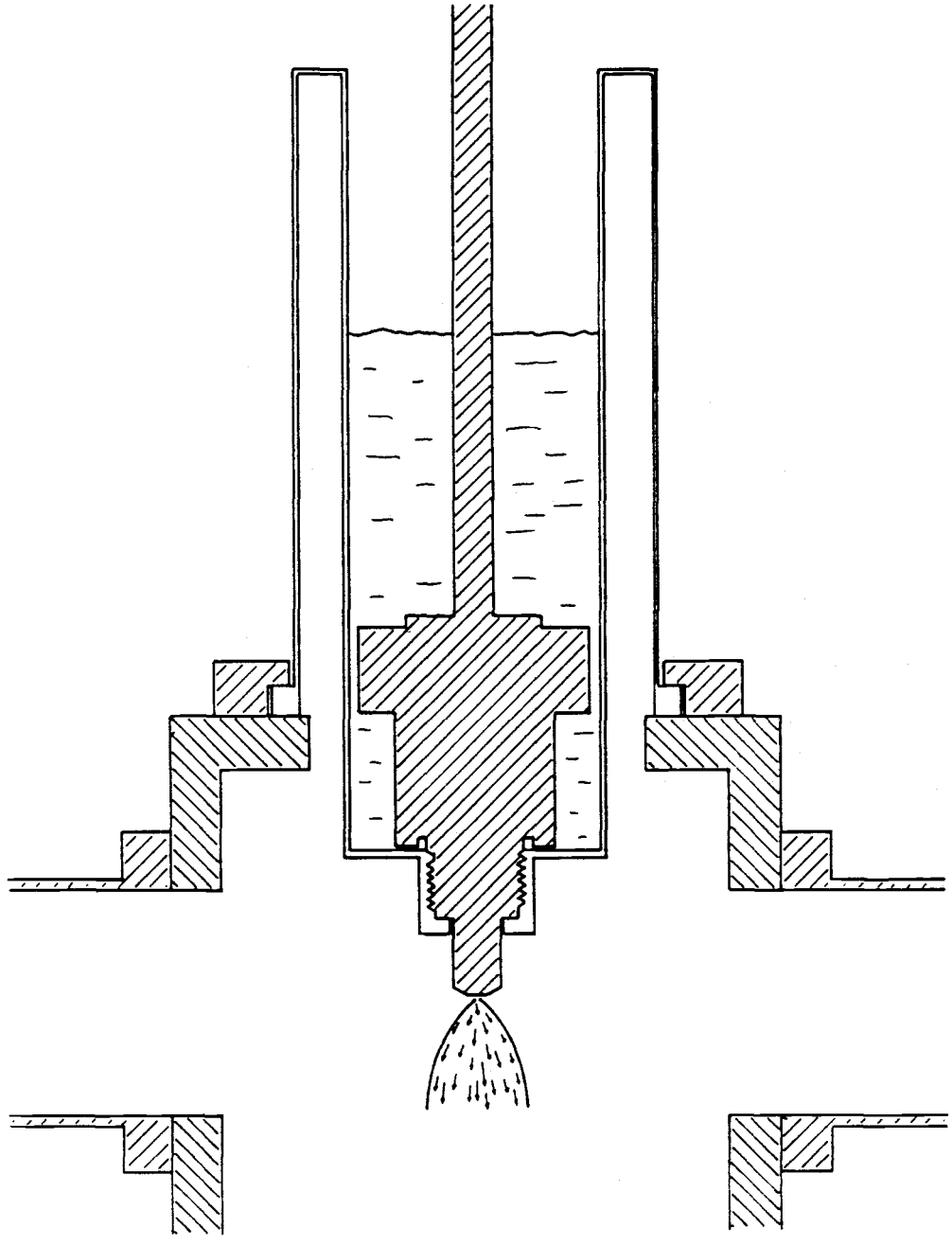

Figure 3.6 Cutaway drawing of dewar assembly and sample cell block. The chamber is evacuated and windows are affixed to the ends of the extension tubes. The laser beams propagate horizontally and intersect with the free jet zone.

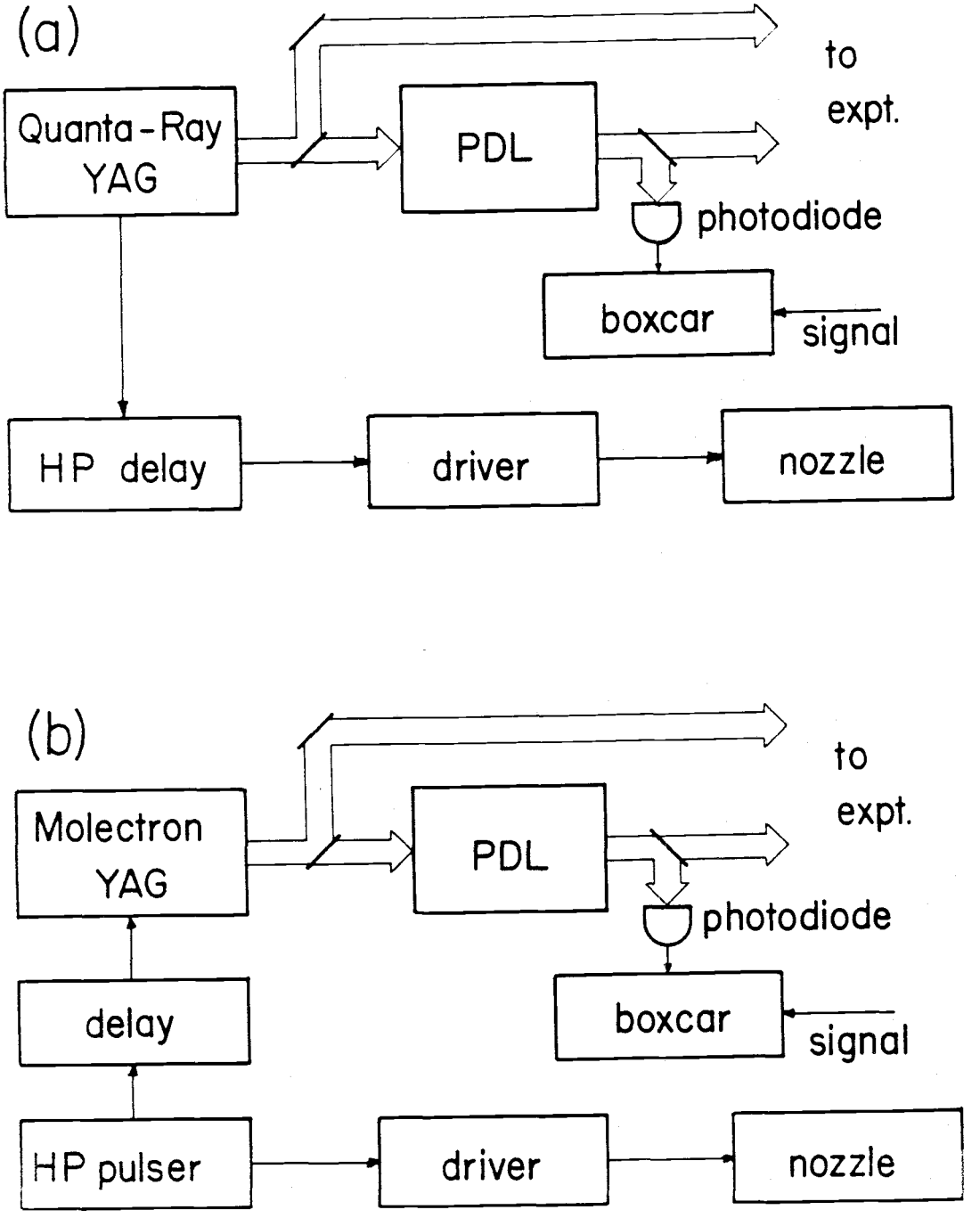

Figure 3.7 Timing diagrams for the CARS experiments. (a) Primary timing pulse is derived from Quanta-Ray YAG. (b) HP pulse generator provides 10 Hz pulse to trigger the nozzle driver and the Molectron YAG.

diameters.

An additional timing loop was necessary to effect a temporal overlap between the detected CARS signal and the gated integrator. While it would have been convenient to use the master oscillator output of the YAG to control the whole experiment it was found that the temporal jitter between the YAG pulse and the boxcar gate (±5 ns) was unacceptably large. The solution was to trigger the boxcar on a stray reflection of the output pulse of the dye laser and delay the signal from the PMT through a extra length of coaxial transmission line (9.25 m). This results in a signal loss of about 1.6 dB and a delay of about 47 ns. This delay is necessary to overcome the nominal 25 ns trigger discriminator delay in the SRS boxcar. By triggering in this fashion the gate is correlated precisely with the output of the dye laser and, since the dye laser pulse has the shortest width, the temporal jitter between the resulting CARS signal and the gate of the boxcar is less than 1 ns. As a consequence, the width of the gate can be adjusted to precisely overlap the width of the CARS signal (~8 ns), and maximize the signal to noise ratio.

The timing of the CARS experiment using the Molectron YAG had a different arrangement. The Molectron provides a "lamp sync" output with a pulse ~200 μs before the laser pulse. Since the pulsed nozzle requires ~500 μs to mechanically turn on after it receives an electrical pulse, the YAG cannot be used as the master oscillator. The alternative, depicted in Figure 3.7b, uses the internal timing circuit in the pulse generator to provide a 10 Hz pulse to the nozzle driver and at the same time to a variable delay YAG trigger. This latter delay can then be adjusted to achieve the required timing of YAG and

nozzle pulse. The triggering of the boxcar was identical to that described for the previous setup.

Sample CO_2 was from a commercial cylinder and passed through a Matheson 450 gas purifier with a type 451 cartridge. Mixtures of CO_2 and helium were made up to 350 psig by evacuating a cylinder and adding the required pressure of CO_2 using a Validyne diaphragm pressure gauge, then filling with commercial He to the final pressure as indicated on the regulator. Sample mixtures were allowed to mix for a minimum of 24 hours before use. The highest pressure used in this work was 250 psig.

RESULTS AND DISCUSSION

The first evidence of cluster formation in CO_2 was found in a jet spectrum of the $2\nu_2$ band of a 10% mix in argon. As soon as it was clear that clusters were being formed, helium was substituted as the carrier gas. Koenig[11] and coworkers have demonstrated that argon readily forms clusters with ethylene under the conditions of a supersonic jet. Helium, on the other hand, shows little tendency to cluster. For this reason it was chosen as the expansion medium. Two consequences of this decision are that helium has a negligible nonresonant signal versus the significant nonresonant susceptibility of argon and that helium is much less efficient in cooling in the free jet expansion. Our experimental evidence quickly illustrated this latter fact. CO_2 clusters were first observed in a 10% CO_2 in argon mixture with a stagnation pressure of 4.4 atm. Under very similar conditions (5.3 atm stagnation pressure) a 10% CO_2 in helium sample showed no evidence of cluster formation. Considerably more extreme

conditions were required to produce detectable concentrations of clusters in a CO_2:He mixture. A 20% CO_2 in helium mixture at a stagnation pressure of 10 atm produced concentrations of clusters similar to those previously observed in argon.

The $2\nu_2$ Q branch of CO_2 has a relative differential Raman cross section of 1.2 compared to that for ν_1 of 0.7.[58] For the CARS experiment the squared ratio of these cross sections would indicate that the ν_1 peak would be approximately one third as intense as the $2\nu_2$ peak. When the ν_1 region was investigated, indeed the cluster signals were somewhat lower but there were more peaks attributable to clusters and they were more completely resolved than in the $2\nu_2$ region.

Figure 3.8 of the ν_1 region illustrates the effect of cooling upon cluster formation. The top trace (a) shows the spectrum of a 5% CO_2 sample where the equilibrium temperature prior to expansion was 258 K. Note that the signal is displayed as the square root of the CARS intensity to facilitate visual comparison of relative species concentrations. Figure 3.8b depicts a similar spectrum with no cooling of the nozzle. Along with the monomer Q branch at 1285.5 cm^{-1}, four other features are discernible at 1275.3, 1278.7, 1279.8 and 1281.3 cm^{-1}. None of these features is present in static scans at room temperature or in jet expansions at lower driving pressures. The calculated translational temperatures at our sampling points range from 10 to 50 K, conditions such that no helium adducts are expected. Figure 3.8 shows that the 1275.3 and 1278.7 cm^{-1} peaks are enhanced at lower nozzle temperatures while Figure 3.9 displays similar variations of relative intensities with changes in CO_2 concentration

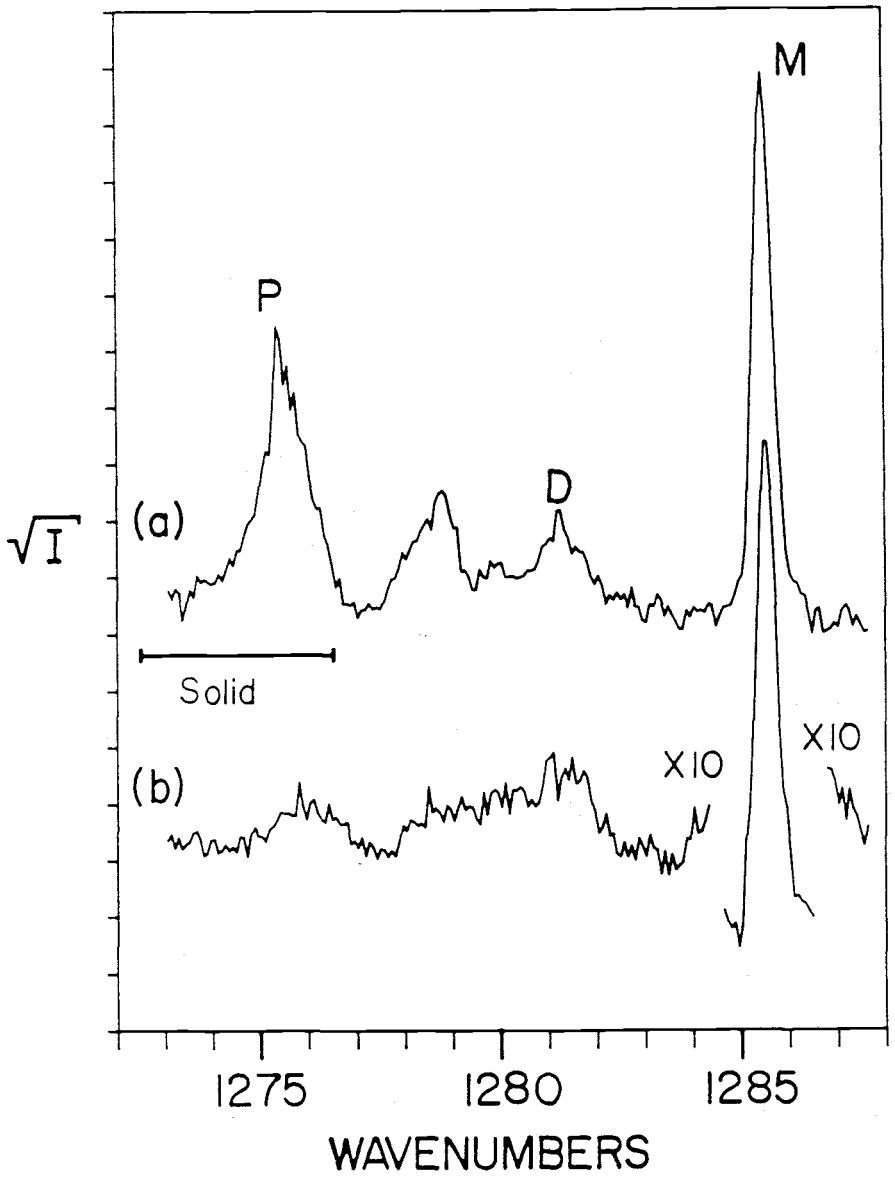

Figure 3.8 CARS spectra of CO_2/He expansions: the ν_1 region. The square root of the CARS signal is displayed to facilitate visual comparison of relative species concentrations. The labels P and D denote bands assigned as polymer and dimer respectively. (a) $\%CO_2$ = 5, X/D = 1.7, T_0 = 258 K, P_0 = 12.2 atm. (b) $\%CO_2$ = 5, X/D = 1.7, T_0 = 295 K, P_0 = 9.8 atm.

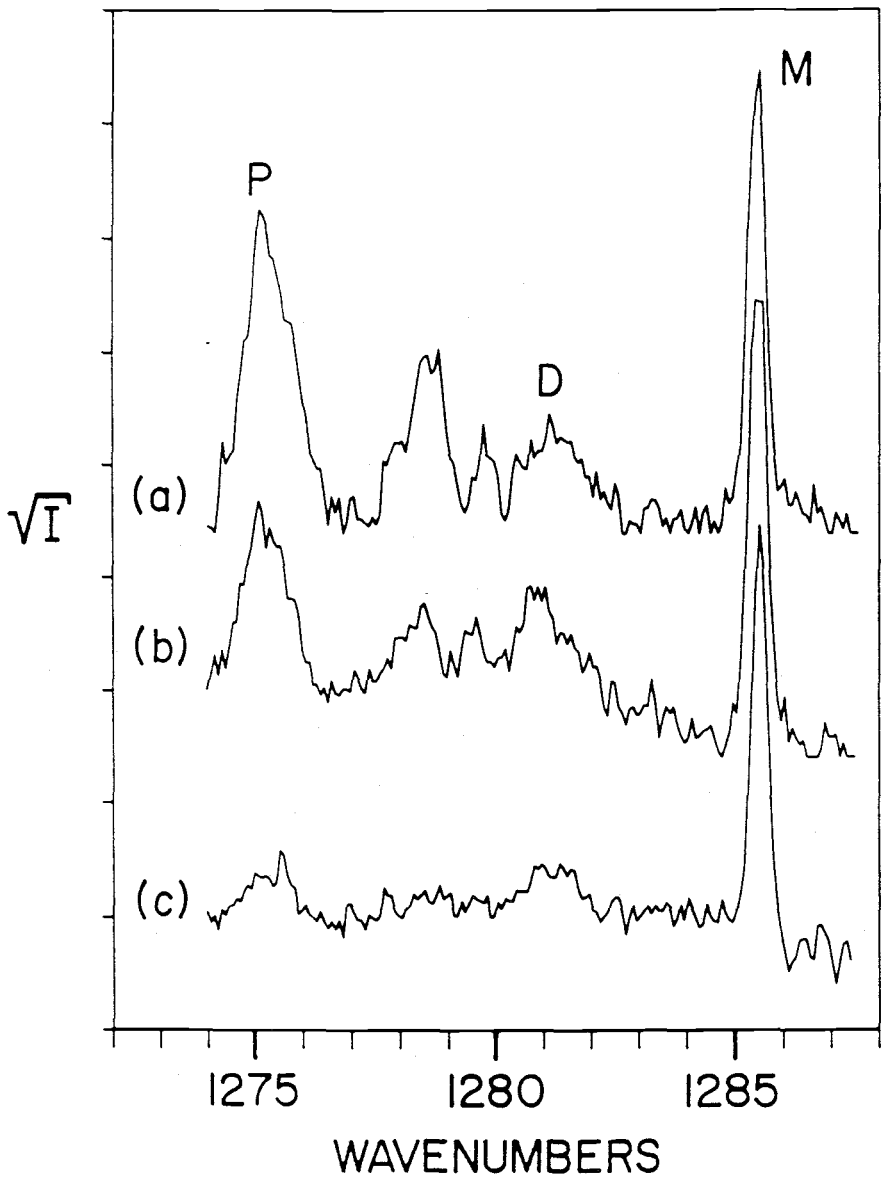

Figure 3.9 The effect of concentration and pressure on the distribution of cluster sizes.
(a) $\%CO_2$ = 5, X/D = 2.1, T_0 = 208 K, P_0 = 12 atm.
(b) $\%CO_2$ = 2, X/D = 2.0, T_0 = 208 K, P_0 = 14.6 atm.
(c) $\%CO_2$ = 1, X/D = 1.8, T_0 = 208 K, P_0 = 18 atm.

and driving pressure. These and other spectra indicate that at least four, and probably more, aggregate species contribute to these spectra, with colder, more condensing expansions favoring bands with greatest red-shift. It may be noted in Figure 3.8 that the 1275.3 cm^{-1} feature labelled P falls in the range reported for the Raman spectrum of solid CO_2.[59] This band shows a red-shift (0.6 cm^{-1}) as the fraction of polymer increases, an effect also noted by Gough et al.[55] in their IR predissociation studies of the $2\nu_2+\nu_3$ combination band and ascribed to increasing mean size of the clusters. No comparable shift was obvious for the other aggregate features although band overlap made precise frequency measurements difficult.

Assuming that the Raman cross section is unaffected by aggregation, we infer from the peak areas of Figure 3.8a that about 20% of the CO_2 is in the form of complexes. Only small cluster sizes would be expected under these conditions and the relative intensity variation and frequency position of the 1281.3 cm^{-1} band support its assignment to the dimeric (D) species. A sequential progression of the cluster bands from monomer to solid frequency values is reasonable and both continuous[55,56] and stepwise[12,13,60] shifts with aggregation have been observed for other small complexes. A search was made for features between the monomer line at 1285.5 cm^{-1} and the band at 1281.3 cm^{-1} using various milder expansion conditions. The absence of any shoulders or new structure to the blue when the 1281.3 cm^{-1} line was still apparent is taken as compelling evidence that the latter characterizes the dimer frequency. Less certain is the assignment of the other clearly resolved band at 1278.7 cm^{-1} which we speculate may be due to trimer. The data provide no basis for this characterization

but it may be noted that this choice produces a pattern of frequency shifts very similar to that observed for HCN complexes, a case in which the assignment of dimer and trimer bands was aided by spectra obtained for equilibrium samples at room temperature.[12,13]

Comparison with Infrared Data

Infrared spectra of the ν_1, $2\nu_2$ region have been reported by Mannik et al.[46] and by Kopec.[54] Both groups obtained similar dimer spectra with unresolved PQR bands. Mannik gave no absolute wavenumber values for these features but, for ν_1, Kopec reports PQR maxima at 1280.5, 1284.7 and 1289.2 cm^{-1}. Figure 3.10a is a reproduction of Kopec's spectrum (Fig. 4.7 of Ref. 54) for comparison with our CARS results for this region. The CARS bands are referenced to the known monomer frequency and have an uncertainty of 0.2 cm^{-1}. The accuracy of the IR measurements was not given by Kopec although the resolution was 0.375 cm^{-1}. Since the IR spectra were obtained on an FTIR instrument, the absolute frequency uncertainty should be much smaller. An uncertainty less than 0.2 cm^{-1} is suggested by calibration with the R branch fine structure of $^{12}C^{16}O^{18}O$ which appears in Figure 3.10a.

Given these frequency uncertainties it is certain that the 1284.7 cm^{-1} IR mode is distinct from the 1281.3 cm^{-1} Raman feature that we attribute to dimer. No indication of this Raman active mode is apparent in the IR spectrum. In addition, there appears to be no Raman feature corresponding to the 1284.7 cm^{-1} IR Q branch. We have taken high resolution (0.05 cm^{-1}) scans of the monomer under conditions which give varying degrees of clustering and this region is clear to

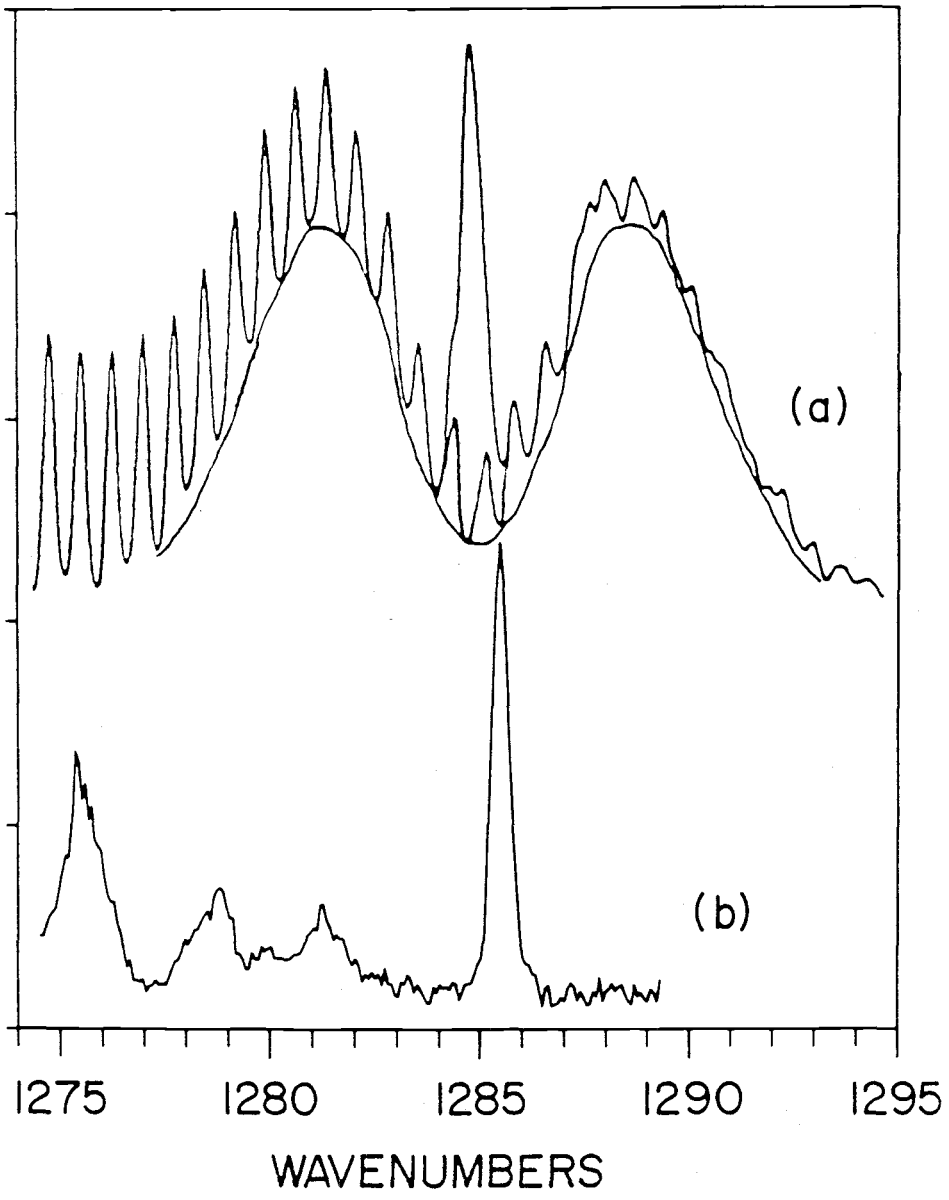

Figure 3.10 Comparison of CARS and infrared data for $(CO_2)_2$. Spectrum (b) (same as Fig. 3.8a) is compared with a reproduction of the infrared spectrum (a) reported by Kopec.[54] Kopec has drawn a smooth line under the rotational R branch peaks of $^{12}C^{16}O^{18}O$ to emphasize the dimer P-R contours and has interpolated the monomer structure in the Q branch region of the dimer.

within 0.2 cm^{-1} of the exceptionally narrow monomer line (FWHM = 0.09 cm^{-1}). We estimate that the Raman cross section of the 1284.7 cm^{-1} mode must be less than 25% of the 1281.3 cm^{-1} band or it would have been detected. Thus the rule of mutual exclusion seems to apply to the CO_2 dimer.

Structural Implications for the Dimer

Figure 3.11 illustrates the normal modes for the two forms of the CO_2 dimer. The offset parallel structure has C_{2h} symmetry with in-phase (A_g) and out-of-phase (B_u) combinations of the two CO_2 symmetric stretches. For this centrosymmetric structure the A_g mode will be Raman active while the B_u vibration will appear only in the IR spectrum. For the T structure, the two symmetric stretches will be active in both IR and Raman spectra. Since the two CO_2 units are perpendicular for this geometry, the G matrix elements coupling these two modes are identically zero and very little mixing of the two isolated symmetric stretches will occur. The consequence of this should be that both modes will have comparable intensities in the Raman spectrum since the polarizability derivatives will be essentially those of the two monomer units. Clearly, the observations do not fit this expectation and are much more consistent with the nonpolar C_{2h} configuration.

Our conclusion thus is that the most stable configuration of the dimer contains an inversion center and hence is nonpolar. However our results do not exclude the possibility of a small amount of a polar form whose presence could account for the electric deflection results. The CARS spectra do show a weak but reproducible Raman feature at

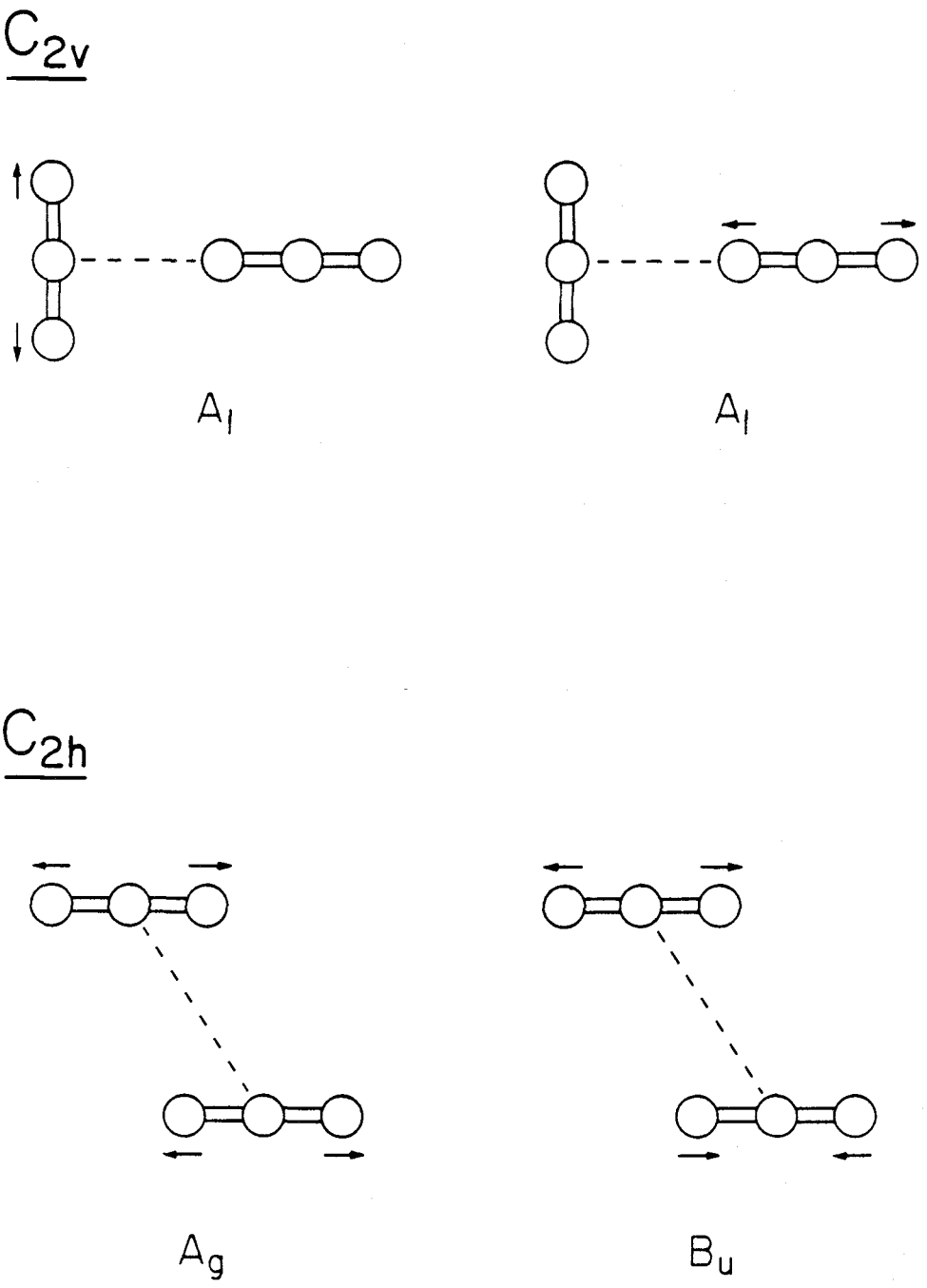

Figure 3.11 Normal modes for the two proposed structures of the CO_2 dimer in the ν_1 region. Because of orthogonality the two modes of the C_{2v} structure are almost completely uncoupled and would both be infrared and Raman active, The C_{2h} structure exhibits one Raman active mode (A_g) and one infrared active mode (B_u).

1279.8 cm^{-1} which could arise from such a species. Such an assignment is purely speculative however and additional data will be needed to test this possibility. Higher resolution spectra could be useful in this regard. Inspired by the rotational fine structure observed by Miller and Watts[56] in the $\nu_1+\nu_3$ combination band of the CO_2 dimer, we have recorded CARS spectra using similar 1 and 2% mixtures of CO_2 in He at high driving pressures. Figure 3.12 shows the average of 5 spectra taken with the high resolution CARS apparatus of the dimer band. There is clear evidence that the band is inhomogeneously broadened, however no Q branch rotational structure was apparent in the dimer region at our resolution limit of 0.05 cm^{-1}.

Improvements in the resolution and S/N limits of these experiments are possible and these may permit some useful measure of the Q branch detail in the 1 cm^{-1} wide band of CO_2 dimer. Even with the present detection capability, the results presented here demonstrate the value of the CARS technique in probing van der Waals complexes. Further refinements will allow the study of many interesting aggregates of small molecules formed in free jets. In addition, the precise spatial resolution and the ability to probe early stages of the expansion suggest that nonlinear Raman methods should prove valuable in the study of aggregation processes.

The limits in resolution imposed by the lasers used in this CARS study can be overcome and both CARS and other coherent Raman techniques can be applied using very narrow linewidth lasers. The design and construction of a very high resolution inverse Raman spectrometer and its preliminary application to the spectroscopy of CO_2 and $(CO_2)_2$ is the subject of the last chapter.

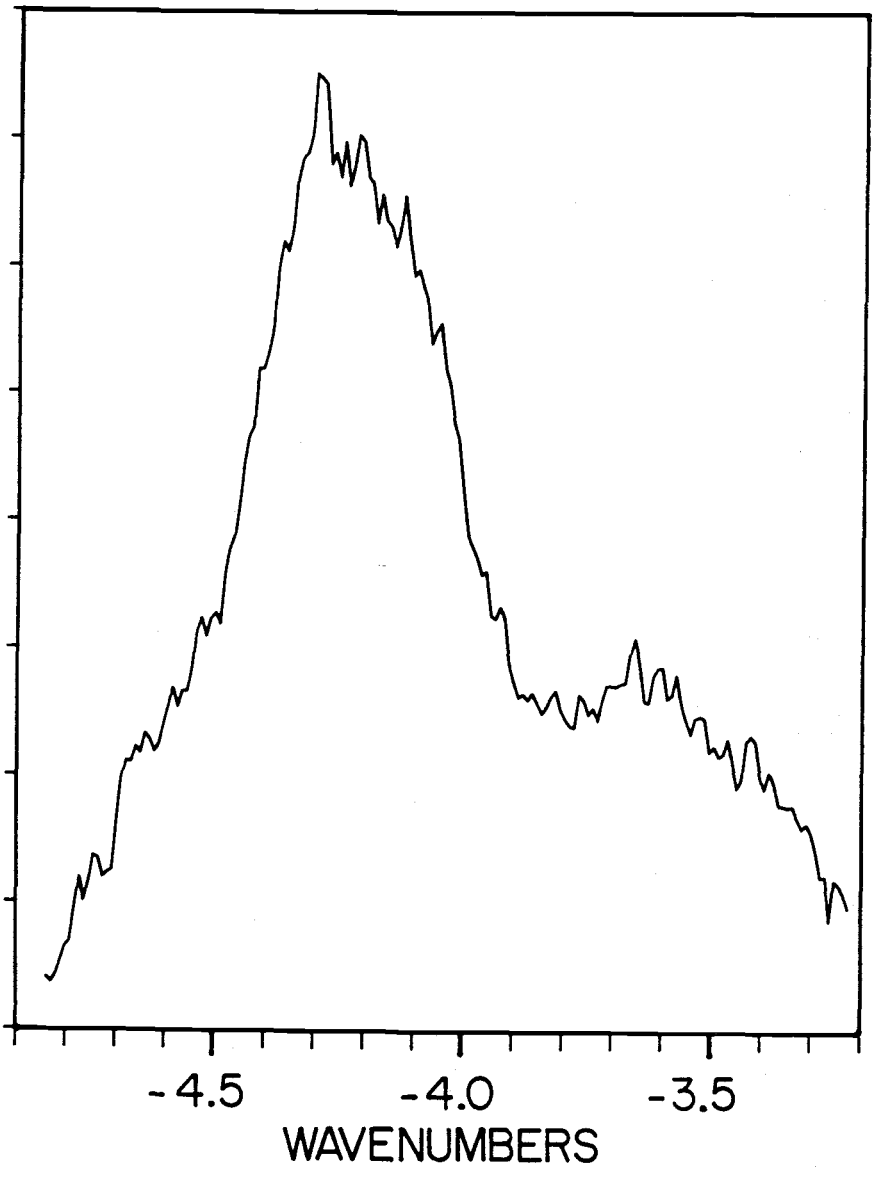

Figure 3.12 Average of 5 "high resolution" CARS spectra of the ν_1 dimer band in a supersonic jet. Resolution = 0.05 cm^{-1}, 2% CO_2 in He, P_0 = 14 atm, T_0 = 208 K.

CHAPTER 4 -- HIGH RESOLUTION INVERSE RAMAN STUDIES

INTRODUCTION

The literature of spectroscopy chronicles dramatic improvements in resolution over the last few decades. Most of the improvement can be credited to the development of tunable laser sources where the limit to resolution is the linewidth of the source rather than the dispersive ability of a monochromator. Coherent Raman techniques have developed to take advantage of the improvements in narrow laser sources. In particular, the actively stabilized, tunable dye laser has spurred the development of high resolution capabilities. In this chapter we will discuss the design of a high resolution inverse Raman spectrometer and its application to the CO_2 problem discussed in the previous chapter.

Spectroscopists have endeavored to improve resolution for a number of reasons. Improved resolution almost certainly yields improved accuracy in the measurement of the energy of a given transition. This improvement gives better spectroscopic constants and the structural and thermodynamic values which are derived from the spectroscopic data. In many cases the improvement in resolution has enabled the accurate assignment of transitions which were formerly characterized by broad unresolved bands. In other cases, the improved resolution has enabled the observation of effects which were formerly unobserved and unknown or only predicted. An example of this is the optical Stark effect where a shift in the molecular vibrational and rotational frequency is induced by a intense, nonresonant optical field.[7] High resolution also enables the precise determination of linewidths which yields information about lifetimes. It also reveals some subtleties of

linewidth which had not previously been seen.[61]

CHOICE OF LASERS

In determining the best lasers to use for a specific experimental setup many factors must be considered. The choices for an inverse Raman spectrometer were limited by the available narrow linewidth lasers. In this experiment one laser, the probe laser, operates in a continuous (cw) mode while the other laser, the pump laser, is a high power pulsed laser. Our first consideration will be the choice of the probe laser. Gas lasers such as a helium-neon and ion lasers can be equipped to provide a stable single-frequency, single-mode source for a fixed frequency probe. Single-mode dye lasers similar to the one which will be described in the next section have also been used as probe lasers. They have the added feature of tunablity, allowing more flexibility in the design of an experiment, however, dye lasers have a much higher inherent noise than gas lasers due primarily to the fluctuations in the dye jet stream. Considering the need for high power and low noise coupled with economy and ease of operation, the ion laser is a clear choice. Finally the choice between the argon ion and the krypton ion laser is essentially a choice of the Raman shift regions which would be available with each system. Table 4.1 shows the Raman shifts accessible using a ring dye laser and various probe lasers. Based upon this table the argon ion laser is the best choice.

Ion lasers have been used with considerable success in configurations which favor a single cavity mode. The approach generally taken is to start with an ion laser tube mounted in a temperature-compensated resonator with a frequency tuning element for

Table 4.1 Raman shift regions (cm^{-1}) accessible with ring dye laser and various probe lasers. YAG laser shifts would include those Raman shifts accessible with a CARS configuration. *DCM data taken from Exciton catalog, others from measured gain profiles.

		Tunable Laser								
Dye:		R110			R590			DCM*		
		Min	Peak	Max	Min	Peak	Max	Min	Peak	Max
Fixed Laser										
(Å)→		5450	5700	5850	5715	5800	6211	6100	6400	7000
↓										
4765	Ar	2638	3442	3892	3489	3745	4886	4593	5361	6701
4880	Ar	2143	2948	3398	2994	3250	4391	4098	4867	6206
4965	Ar	1792	2597	3047	2643	2900	4041	3748	4516	5855
5017	Ar	1584	2388	2838	2434	2691	3832	3539	4307	5647
5145	Ar	1088	1892	2342	1939	2195	3336	3043	3811	5151
5287	Ar	566	1370	1820	1417	1673	2814	2521	3289	4629
5309	Kr	487	1292	1742	1338	1595	2735	2442	3211	4550
5320	YAG	448	1253	1703	1299	1556	2697	2404	3172	4511
5682	Kr	-749	56	505	102	358	1499	1206	1974	3314
6471	Kr	-2895	-2090	-1640	-2044	-1788	-647	-940	-171	1168

the high reflector. A small prism, tuned with the vertical adjustment of the rear reflector has the effect of limiting the laser to one lasing region. At the high temperatures in the plasma the Doppler broadened gain profile of the argon laser is greater than 5000 MHz.[62] The spacing between longitudinal modes in a standing wave cavity is $\Delta f = c/2L$ where Δf is the frequency difference between two adjacent modes, c is the speed of light and L is the effective cavity length. We note that the effective cavity length is slightly longer than the measured length due to the elements (windows and étalon) which have a higher index of refraction than air.

In our laboratory an argon ion laser was chosen (Spectra-Physics 165-08) with a temperature stabilized solid étalon (Spectra-Physics 583). In this laser L = 1.05 m and Δf = 143 MHz. It is clear that the laser will operate on quite a number of longitudinal modes simultaneously. The manual suggests that for transitions with high gain, this could result in more than 20 individual frequencies. To overcome this tendency to operate multimode an étalon with a free spectral range (FSR) of about 10,000 MHz is placed within the cavity. Figure 4.1 illustrates the combination of laser gain profile, allowed cavity modes and the étalon loss curve. By using a low finesse étalon just enough loss can be incorporated into the cavity to cause one cavity mode to dominate. Spectra-Physics indicates that the short term (<1 s) frequency stability with this configuration is 8 MHz and that the long term (~10 h) stability is 80 MHz. In laboratories where this is insufficient, active stabilization has achieved stability better than ± 1 MHz.[63] Since the pulsed laser in this experiment has a transform broadened linewidth of ~60 MHz, further effort to stabilize

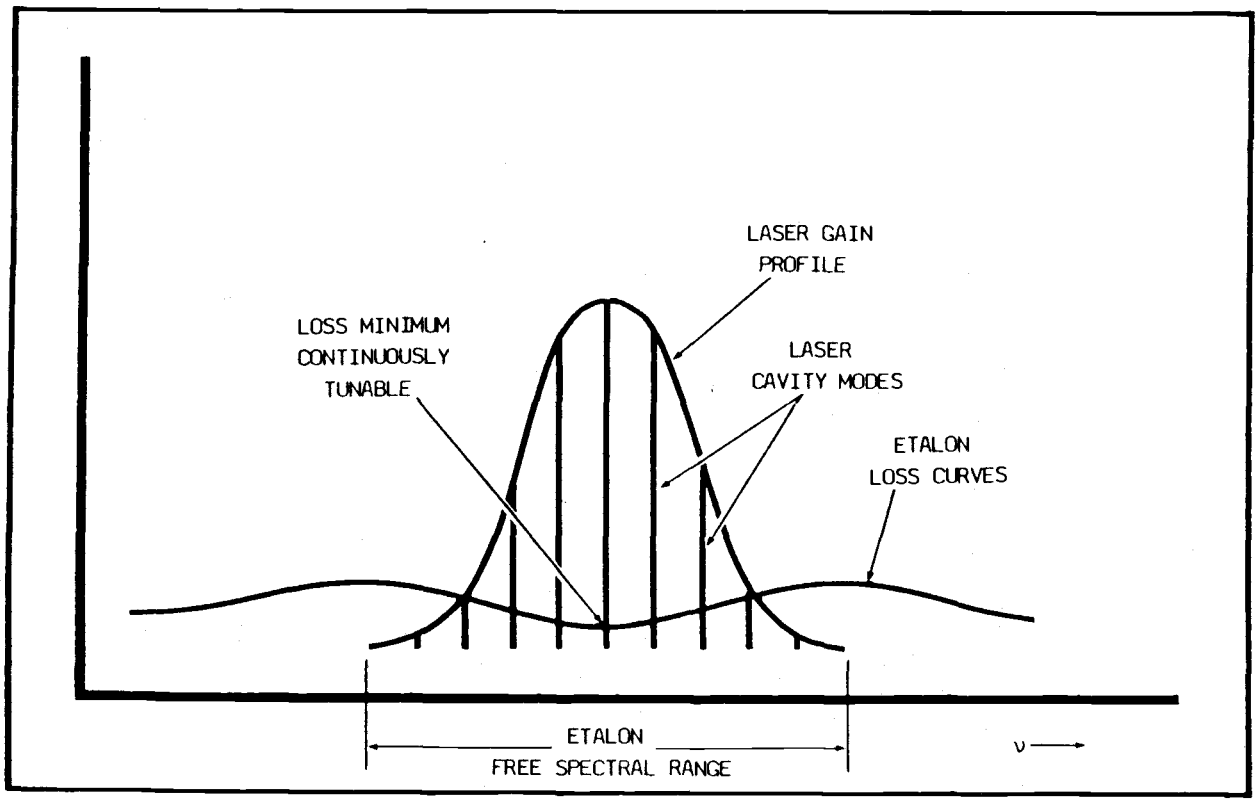

Figure 4.1 Argon ion laser gain profile showing cavity modes and étalon modes. (from Ref. 62)

the argon ion laser was deemed unnecessary.

It is even more difficult to achieve stable single frequency pulsed operation. Littman[64] recently reported on a novel pulsed dye laser oscillator which has near TEM_{00} mode, a linewidth of ~150 MHz and an efficiency of 3%. The design features a very short cavity which allows at least 10 round trips within the duration of one pulse. This feature is credited with reducing amplified spontaneous emission to <0.01%. During scanning, the cavity length changes by just the amount necessary to keep the number of wavelengths constant and this has enabled scans of up to 25 cm^{-1} without mode hops. While this design appears to have promise it requires considerable additional equipment to calibrate and stabilize it as well as the time and effort in building and integrating it into a working system. No commercial system based upon this design has yet appeared.

Several groups[65,66] have demonstrated workable pulsed systems based upon a cw tunable dye laser oscillator and a series of pulsed amplifier cells. First we will consider the desirable features of the tunable cw dye laser. The primary requirements are for a unit with high stability in a single mode, the ability to tune precisely within a specified range with no mode hops and the power necessary to saturate the first stage of an amplifier. A commercially available unit (Coherent 699-29) has many features which recommend it for this purpose. They are:

1. Traveling wave, ring cavity which optimizes power and improves stability.
2. Actively stabilized cavity locked to a temperature stabilized reference cavity. Active elements include a thick étalon, a thin

étalon, a high reflector fold mirror and a tilting Brewster plate.

3. Integral wavemeter which features 0.002 cm^{-1} accuracy.
4. Computer control of scanning which, in conjunction with the wavemeter, permits highly accurate scans of many wavenumbers.

A schematic of the cavity of the scanning ring dye laser is shown in Figure 4.2. Since this system is relatively complex, we consider here in some detail the functional operation of this device. The primary excitation source for the dye laser is an argon ion laser with an output of 5 watts all lines (Coherent INNOVA 90-5). This pump beam is brought to a focus within the dye jet with the pump mirror M_1. Four mirrors combine to form the cavity. M_6 is a high reflector located just behind the pump mirror. It images the fluorescent dye spot onto M_5, the upper fold mirror. M_3 is a piezoelectrically driven mirror which images the fluorescent dye spot onto the output coupler M_4. Other important elements in the cavity include the intracavity étalon assembly (ICA) which includes a piezoelectrically driven thick étalon (FSR = 10 GHz) and a galvo driven thin étalon with a FSR of 225 GHz. Coarse scanning is accomplished with a 3-plate birefringent filter[67] which is mounted at Brewster's angle. Scans of 30 GHz can be accomplished by tilting a "scanning Brewster plate". The effect of this is to slightly alter the length of the cavity, the two étalons are scanned concurrently and, with proper electrical adjustment, the laser changes frequency smoothly with no mode hops.

The "optical diode" completes the list of critical components. This device consists of a section of special optical glass which is placed in a magnetic field. Polarized light which passes through this glass experiences the Faraday effect where the axis of polarization is

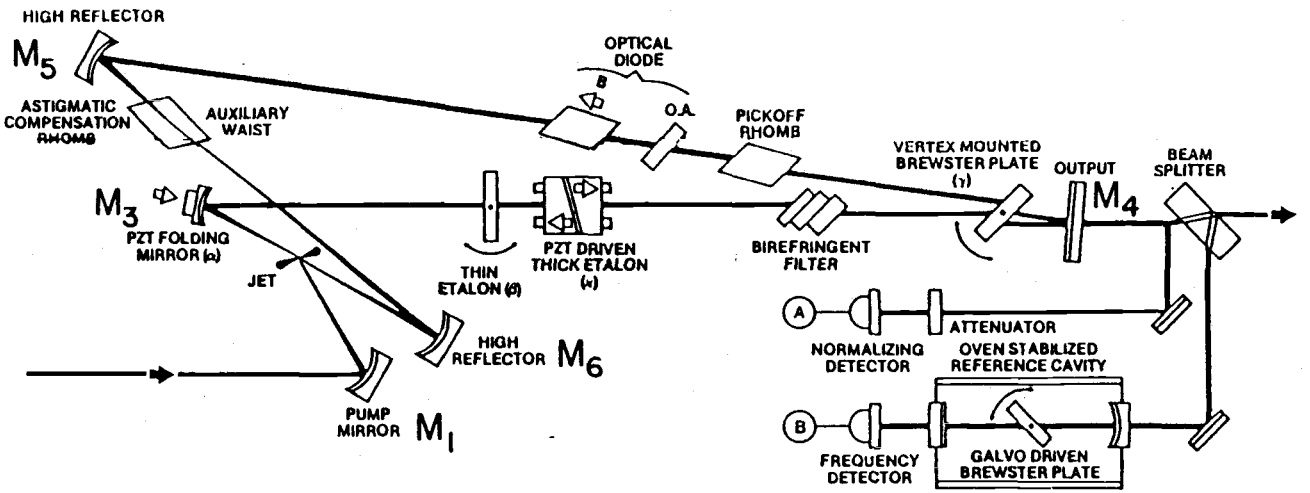

Figure 4.2 Schematic of the Coherent 699-29 ring dye laser. (from Ref. 68)

rotated slightly. This light then passes through a thin quartz element which also rotates the light by the same amount. The combined effect of these two elements is different depending upon the direction of the incident light. In one direction, the forward direction, the quartz plate imparts a slight rotation of the vertically polarized light circulating in the cavity then the Faraday rotator rotates the light in the opposite direction for a net rotation of 0. In the reverse direction the Faraday rotator imparts a rotation in the same direction as the quartz plate resulting in a net rotation of polarization. The slight loss of power on the various Brewster elements within the cavity is sufficient to suppress this direction of oscillation and ensure that the laser operates in the forward direction only.

Without active stabilization the laser has a linewidth of about 20 MHz which is due primarily to mechanical and acoustic vibrations causing a change in the length of the cavity. In the active mode the output of the laser is sent to a temperature stabilized Fabry-Perot cavity where an error signal is derived by comparing the fringe information with a power reference. This error is used to drive both the scanning Brewster plate and the piezoelectrically driven fold mirror M_3 (tweeter). The frequency response of the Brewster plate is on the order of 10 Hz and that of the tweeter is 10 kHz. With this active stabilization the laser has a linewidth of ~1 MHz.

From the standpoint of the spectroscopist, the most important feature of this laser is the built in wavemeter which serves two critical functions. First it provides an absolute frequency reference and with the aid of the computer automatically sets the laser to a precise frequency. Second, the wavemeter is the heart of the scanning

function, measuring the wavelength at the start of each 10 GHz scan and ensuring that a total scan of many wavenumbers can be made by accurately overlapping contiguous 10 GHz segments. Without the wavemeter, this laser can be scanned a maximum of 30 GHz (1 cm^{-1}) before it has to be reset by hand.

The wavemeter is shown in schematic form in Figure 4.3. Two beams are split off of the output of the laser and directed up into the wavemeter housing mounted just above the output coupler. The beams are further split, one impinges upon a power sensor, while two beams are directed into two rods of Z cut quartz 70 and 74 mm in length. This optical activity monochromator (OAM) measures the difference in the degree of rotation between the two linearly polarized beams, a quantity which is wavelength dependent. The difference in polarization rotation between the two beams is measured with a spinning disk of polaroid material and two sensors.

The rotation of polarization through just one of the crystals ranges from 1000 to 3500° but the difference in the rotation between the two beams varies less than 180° over the entire scan range of the laser. This allows a coarse wavelength and an OAM order to be determined. Once a particular 180° order has been established, the determination of absolute rotation allows the frequency to be established to an accuracy of ± 1 cm^{-1}. This is sufficient to provide a means of determining a particular vernier étalon (VET) repeat range for a more precise frequency measurement.

The VET consists of two étalons spaced by two C shaped pieces of Zerodur glass of slightly different length, enclosed within an evacuated, temperature-stabilized housing. The free spectral range of

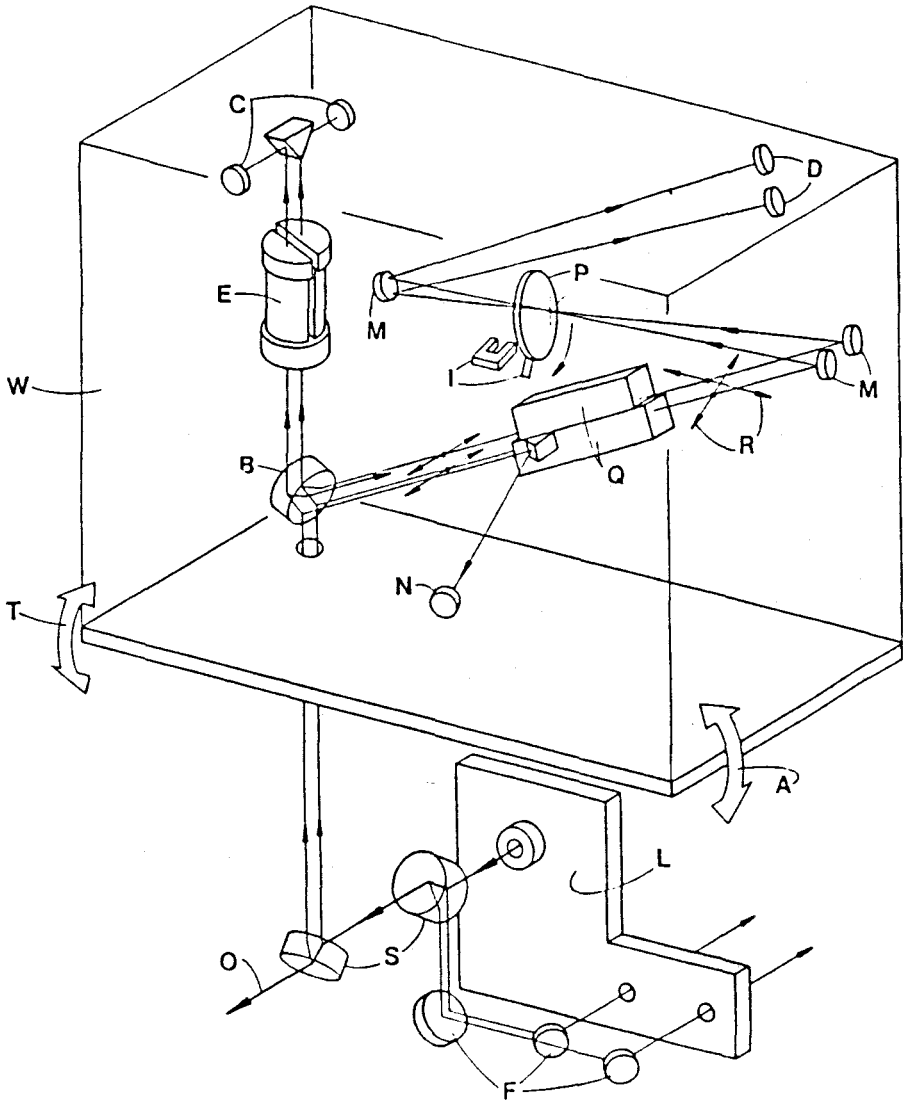

Figure 4.3 Schematic of dye laser wavemeter (from Ref. 68)

A. Wavemeter tilt adjust, about an axis axial to the laser
B. Brewster-angle polarizing beamsplitter (13% each beam)
C. Detectors for channels 1, 2 of the VET
D. Detectors for channels 1, 2 of the OAM
E. Vernier etalon assembly
F. Fold mirrors delivering beams to the frequency servo
I. Interrupter & flag locating the orientation of the polarizer
L. Output end plate of the CR-699-21 dye laser
M. Fold mirrors delivering beams to OAM detectors
N. Detector for intensity normalization in the wavemeter
O. Laser output beam
P. Spinning polarizer wheel
Q. Crystal Quartz bars (2 lengths) for OAM
R. Arrows indicating rotated polarization vectors
S. 45° incidence beamsplitters (2 places, 0.7% each beam)
T. Wavemeter tilt adjust, about an axis transverse to the laser
W. Wavemeter package, mounted on the tilt plate

the two étalons is 6.5 and 6.8 GHz. After approximately 23 free spectral ranges of the longer étalon, the relative positions of the two étalon peaks repeats, thus the VET repeat range is ~150 GHz. The computer "reads" the VET by scanning the laser about 15 GHz and measuring the frequency difference between the peaks of the two étalon transmission curves. This difference determines which étalon peak within the repeat range is being viewed. The final frequency determination is made by considering the position of the first étalon peak with respect to the beginning of the read scan. Thus a frequency measurement is a four step process: 1) determine OAM order, 2) determine coarse frequency from absolute rotation of OAM, 3) locate position of peak within the VET repeat range, and 4) measure position of VET peak relative to current laser setting and calculate frequency.

Needless to say, the operation of the wavemeter and the control of the scanning of the laser mandates the use of a computer. An Apple IIe microcomputer is integrated into the laser system with special interface and control electronics supplied by Coherent. Also supplied by Coherent is a BASIC program with associated assembly language subroutines to enable the microcomputer to control and calibrate the laser.

PULSED PUMP LASER

The choice of pump laser was limited to Nd:YAG, nitrogen and excimer lasers. Previous laboratory experience with YAG lasers in addition to the need for nearly single-mode operation strongly favored the choice of the doubled Nd:YAG as the pump laser. This choice also offers the flexibility of allowing the YAG to be used for CARS

experiments in addition to the inverse Raman experiment. Important specifications for this laser include the beam profile and the pulse width. The ideal beam profile for spectroscopy is a TEM_{00} beam which has Gaussian power distribution and an absence of "hot spots", small areas of the beam cross section which have much higher relative power. These hot spots are the primary cause of damage to expensive optics as well as the cause of inefficient pumping in a dye amplifier. Unfortunately a stable resonator design which favors the ideal Gaussian beam profile does not extract power efficiently from the solid Nd:YAG crystal which provides the gain medium for the laser. In most commercial systems the cavity design is an unstable resonator configuration which trades off beam quality for efficiency.

Power is coupled out of the oscillator using a diffraction scheme which produces a beam with a hole in the center of the cross section or as an alternative, by polarization coupling. Polarization coupling, the method used by the Molectron MY34-10 employed in our experiments, produces a beam with a more even cross-sectional power distribution. However, the most compelling reasons for favoring this laser are its 20 ns pulse width which yields a narrower Fourier transform limited linewidth in the amplified dye laser, and the availability of a single axial mode option (SAM). The design of the single axial mode option is important for high resolution work and bears some explanation.

The optical schematic of the Molectron MY34-10 is shown in Figure 4.4. Two elements, the SAM étalon and the unétalon comprise the optical part of the SAM while the electrical part, the Q switch trigger, comes from a photodiode monitoring the power circulating in the cavity. In its operation the unétalon is aligned normal to the

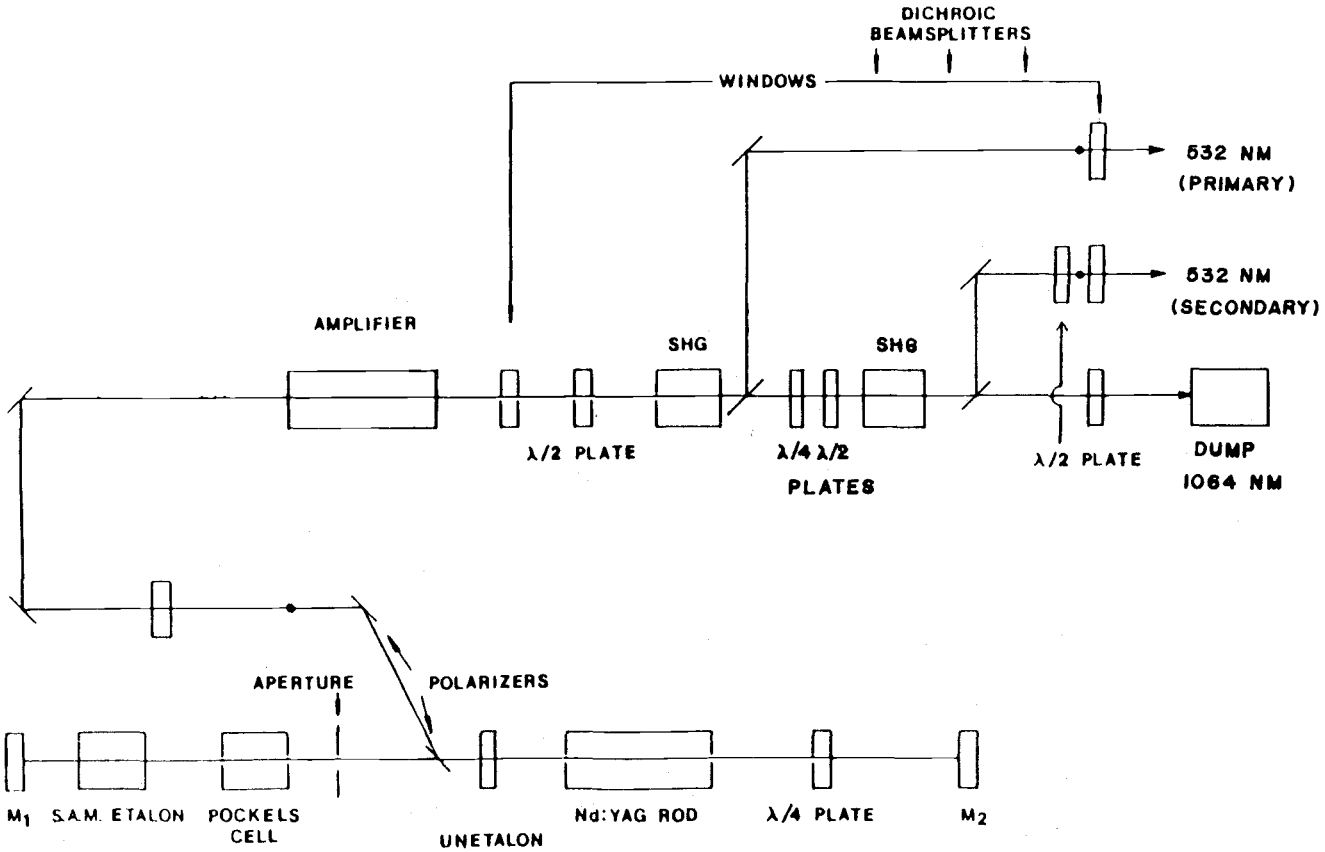

Figure 4.4 Optical schematic of Molectron MY34-10 Nd:YAG laser showing single axial mode option. (Adapted from Ref. 69)

lasing axis and provides a secondary or prelase cavity. The flashlamp power in the oscillator is adjusted below lasing threshold for the prelase cavity with the rear reflector blocked. The voltage to the KD^*P Pockels cell (Q switch) is adjusted to just sustain a low level of circulating power within the cavity. In order to sustain lasing the mode must be resonant in both the prelase and the main cavities. This constraint along with the selective loss induced by the SAM étalon highly favor a single resonant mode. With careful adjustment of the SAM étalon and the Q switch voltage the prelase pulse forms slowly enough after the flashlamps fire to establish a single mode which continues to build in energy. At a certain power threshold the photodiode triggers the Q switch and the remaining gain in the oscillator rod is quickly dumped into this already established, stable single mode.

For the CARS experiment, single mode operation enables high resolution spectroscopy when combined with a narrow linewidth pulse amplified dye laser. When used as a pump for a pulse amplification system, the single-mode character has a more subtle but equally compelling advantage. The radiation emitted from a multimode YAG laser consists of numerous cavity modes with a frequency spacing $\Delta f = c/2L$, where L is the effective cavity length. If two adjacent cavity modes predominate, the temporal profile of the output pulse will exhibit amplitude modulation or mode beating with a frequency equal to the mode spacing. When this pulse is used to pump an amplifier, the temporal profile of the pump modulates the output of the amplifier. The change in multimode behavior from one shot to the next, coupled with the fixed time delay between amplifier stages, causes a variable superposition of

the temporal profile of one amplifier stage upon the next. This fluctuating superposition results in a dramatic shot to shot variation in the overall amplifier gain. In addition it broadens the linewidth of the amplified pulse because the modulation causes sidebands. Thus, although there is a significant price paid in output power when running with the single mode option, this loss is overshadowed by the benefits of a smooth temporal profile.

PULSED DYE AMPLIFIER

There were many options for the design of a pulsed amplifier system. Drell and Chu[65] reported a setup using two transverse pumped dye amplifiers and a final, longitudinally pumped, amplifier. Esherick and Owyoung[66] illustrated a similar pulsed amplifier as part of a high resolution inverse Raman system. Rahn[70] designed and constructed an elegant pulsed amplifier which virtually eliminated amplified spontaneous emission. In addition, there is at least one commercial pulsed dye amplifier (Lambda Physik FL 2003) on the market.

Our initial approach was to simplify the pulsed amplifier system to its bare minimum by eliminating elements which were not absolutely necessary, with the idea of perhaps adding those or other elements later if the need was demonstrated. This strategy proved wise as, at the present stage of development, there has been very little added to the system. The initial design was a composite of the designs of Drell and Chu[65] and Esherick and Owyoung[66] and is depicted in Figure 4.5. The pump source is a doubled, single-mode Nd:YAG laser (Molectron MY34-10) with a temporal pulse width of 20 ns. The 532 nm output is used to pump the three amplifier stages. All of the previous

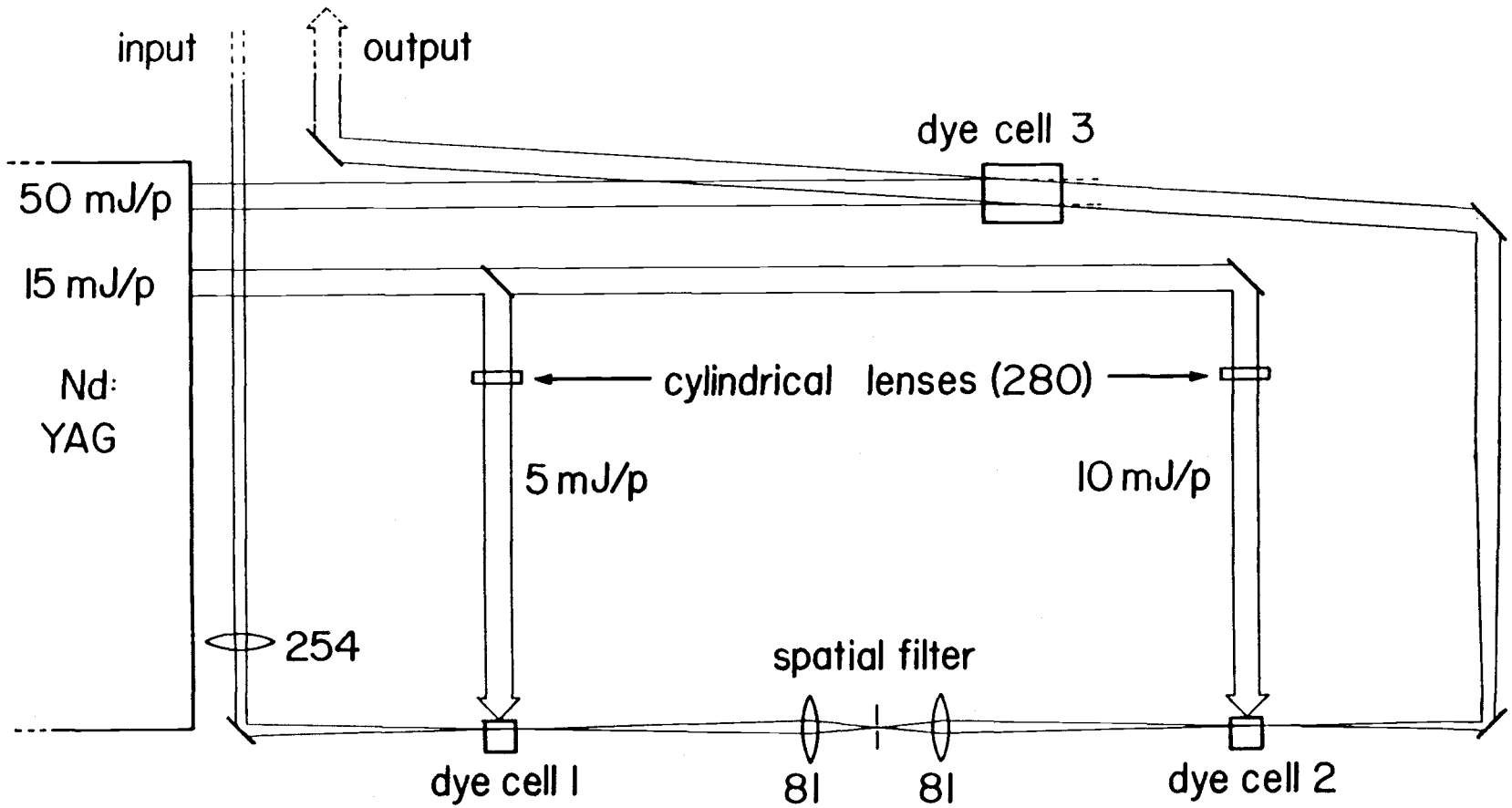

Figure 4.5 Schematic of the optical layout of the pulsed dye amplifier.

designs featured a Faraday rotator between the cw dye laser and the first amplifier stage to isolate the dye laser from the instabilities caused by feedback of amplified spontaneous emission produced in the amplifier chain. Since a Faraday rotator is expensive and we did not already have one, we were pleased that it proved sufficient to isolate the dye laser with a long path (1.5 m) and aperture between it and the first amplifier stage.

Amplified spontaneous emission (ASE) is a by-product of pumping a gain medium such as a laser dye. The population inversion which is required to sustain oscillation or amplification will relax to equilibrium by any means possible. Three modes of decay are possible, nonradiative or thermal decay, spontaneous emission and stimulated emission. The fluorescent dyes typically used for amplifying lasers have a low rate of nonradiative decay compared to the spontaneous and stimulated channels. The ASE results when the gain medium emits a spontaneous photon along the direction of pumping. This photon can then cause stimulated emission from other excited molecules along the same path, resulting in a laser like beam along the direction of propagation. Even without feedback, ASE can cause significant depletion of the population inversion and cause excessive background noise.[71] Ultimately the energy that can be stored in an amplifier and hence the maximum gain is limited mainly by ASE. A recent estimate of single pass gain to be expected from a transverse pumped dye amplifier cell is 3×10^4, a value reduced from previous predictions by a factor of >250.[72]

Another element not included in our original design was a dispersive element between the first and second stages of

amplification. This is typically a direct-vision prism, an optical element which passes the frequency of interest parallel to the incident light while dispersing other frequencies off the optical axis.[73] The purpose of this element is to discriminate against the ASE by dispersing the output of the first amplifier stage prior to focusing through a pinhole. It is important to minimize the copropagating ASE emerging from the first stage since it will experience two more stages of amplification and can seriously deplete the power delivered to the laser beam. The disadvantage to having a dispersive element in the amplifier chain is that a major shift of the dye laser frequency requires realignment of the amplifier elements.

The final design constraint was to use as few optical elements as possible. The lenses used in the amplifier were uncoated and hence each lens caused an 8% reflection loss. The prisms used for turning the beams, however, had broadband anti-reflection (BBAR) coatings to minimize additional losses.

Cells for the amplifier were obtained as a stock flow-through fluorometer cell (Hellma Type 131QS). The cells were 12.5 mm square with a length of 45 mm, constructed from quartz and polished on all four sides. They have a 4 mm tube affixed to each end to facilitate coupling to the dye pump and reservoir. Quartz was selected as the cell material because there is a greater range between the fusing temperature and the softening temperature compared to commercial optical glass. This results in less optical distortion near the fused joints of the cell and and allows the laser to propagate very close to the front surface of the cell. Specially constructed wedged dye laser cells with BBAR coating could have been obtained at four times the

price.

To minimize reflection losses and enhance the purity of polarization as well as discriminate against ASE with random polarization, the cells are oriented at Brewster's angle. This has the additional feature of minimizing the length of the pumped gain medium between the parallel sides of the dye cells. The dye used in the amplifier depends upon the required wavelength range. Table 4.2 gives a list of the choices of dye for the amplifier as a function of the wavelength range and the dye chosen for the ring dye laser. It is appropriate to note that the dye chosen for the ring dye laser and the complementary dye for the amplifier are different due to the "blue shift" of the dye when pumped with a Nd:YAG. The first two stages of the amplifier are separated by a spatial filter to minimize the passage of ASE. In addition, four iris apertures are placed to define the input laser beam, on either side of the spatial filter and between the second and the third stages of the amplifier. By far the most critical aperture is the adjustable iris between the spatial filter and the second amplifier stage.

The third amplifier stage is constructed from two 2 in. round windows secured in a delrin housing with an internal spacing of 17 mm. This cell is also oriented at Brewster's angle and is longitudinally pumped. The dye beam is slowly diverging from its focus in the second stage and the 532 nm pump is collimated as it emerges from the laser. In the overlap region in the dye the beams are approximately the same size. Due to the Brewster orientation of the cell, the path length is ~22 mm and the dye concentration is a factor of ten weaker than that in the first and second amplifier stages. For Rhodamine 575, the dye used

Table 4.2 Dyes for the YAG pumped pulsed amplifier useful with specific ranges of the ring dye laser.

Argon pumped (699-29)				YAG pumped (pulsed amp.)			
Dye	λ (Å)			Dye	λ (Å)		
R110	5450	--	5850	R575	5520	--	5820
				R590	5420	--	6070
R590	5715	--	6211	R590	5420	--	6070
				R610	5700	--	6290
				KR620	5700	--	6040
				R640	5900	--	6800
				DCM	6080	--	6820
DCM	6100	--	7000	DCM	6080	--	6920
				LD688	6530	--	7250

in the current experiments, the concentration in the first and second stages of the amplifier is 2.8×10^{-4} M (116 mg/L) while in the third stage the concentration is 2.8×10^{-5} M (11.6 mg/L). Virtually all of the pump laser energy is absorbed in the first 2 mm in the side pumped stages whereas only 80 - 90% of the pump energy is absorbed within the third stage.

Pump power delivered to the three amplifier stages are 3-5 mJ/p (milliJoules per pulse) to the first stage, 6-10 mJ/p to the second stage and 30-50 mJ/p to the final stage. The overall amplification of a 200 mW beam from the ring dye laser is ~10^6 yielding a pulse power of ~4 mJ. Very roughly the gain in the first stage is 10^3, in the second stage 10^2 and in the third stage ~10.

Throughout the setup phase of the pulsed dye amplifier a chopper was placed at the output of the ring dye laser to limit the pulse length to about 100 μs. This was done to minimize the power dissipated in the photodiode which was used to measure gain and temporal profile. At one point the chopper was removed from the dye laser path and the full power of the cw beam fell upon the first dye amplifier cell. This immediately caused severe thermal effects in the dye medium and caused the beam to steer completely out of the normal beam path. Esherick and Owyoung[66] include an electro-optic chopper in their design of a pulsed amplifier system and they do make an offhand reference to these same thermal effects.

DETECTOR

The choice of detector for an inverse Raman experiment bears some consideration. The objective, as with most experiments is to maximize

the signal to noise ratio. As was discussed in Chapter 2, the inverse Raman signal appears at the detector as a small absorption of the probe beam intensity. The design goal for the optical experiment is to maximize the signal, while the detector is optimized to see the signal with a minimum of background noise. This noise ultimately determines the smallest signal which can be detected and hence the sensitivity of the system. Noise at the detector can be separated into three sources, thermal noise, classical noise and shot noise.[74] Thermal noise results in dark current due to the mobility of charge carriers at temperatures above 0 K. In the high current case of inverse Raman spectroscopy, thermal noise is completely swamped by the high ambient currents. Classical noise is described by Tolles[74] as noise due to uncontrolled quantities such as turbulent eddies in the plasma discharge of laser sources and other uncharacterized noise. Shot noise is caused by the fluctuations in current that are due to the discreteness of the charge carriers and to random electronic emission.[31] Since shot noise poses the ultimate quantum limit on the noise background, it is worthwhile to investigate this limit in terms of actual experimental conditions.

The detector used in this experiment is a fast silicon photodiode (EG&G FND-100Q) which has an active area of 5.1 mm^2, a rise time of <1 ns and capacity for reasonably high current with a short duty cycle. Shot noise can be expressed as the mean-square current amplitude with respect to an average current,

$$\overline{i_N^2}(\nu) = 2e\bar{I}\Delta\nu \quad . \tag{4.1}$$

Here e is the charge on an electron and $\Delta\nu$ is the frequency

bandwidth.[75] The current through the photodiode due to illumination by the probe laser is 24 mA. Using a bandwidth derived from the 15 ns gate ($\Delta\nu$ = 66 MHz) and $\bar{I}$ = 24 mA in Eq. (4.1), the square of the shot noise is 5.1×10^{-13} A^2. This yields an rms value of 7.1×10^{-7} A or 3.6×10^{-5} V across the 50 Ω load. With a maximum amplification in this experiment of 2×10^4 (see below), the voltage fluctuations observed at the output of the boxcar due to shot noise alone would be 0.71 V rms. If 30 shots are signal averaged the apparent noise is reduced by a factor of $(30)^{\frac{1}{2}}$ so that the noise on the spectrum due to shot noise would have a rms value of 0.13 V. The best spectrum taken under these conditions shows peak noise of 0.25 V indicating that the spectrometer is working close to the shot noise limit.

SIGNAL DETECTION

Figure 4.6 is a schematic of the inverse Raman experiment. The single-mode argon ion probe laser and the tunable pulsed pump laser system have already been described in detail. Once the required beams are available, the optical arrangement of the experiment is quite simple. Note that both the probe laser and the cw dye laser oscillator are chopped by the same slit so that they each have a pulse width of ~100 μs. This chopping minimizes the previously discussed thermal effects in the dye amplifier cells and creates a quasi-cw probe beam to lower the duty cycle on the detector photodiode.

The pump and the probe beams each pass through the center of independent focussing lenses to prevent off-axis aberrations from distorting the beams at their foci and to permit spatial overlap to be adjusted in all three dimensions. For this latter purpose the pump

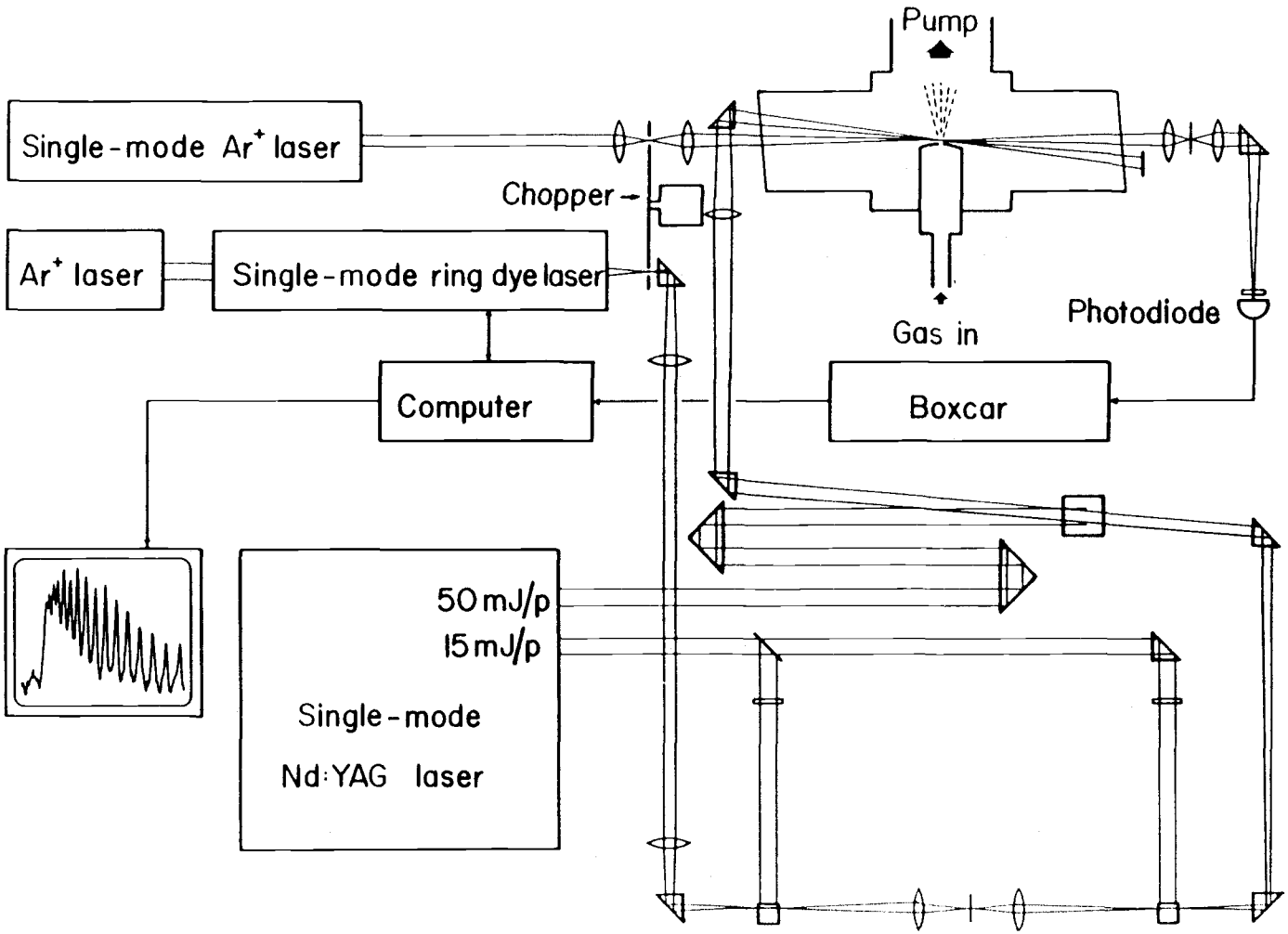

Figure 4.6 Optical schematic of the inverse Raman spectrometer.

beam focussing lens is mounted upon an adjustable stage permitting movement parallel to the optical axis. In this crossed beam experiment, the angular separation of the pump and probe beams is typically ~2°. This allows the pump beam to be blocked immediately after the sample cell and to be further discriminated against with a spatial filter. The probe beam is focussed onto the detector with a spherical reflector. The detector is shielded from stray light by a 230 × 25 mm tube located along the optical axis. For further discrimination, a narrow bandpass interference filter (5145 Å) is placed immediately in front of the fast photodiode biased with 90 V.

The signal from the photodiode passes through a 7 m length of coaxial cable and is coupled into the input of a pair of cascaded video amplifiers (Comlinear CLC100) by a 470 pF capacitor. Together the video amplifiers boost the signal by a factor of 100 before it is input into the boxcar integrator (Stanford Research Systems SR 250). The gate width (~15 ns) and delay are adjusted to optimize the detection of the signal. The 7 m length of coaxial cable delays the signal by ~35 ns in order to overcome the trigger delay of the SRS boxcar (~25 ns). The averaged output of the boxcar is digitized by the interface electronics supplied with the Coherent laser and stored on floppy disk using the data collection software supplied by Coherent for the Apple IIe microcomputer.

A timing diagram is shown in Figure 4.7. A 600 rpm chopper provides the master timing pulse synchronized to the chopped laser beams with an optical switch and a timing hole at the edge of the wheel. The conditioned output of the optical switch provides a trigger pulse to the "lamp trigger" input of the Nd:YAG, preceding the Q

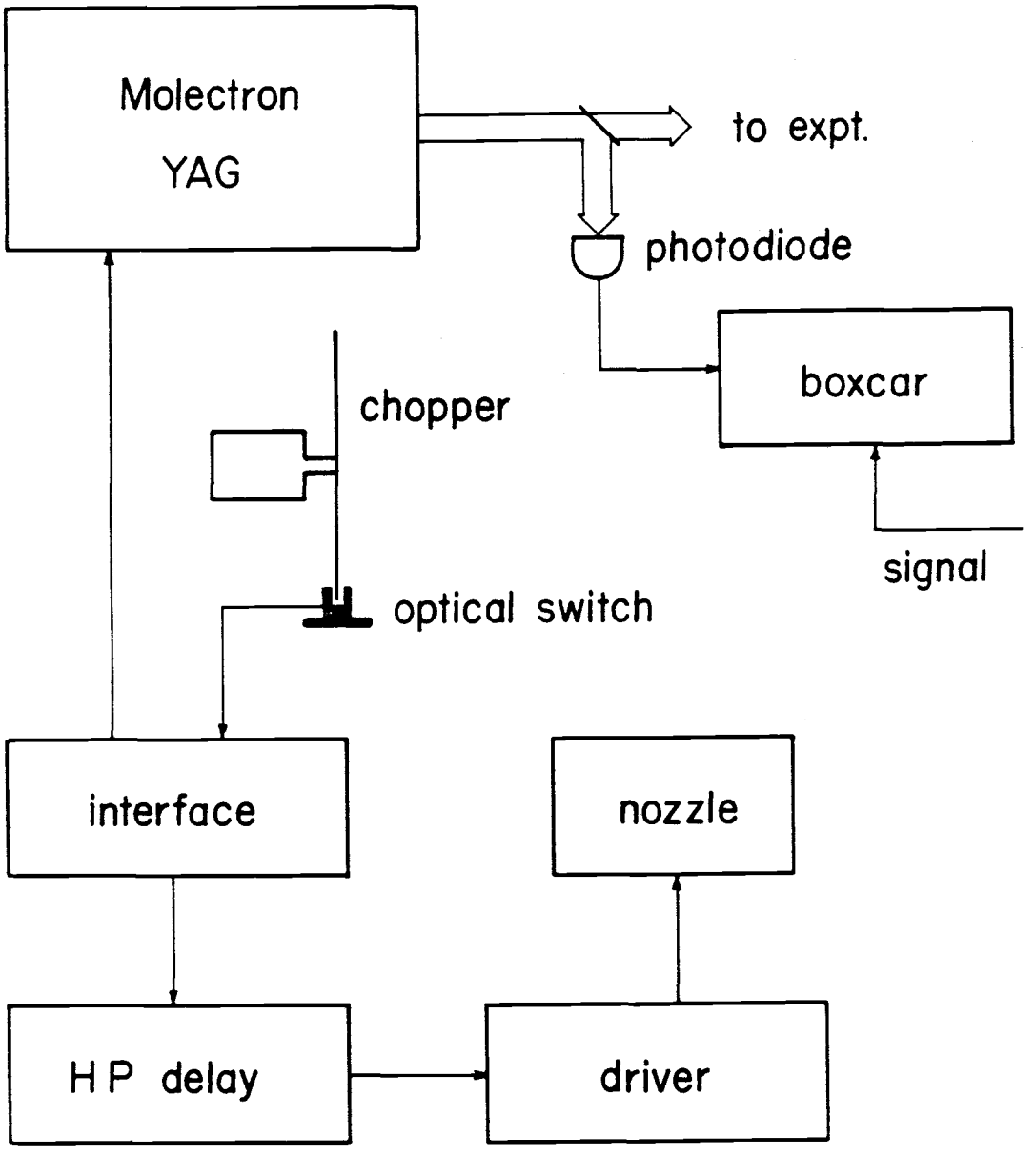

Figure 4.7 Timing diagram for inverse Raman experiment. The primary timing pulse is generated by the 600 rpm chopper which chops both the dye laser and the argon ion laser in addition to activating the optical switch.

switched output by ~750 μs. The trigger for the boxcar is obtained from a photodiode monitoring the 532 nm output of the YAG in much the same fashion as described in chapter 3. This arrangement is necessitated because the Q switched output of the YAG with the single-mode option is internally triggered and experiences a temporal jitter of ±5 μs relative to the input trigger. The timing pulse from the master oscillator is also used to trigger the pulsed supersonic jet system as described in Chapter 3.

RESULTS AND DISCUSSION

An initial study of the CO_2 Fermi doublet was undertaken as a means of characterizing the performance of the spectrometer. Of particular interest are the instrumental limits to sensitivity and resolution. The Q branches, ν_1 and $2\nu_2$, of CO_2 which were discussed in chapter 3 offer a useful test of these parameters. The spectroscopic work detailed in chapter 3 enables us to establish comparative sensitivities. In addition, the $2\nu_2$ peak is extraordinarily narrow and hence serves as a convenient resolution standard. This small linewidth is due to the almost perfect coincidence of the rotational substructure since the B values are nearly identical in the upper and lower vibrational states. The ν_1 peak, though unresolved in the CARS experiment, does have structure resolvable in this high resolution experiment and this also was used to estimate the instrumental resolution.

Resolution Estimates

Our laboratory equipment does not include an étalon with the

necessary free spectral range to directly measure the width of the dye laser peak. For this reason an indirect method of measuring instrumental resolution was undertaken. A series of ν_1 scans of the monomer at room temperature were taken at static pressures ranging from 5 Torr to 740 Torr. Figure 4.8 shows a representative series ranging from the almost fully resolved spectrum at 10 Torr to the completely unresolved "broad" band at 740 Torr. We note that the width of the unresolved peak is only 0.12 cm^{-1} (FWHM) so that the term broad here is clearly relative. The spectra were compared to spectra calculated using the program CARLINR.FOR. This program is the latest version of a CARS/Raman spectral calculation program which was first written by Dr. Peter Huber-Wälchli and Dr. Dennis Guthals. It was further extensively modified by Dr. Thomas Lundeen. The current version was completely rewritten by Dr. Jeng J. Yang and contains numerous extensions which allow the calculation of pure rotational spectra of linear polyatomics as well as the O, Q and S rovibrational spectra. For purposes of comparing spectra a 0.7 cm^{-1} segment of the ν_1 Q branch was calculated, showing transitions out to J = 54.

Because of the low S/N at low pressures, linewidth measurements of isolated lines were not very accurate e.g. 0.007 $\pm$0.001 cm^{-1} for Q_{18}. It is possible to make a better estimate of the linewidth of the lower pressure spectra by comparing the overall contours to those of computed spectra. Calculations were performed assuming individual linewidths from 0.004 through 0.040 cm^{-1}. Each experimental curve was visually compared to the set of calculated spectra and a "best fit" linewidth was determined. In this manner an average linewidth, assumed the same for each J line, was found for each of the spectra with

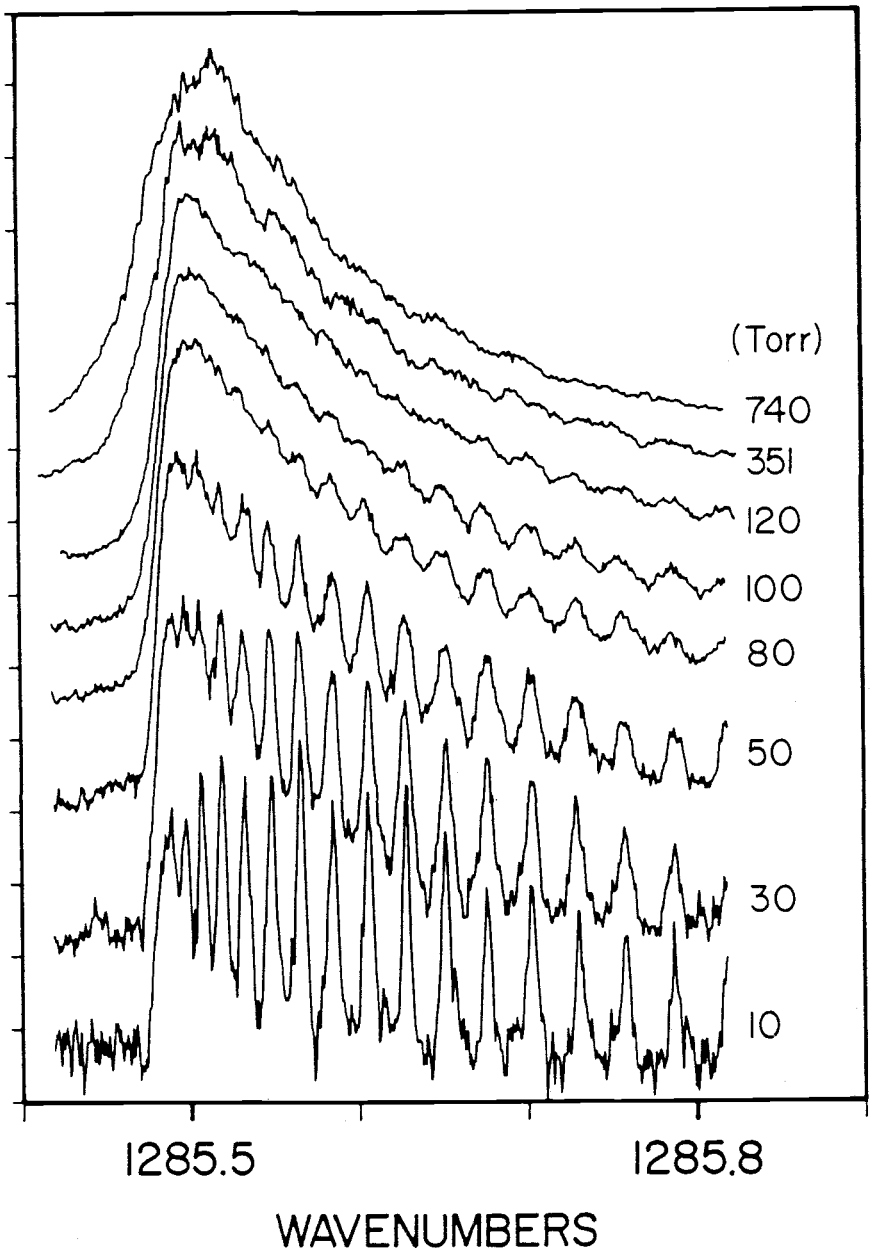

Figure 4.8 High resolution inverse Raman scans of the ν_1 mode of neat CO_2 monomer at a series of pressures.

resolvable structure. Figure 4.9 is a plot of the estimated linewidths of the spectra from 10 Torr to 150 Torr. This curve is reasonably linear and has a slope of 0.000237 $\pm$0.000005 cm^{-1}/Torr and a zero pressure intercept of ~0.0041 $\pm$0.0003 cm^{-1}. The latter is due to the natural width and the Doppler width plus the instrumental broadening. Since the transition from the excited to the ground state is not one photon allowed, both states have very long lifetimes and hence well defined energies. Thus we presume that the natural Raman linewidth will be very narrow and can be neglected in this discussion.

The Maxwell-Boltzmann velocity distribution (Doppler broadening) is responsible for the Gaussian lineshape of the peak. Our measurements of the dye laser temporal profile suggests that a Gaussian is also a reasonable dye laser lineshape. Thus the 0.0041 cm^{-1} zero pressure linewidth is the convolution of two Gaussian peaks. Note that we are assuming that the probe laser has a negligible linewidth relative to the dye laser peak. The 0.0041 cm^{-1} intercept can then be deconvoluted into its component 0.0024 cm^{-1} Doppler linewidth and a 0.0033 cm^{-1} instrumental linewidth.

A second estimate of the resolving capability of our system was extracted from the inverse Raman spectra of the $2\nu_2$ monomer Q branch (Figure 4.10). The individual rotational lines were not resolved due to the extremely close spacing between them (<0.002 cm^{-1} through Q_{34}) and a bandhead turnaround at Q_{28}. Trace (a) is a scan taken at 1 Torr static pressure with a width of 0.013 cm^{-1} (FWHM) and trace (b) is of 5% CO_2 in He in a jet with a width of 0.0047 cm^{-1} (FWHM). This latter spectrum has the narrowest linewidth recorded with this equipment to date. The width of this peak depends upon both the

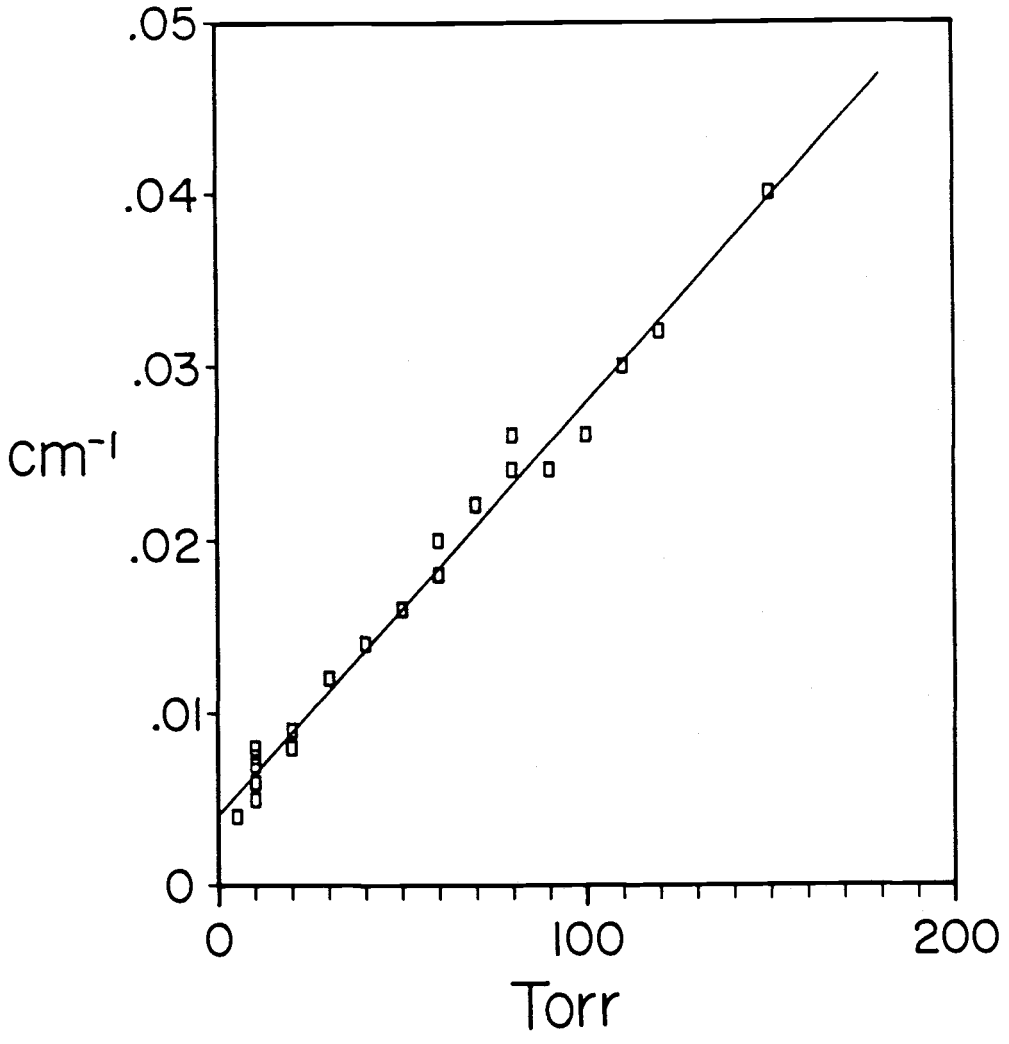

Figure 4.9 Plot of linewidths derived from all low pressure spectra of the ν_1 monomer Q branch of CO_2 plotted against static pressure. These linewidths were measured by visual comparison of the spectra with a series of calculated spectra.

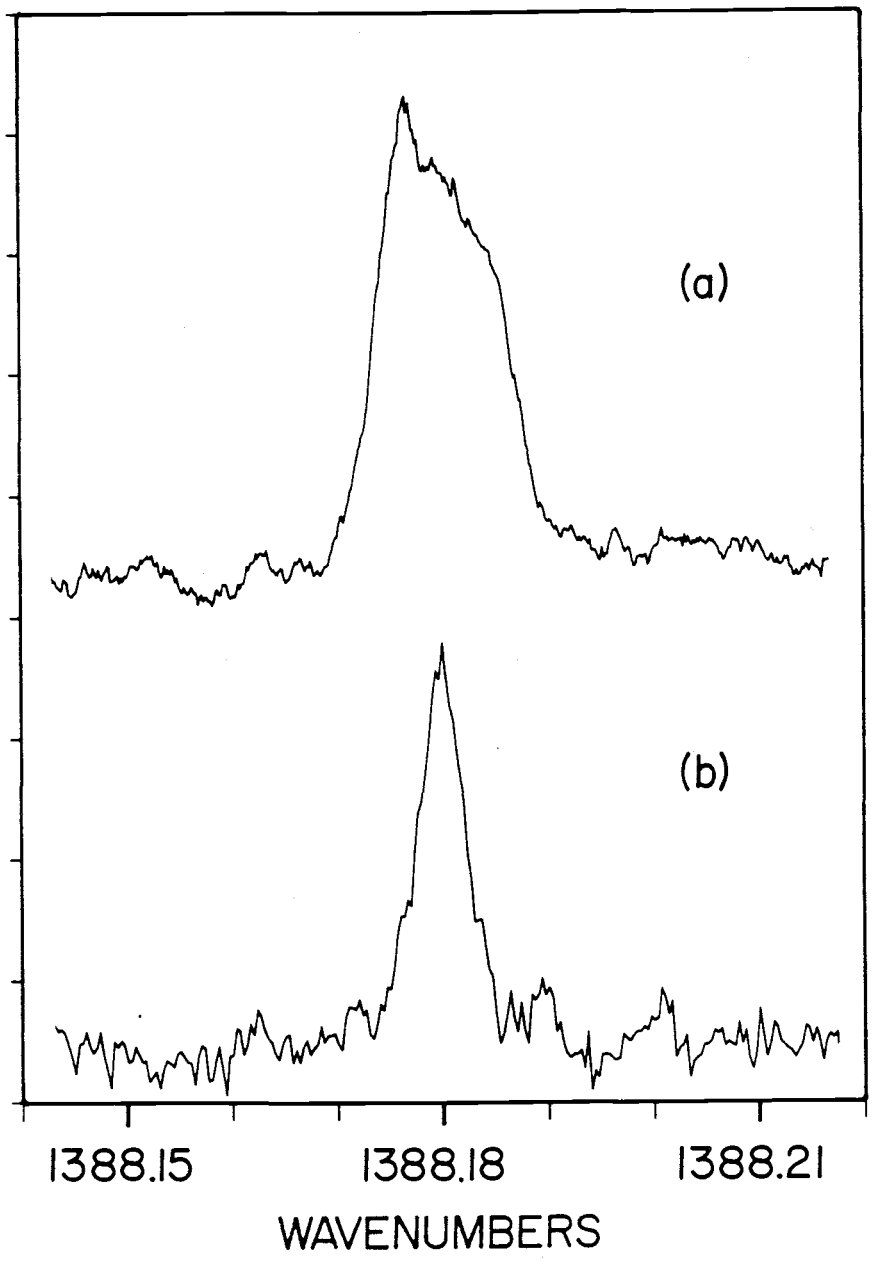

Figure 4.10 Two scans of the $2\nu_2$ Q branch of CO_2. (a) static scan T = 300 K, P = 1 Torr, Width = 0.013 cm^{-1} (FWHM). (b) jet scan $\%CO_2$ in He = 5, T_0 = 203 K, P_0 = 14.6 atm, Width = 0.0047 cm^{-1}.

translational temperature (Doppler broadening) and the rotational temperature (rotational state populations). Previous studies indicate that the rotational temperature is usually only slightly higher than the translational temperature in a free jet expansion,[76] so we will assume that they are the same for the purposes of calculating a spectrum. The exact position of sampling is not known but a range for X/D, and hence for T_{Trans}, can be estimated. A value for the highest temperature in the jet comes from an evaluation of the temperature associated with a supersonic expansion of pure helium at an X/D of 1.7 (60 K). This is a reasonable estimate of the closest approach X/D value and the 60K translational temperature yields a Doppler width of 0.0011 cm^{-1}. A low temperature limit comes from assuming X/D = 4, an absolute maximum value for the recorded experimental conditions. The predicted temperature at this position is 13.5 K, corresponding to a Doppler width of 0.00055 cm^{-1}. Spectra of $2\nu_2$ were calculated for these conditions and convoluted with various assumed instrumental linewidths. Good agreement was achieved with an assumed instrumental linewidth of 0.0015 cm^{-1} (60 K) and 0.0042 cm^{-1} (13.5 K). These values provide reasonable boundaries to an average instrumental linewidth of 0.0029 $\pm$0.0014 cm^{-1}.

The Fourier transform of the measured temporal profile of the dye laser pulse provides a third and final estimate of the resolution of the system. This is the fundamental limit imposed by the uncertainty principle which for Gaussian peaks takes the form $\Delta\nu\Delta t \geq 2\ln 2/\pi$ (0.44).[77] This yields a width (FWHM) of 0.0019 $\pm$0.0003 cm^{-1} for a measured pulse width of 7.6 $\pm$1 ns (FWHM). Comparison with the linewidths derived from the ν_1 and $2\nu_2$ bands thus clearly indicate

that the spectrometer is operating near the transform limit.

The resolution and sensitivity of this IRS system has extended the low pressure limit for studies of CO_2 linewidths and it is interesting to compare our results with studies by others at higher pressure. By extrapolation of the data in Figure 4.9, we deduce an isolated linewidth of 0.180 cm^{-1} for each Q-line of ν_1 at 740 Torr. Using this value a calculated spectrum for the entire Q branch at 740 Torr shows no structure and an overall width of 0.32 cm^{-1}. This is more than twice the value of 0.12 cm^{-1} which we actually measure at 740 torr (Fig. 4.8). Such a discrepancy was also noted previously by Baran et al.[78] in their cw Raman gain measurements where the observed overall width (0.13 cm^{-1} at 760 Torr) was much smaller than that they calculated (0.23 cm^{-1}). The latter was an approximate value derived by fitting the low shift side of the unresolved Q branch to a Lorentzian. Our more direct measurements confirm their explanation that motional narrowing is responsible for the reduced ν_1 linewidth of CO_2 at 760 Torr. Such narrowing is known for other systems and occurs when the inelastic collision frequency exceeds the frequency separation between adjacent transitions in the dense ν_1 Q branch spectrum.

Sensitivity Estimates

To judge the relative sensitivities of the IRS system, additional scans were taken of neat CO_2 and CO_2/He mixtures in supersonic expansions. These spectra are represented in Figure 4.11. The neat CO_2 spectrum matches a spectrum calculated for a temperature of 60 K. Absolute sensitivity measurements are difficult to quantify,

however comparison of the monomer line in Figure 4.11b with that in 3.9a shows that, under similar scanning conditions, the S/N of the IRS spectra is about 10 to 20 times lower than that obtained by CARS. Due to the large difference in the power per unit bandwidth between the CARS and IRS systems, this factor will change depending upon the width of the observed line. A narrow transition, such as the $2\nu_2$ monomer Q branch, benefits from the use of the very narrow lasers in the IRS system while in the CARS system, with a dye laser width 20 times the width of the 1 Torr static peak, only a fraction of the dye laser power is resonant and produces signal. A broad peak, on the other hand, is probed equally effectively using either a broad or narrow laser.

Search for CO_2 Dimer

The spectra of the ν_1 and $2\nu_2$ bands of CO_2 serve to illustrate the high resolution capabilities of this inverse Raman system. Furthermore, the observation of both the ν_1 and $2\nu_2$ bands in the jet indicate that the technique has sufficient sensitivity to probe the dilute conditions in a supersonic expansion. Having established this capability, there was considerable interest in applying this high resolution inverse Raman system to probe the CO_2 dimer peak for possible evidence of rotational fine structure. Figure 4.12 is a thirteen cm^{-1} scan covering the ν_1 region from the monomer through the polymer. This was a cooled, pulsed jet experiment with 5% CO_2 in He at 14.6 atm stagnation pressure. The monomer was scanned both before the scan and afterwards with a neat CO_2 sample in the jet to guarantee instrumental integrity. The output of the boxcar was digitized at 50 MHz intervals resulting in 7800 data points for one

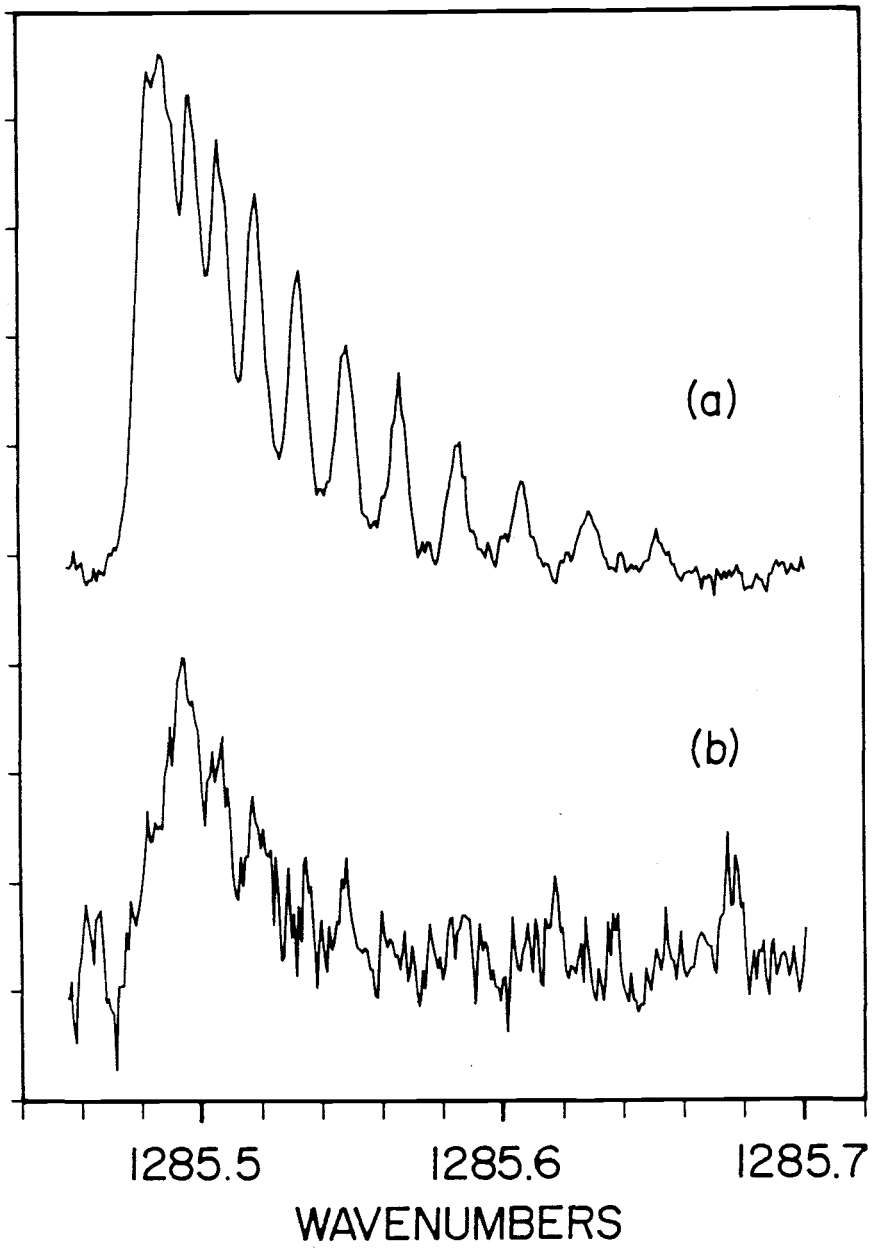

Figure 4.11 Jet spectra of (a) neat CO_2 T_0 = 300 K, P_0 = 7.8 atm, and (b) 5% CO_2 in He, T_0 = 261 K, P_0 = 14.6 atm.

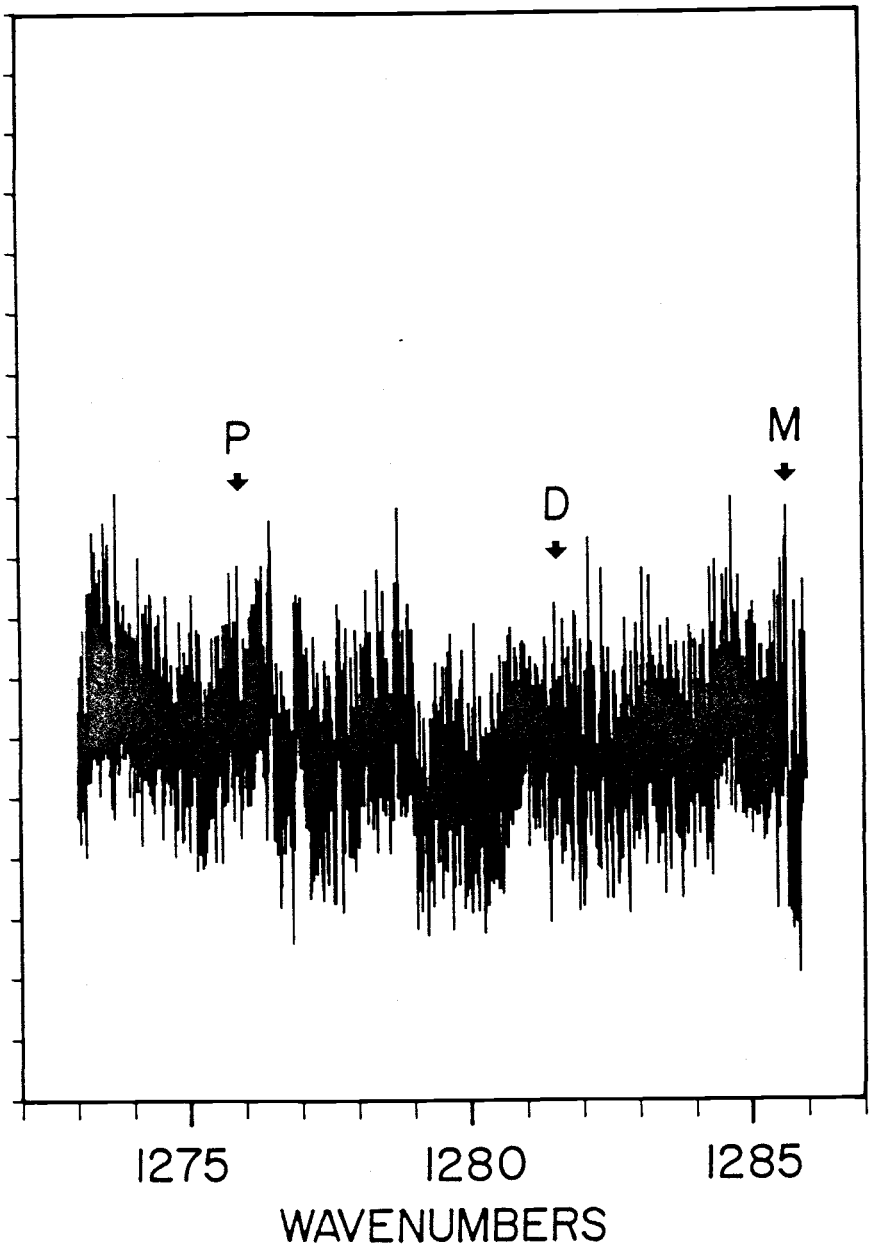

Figure 4.12 Thirteen cm^{-1} scan through the ν_1 dimer and polymer region of CO_2. T_0 = 261 K, P_0 = 14.6 atm, 5% CO_2 in He.

scan. In an expansion of the monomer region, the monomer is just discernible above the noise. Comparison of this spectrum with a CARS spectrum at similar conditions (cf. Fig. 3.9a) indicates that the cluster peaks should be of comparable intensity to the monomer. It is clear that this spectrum is at the ragged edge of the sensitivity of these preliminary experiments. There is no structure that can be attributed to clusters. Thus, while the present system has enough sensitivity to detect monomeric species of interest in dilute jet expansion, an enhancement in signal of an order of magnitude will be required to achieve results comparable to the CARS system.

Experimental Enhancements

Several aspects of the experiment could be modified to enhance the signal or reduce the noise. For jet experiments, there is an indication that using nozzles with a slit rather than a round hole creates a free jet with a higher number density along a line which can be oriented with the focal cylinder in the crossed beam experiment. This could enhance the signal level by a significant factor. The noise in the system is due to several effects. There is evidence of radio frequency pickup by the coaxial cable used to create a time delay. The system is presently being modified to utilize a triaxial cable where the signal return shield is itself surrounded by a grounded Faraday shield.

Another source of noise is associated with the temporal jitter between the trigger to the Molectron YAG laser and the resulting light pulse. There are two aspects to this jitter, one is the shot to shot variation which is ± 5 ns. The other is a longer term variation

associated with the temperature fluctuations in the Molectron which cause a gradual shift of stable single modes. Adjustments to the YAG étalon or Q switch voltage, which are sometimes made during a scan to maintain stable operation, can cause a similar timing variation. The trigger to the boxcar however, is taken from the Molectron light pulse with the result that there is negligible jitter of the boxcar gate with respect to the signal pulse even with a substantial change in the delay from initial YAG trigger to light pulse. This jitter does, however, change the time of the laser firing relative to the 100 μs probe pulse.

As previously discussed, the detector is coupled to the video amplifiers through a 470 pF capacitor to remove the dc component prior to amplification. The resulting signal consists of a pair of mirror image derivative curves which coincide with the leading and trailing edges of the probe laser pulse along with the high frequency signal pulse. The leading pulse is on the order of several volts and appears to cause a momentary imbalance in the video amplifiers. An oscilloscope trace of the amplified probe pulse shows a very slight dc offset which changes during the 100 μs pulse width. This dc ramp has a peak to peak voltage of ~5 mV which causes no problems except under high gain conditions. With the boxcar set to its maximum sensitivity (Gain = 200) a change of 10 μs in the position of the dye laser pulse relative to the probe laser pulse causes a change in the dc offset of 0.5 mV resulting in a 0.1 V change in the output of the boxcar. This is the expected voltage fluctuation due to the shot-to-shot timing fluctuations. The timing changes associated with the adjustment of the Q switch voltage or the étalon or with mode hops in the YAG can be as much as 30 μs. The resulting change in the baseline at the output of

the boxcar would be 0.3 V. These baseline fluctuations limit the sensitivity of the instrument in its current configuration. Modifications to the detector electronics are currently underway in an effort to improve this situation.

Further improvements in the signal to noise ratio would be anticipated with a major modification to the data collection system. The present system software sends the averaged output of the boxcar to the Apple computer and does not permit single shot capture of the data. This data collection program is currently being modified to digitize every shot and to allow ratioing of the signal by the output of the pulsed dye laser so as to reduce the "on resonance" noise. This should reduce the noise associated with the shot to shot fluctuations of the dye laser which arise in part from the fluctuations in the YAG source and from spatial variations in the dye cells due to laser wander and bubbles.

In this chapter we have documented the design and construction of a high resolution inverse Raman spectrometer which will find future application in the study of many molecular species. Here, an initial study of the CO_2 monomer bands was undertaken to characterize the spectrometer with respect to resolution and sensitivity. In addition, the apparatus was used in a preliminary examination of the dimer region of CO_2 which comprised the focus of the CARS work in chapter 3. Although the dimer band was not detected by IRS, it is believed that further enhancements in signal can be made so that this intriguing system may yield to future studies.

REFERENCES

1. C. V. Raman and K. S. Krishnan, Nature **121**, 501 (1928).

2. D. A. Long, Raman Spectroscopy, (McGraw-Hill, London, 1977).

3. E. J. Woodbury and W. K. Ng, Proc. IRE **50**, 2367 (1962).

4. R. W. Terhune, Bull. Am. Phys. Soc. **8**, 359 (1963).

5. R. W. Terhune and P. D. Maker, in Nonlinear Optics, Vol. 2, A. K. Levine, ed. (Dekker, New York, 1968) p. 294.

6. A. D. Wilson-Gordon and H. Friedmann, Chem. Phys. Lett. **89**, 273 (1982).

7. L. A. Rahn, R. L. Farrow, M. L. Koszykowski and P. L. Mattern, Phys. Rev. Lett. **45**, 620 (1980).

8. D. H. Levy, in Quantum Dynamics of Molecules: the New Experimental Challenge to Theorists, R. G. Wolley ed. (Plenum, New York, 1980) p. 115.

9. H. Ashkenhas and F. S. Sherman in Rarefied Gas Dynamics, J. H. de Leeuw, ed. Vol. II (Academic Press, New York, 1966) p. 84.

10. E. K. Gustafson, Ph.D. thesis, Stanford University, (1983).

11. F. Koenig, P. Oesterlin and R. L. Byer, Chem. Phys. Lett. **88**, 477 (1982).

12. G. A. Hopkins, M. Maroncelli and J. W. Nibler, Chem. Phys. Lett. **114**, 97 (1985).

13. M. Maroncelli, G. A. Hopkins, J. W. Nibler and T. R. Dyke, J. Chem. Phys. **83**, 2129 (1985).

14. E. W. Becker, K. Bier and W. Henkes, Z. Physik **146**, 333 (1956).

15. W. G. Dorfeld and J. B. Hudson, J. Chem. Phys. **59**, 1253 (1973).

16. W. G. Dorfeld and J. B. Hudson, J. Chem. Phys. **59**, 1261 (1973).

17. O. F. Hagena and W. Obert, J. Chem. Phys. **56**, 1793 (1972).

18. O. F. Hagena, Surf. Sci. **106**, 101 (1981).

19. E. Garmire, F. Pandarese and C. H. Townes, Phys. Rev. Lett. **11**, 160 (1963).

20. N. Bloembergen, Nonlinear Optics, (Benjamin, New York, 1965).

21. N. Bloembergen, Am J. Phys. 35, 989 (1967).

22. P. D. Maker and R. W. Terhune, Phys. Rev. A: **137**, 801 (1965).

23. Y. R. Shen and N. Bloembergen, Phys. Rev. A: **137**, 1787 (1965).

24. J. A. Giordmaine and W. Kaiser, Phys. Rev. **144**, 676 (1966).

25. M. Maier, W. Kaiser and J. A. Giordmaine, Phys. Rev. **177**, 580 (1969).

26. R. H. Pantell and H. E. Puthoff, Fundamentals of Quantum Electronics, (Wiley, New York, 1969).

27. P. Lallemand, in The Raman Effect, Vol. 1, A. Anderson, ed. (Dekker, New York, 1971) p. 287.

28. W. Kaiser and M. Maier, in Laser Handbook, Vol. 2, F. T. Arecchi and E. O. Schulz-Dubois, eds. (North-Holland, Amsterdam, 1972) p. 1077.

29. Y. R. Shen, in "Light Scattering in Solids," Topics in Applied Physics, Vol. 8, M. Cardona, ed. (Springer-Verlag, Berlin and New York, 1975) p. 275.

30. C. S. Wang, in Quantum Electronics: A Treatise, Vol. 1, H. Rabin and C. L. Tang, eds. (Academic Press, New York, 1975) p. 447.

31. A. Yariv, Quantum Electronics, (Wiley, New York, 1975).

32. M. Maier, Appl. Phys. **11**, 209 (1976).

33. J. Ducuing, in Nonlinear Optics, P. G. Harper and B. S. Wherrett, eds. (Academic Press, New York, 1977) p. 11.

34. J. W. Nibler and G. V. Knighten, in "Raman Spectroscopy of Gases and Liquids," Topics in Current Physics, Vol. 11, A. Weber, ed. (Springer-Verlag, Berlin and New York, 1979) p. 253.

35. M. D. Levenson, Introduction to Nonhlinear Laser Spectroscopy, (Academic Press, New York, 1982).

36. J. P. Taran and S. Druet, Progress in Quantum Electronics, Vol. 7, (Pergamon, London, 1981) p. 1.

37. Y. Prior and A. N. Weiszmann, Phys. Rev. A: **29**, 2700 (1984).

38. Y. R. Shen, The Principles of Nonlinear Optics, (Wiley, New York, 1984).

39. D. J. Griffiths, Introduction to Electrodynamics, (Prentice-Hall, Englewood Cliffs, NJ, 1981) p. 170.

40. W. J. Jones, in Non-Linear Raman Spectroscopy and Its Chemical Applications, W. Kiefer and D. A. Long, eds. Series C, Vol. 93 (Reidel, London, 1982) p. 473.

41. W. Kiefer, in Non-Linear Raman Spectroscopy and Its Chemical Applications, W. Kiefer and D. A. Long, eds. Series C, Vol. 93 (Reidel, London, 1982) p. 241.

42. J. O. Hirschfelder, C. F. Curtiss and R. B. Bird, Molecular Theory of Gases and Liquids, (Wiley, New York, 1954).

43. G. C. Maitland, M. Rigby, E. B. Smith and W. A. Wakeham, Intermolecular Forces Their Origin and Determination, (Clarendon, Oxford, 1981).

44. T. Kihara, Intermolecular Forces (Wiley, New York, 1978).

45. J. S. Juenter, R. L. DeLeon and A. Yokozeki, Faraday Discuss. Chem. Soc. **73**, 63 (1982).

46. L. Mannik, J. C. Stryland and H. L. Welsh, Can. J. Phys. **49**, 3056 (1971).

47. S. E. Novick, P. B. Davies, T. R. Dyke and W. Klemperer, J. Am. Chem. Soc. **95**, 8547 (1973).

48. L. Fredin, B. Nelander and G. Ribbegard, J. Mol. Spectrosc. **53**, 410 (1974).

49. M. Hashimoto and T. Isobe, Bull. Chem. Soc. Japan **47**, 40 (1974).

50. A. Koide and T. Kihara, Chem. Phys. **5**, 34 (1974).

51. N. Brigot, S. Odiot, S. H. Walmsley and J. L. Whitten, Chem. Phys. Lett. **49**, 157 (1977).

52. R. Guasti, V. Schettino and N. Brigot, Chem. Phys. **34**, 391 (1978).

53. A. E. Barton, A. Chablo and B. J. Howard, Chem. Phys. Lett. **60**, 414 (1979).

54. R. L. Kopec, Ph.D. Thesis, Indiana University, Bloomington (1981).

55. T. E. Gough, R. E. Miller and G. Scoles, J. Phys. Chem. **85**, 4041 (1981).

56. R. E. Miller and R. O. Watts, Chem. Phys. Lett. **105**, 409 (1984).

57. J. M. Lobue, J. K. Rice and S. E. Novick, Chem. Phys. Lett. **112**, 376 (1984).

58. H. W. Schrötter and H. W. Klöckner, Raman Spectroscopy of Gases and Liquids, edited by A. Weber (Springer-Verlag, New York, 1979), p. 123.

59. A. Anderson and T. S. Sun, Chem. Phys. Lett. **8**, 537 (1971).

60. C. A. Haynam, D. V. Brumbaugh and D. H. Levy, J. Chem. Phys. **81**, 2282 (1984) and references therein;
Y. D. Park and D. H. Levy, J. Chem. Phys. **81**, 5527 (1984).

61. L. A. Rahn, A. Owyoung, M. E. Coltrin and M. L. Koszykowski, Proc. VIIth Int. Conf. on Raman Spectrosc. W. F. Murphy, ed. (North-Holland, Amsterdam, 1980) p. 694.

62. Spectra Physics model 165 ion laser instruction manual. (Spectra-Physics, Mountain View, CA, 1980) p. 5-3.

63. H. Frunder, L. Matziol, H. Finsterhölzl, A. Beckmann and H. W. Schrötter, J. Raman Spectrosc. **17**, 143 (1986).

64. M. G. Littman, Appl. Opt. **23**, 4465 (1984).

65. P. Drell and S. Chu, Opt. Commun. **28**, 343 (1979).

66. P. Esherick and A. Owyoung, Advances in Infrared and Raman Spectroscopy, R. J. H. Clark and R. E. Hestor eds. Vol. 9 (Heyden & Sons Ltd., London, 1982) pp. 130-187.

67. A. L. Bloom, J. Opt. Soc. Am. **64**, 447 (1974).

68. Coherent model 699 operating manual (Coherent, Palo Alto, CA, 1981).

69. Molectron model MY34-10 operating manual (Cooper Lasersonics, Santa Clara, CA, 1984).

70. L. A. Rahn, Sandia Laboratories, Livermore, personal communications.

71. U. Ganiel, A. Hardy, G. Neumann and D. Treves, IEEE J. Quantum Electron. **QE-11**, 881 (1975).

72. A. A. Hnilo, O. E. Martinez and E. J. Quel, IEEE J. Quantum Electron. **QE-22**, 20 (1986).

73. F. A. Jenkins and H. E. White, Fundamentals of Optics, 4th ed. (McGraw-Hill, New York, 1976), p. 34.

74. W. M. Tolles and A. B. Harvey, in Chemical Applications of Nonlinear Raman Spectroscopy, A. B. Harvey, ed. (Academic Press, New York, 1981), p. 17.

75. A. Yariv, Optical Electronics, 3rd. ed. (Holt, Rinehart and Winston, New York, 1985).

76. P. Huber-Wälchli and J. W. Nibler, J. Chem. Phys. **76**, 273 (1982).

77. D. J. Bradley, in Ultrashort Light Pulses, S. L. Shapiro, ed. Topics in Applied Physics, Vol. 18, (Springer-Verlag, Berlin, Heidelberg, New York, 1977) p. 17.

78. J. Baran, A. Grofcsik and W. J. Jones, Mol. Phys. **45**, 1291 (1982).